Numerical Modeling of the Work Piece Region in the Plasma Arc Cutting Process

A Thesis
SUBMITTED TO THE FACULTY OF
UNIVERSITY OF MINNESOTA
BY

David Osterhouse

IN PARTIAL FULFILLMENT OF THE REQUIREMENTS
FOR THE DEGREE OF
DOCTOR OF PHILOSOPHY

Terry Simon, Adviser

May, 2014

Acknowledgements

I am deeply thankful to my advisor, professor Joachim Heberlein, for his guidance throughout this work. His curiosity, intellect, experience and intuition has enriched not only this work but also, I believe, the entire plasma community. I am grateful, as well, to professor Terry Simon for filling the official role of advisor as Dr. Heberlein's health failed. I would also like to thank my office mate, Venkat Raman Narayan Thenkari for numerous conversations about plasma and particularly for his help in calculating partition functions. A great deal of insight was gained from conversations with John Lindsay, Yu Zhang, Madhura Mahajan and other employees of Hypertherm Inc.

The work was supported by funding received from Hypertherm Inc. A portion of this work was carried out on computing resources received from the Minnesota Supercomputing Institute.

Abstract

The plasma arc cutting process is widely used for the cutting of metals. The process, however, is not fully understood and further understanding will lead to further improvements. This work aims to elucidate the fundamental physical phenomena in the region where the plasma interacts with the work piece through the use of numerical modeling techniques. This model follows standard computational fluid dynamic methods that have been suitably modified to include plasma effects, assuming either local thermodynamic equilibrium or a slight non-equilibrium captured by the two-temperature assumption. This is implemented in the general purpose, open source CFD package, OpenFOAM. The model is applied to a plasma flow through a geometry that extends from inside the plasma torch to the bottom of the slot cut in the work piece. The shape of the kerf is taken from experimental measurements. The results of this model include the temperature, velocity, and electrical current distribution throughout the plasma. From this, the heat flux to and drag force on the work piece are calculated. The location of the arc attachment in the cut slot is also noted because it is a matter of interest in the published literature as well as significantly effecting the dynamics of the heat flux and drag force. The results of this model show that the LTE formulation is not sufficient to capture the physics present due to unphysical fluid dynamic instabilities and numerical problems with the arc attachment. The two-temperature formulation, however, captures a large part of the physics present. Of particular note, it is found that an additional inelastic collision factor is necessary to describe the increased energy transfer between electrons and diatomic molecules, which is widely neglected in published literature. It is also found that inclusion of the oxygen molecular ion is necessary to accurately describe the plasma flow, which has been neglected in all published two-temperature oxygen calculations. The heat flux is found to be greatest at the top of the cut slot where the thermal boundary layer is thinnest and the arc attachment increases heat transfer.

Table of Contents

List of Tables

List of Figures

Chapter 1

Introduction

1.1. Thermal Plasma

There are, broadly speaking, four states of matter. A material at a temperature of absolute zero will be a solid. As heat is added to this material, its temperature will rise until it reaches the melting point, at which the material will melt into a liquid. As further energy is added to this liquid, its temperature will rise further until it reaches the boiling temperature, at which point, the liquid boils into a gas. As further energy is added to the gas and the temperature increases further, electrons will be driven off of the atoms and molecules in ionization reactions. This gas which includes both ions and free electrons is the fourth state of matter, a plasma.

There are a great many similarities between a plasma and a simple gas. They both consist of numerous small particles (atoms, molecules, etc) that are not bound together but that fly around willy-nilly colliding with each other. As such, they both expand freely to fill any space available, which is the definition of a gas. Because of this, a plasma is sometimes referred to as a gas. The electrical properties of a plasma, however, are distinctively different than those of a simple gas. A simple gas is an extremely good electrical insulator. Because of the abundance of ions and free electrons in a plasma, however, it is an excellent electrical conductor. Thus, it is clear that wherever an electrical current seems to flow through a gas, it is, in fact, a plasma.

In such a plasma, it is noteworthy that the free electrons are orders of magnitude less massive than even the smallest atom. As such, the electrons behave somewhat differently than the atoms, molecules, and ions, which are collectively called the heavy species. In particular, electrons have a high mobility, which is to say that they are easily accelerated to high energies by electric fields. Furthermore, while the energy of the electrons and heavy species will tend to equilibrate through collisions, this is not always so. In such cases, the plasma is referred to as a

non-thermal plasma and the electron energy distribution function must be studied separately from the energy of the heavy species. In the present work, however, a thermal plasma is studied, in which there are sufficient collisions to equilibrate the electrons and heavy species. This assumption will be slightly relaxed to a two temperature assumption later, but this is a small enough deviation that it is still widely referred to as a thermal plasma.

1.2. Plasma Arc Cutting Process

The ability to cut metal into intricate shapes is important for many industries, such as car manufacturing, ship building, and building construction. There are four major methods for cutting metal: 1) oxy-fuel cutting, 2) laser cutting, 3) water jet cutting, and 4) plasma arc cutting. Oxy-fuel cutting simply uses a burning jet of combustible gas and oxygen to melt and remove metal. Laser cutting uses a high energy laser to melt the metal in combination with a jet of gas that removes the molten metal. Water jet cutting uses an extremely high velocity jet of water with abrasive particles included to wear away at the metal, creating a cut. Finally, plasma arc cutting uses an electrical arc carried by a jet of high enthalpy plasma to melt and blow away the metal.

Of these methods, oxy-fuel is the cheapest to operate and can be used on extremely thick sheets of metal, although it suffers from poor cut quality and slow cut speeds. Laser produces extremely clean and precise cuts although it is very expensive, only viable for thin metal and also suffers from slow cut speeds. Water jet cutting is also extremely clean and precise, and creates no heat affected zone adjacent to the cut. It is extremely slow, however, compared to other methods, which makes it expensive. Plasma cutting, on the other hand, has by far the fastest cut speeds with cut quality that is close to that of laser cutting. It also can cut very thick work pieces, up to four inches of mild steel. The cost is more than that for oxy-fuel but cheaper than that for laser or water jet cutting. Thus, plasma cutting has a clear advantage where high output and clean cuts are a priority.

The plasma cutting equipment consists of a power supply, a high frequency starter, and the cutting torch. The power supply maintains whatever voltage is necessary in order to supply a constant electrical current to the torch. The high frequency starter is used to produce a short pulse of extremely high voltage in order to break down the gas and initiate an arc at the beginning of a cut. The torch, shown in figure 1.1 consists of an electrode (the cathode) inside a nozzle, through which the working gas flows. This nozzle is often then placed in an additional nozzle, called the shield cap, through which shielding gas flows. The cathode, nozzle, and shield cap are made of

copper with a hafnium insert in the middle of the cathode. The hafnium insert is used for both its advantageous electron emission properties and advantageous wear properties.

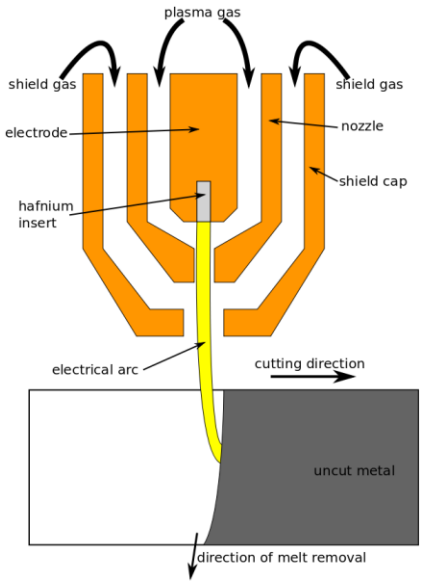

Figure 1.1. Schematic of plasma arc cutting process.

During the cutting process, an electric arc is struck between the cathode and the work piece, which serves as the anode. This electric arc is carried by the working gas, which flows through the nozzle and is ionized into a plasma. As the arc and plasma pass through the very narrow nozzle bore, it is tightly constricted, causing immense Joule heating, which raises the temperature to as high as 35000K. Due to the high temperatures present, the nozzle and electrode are water cooled to protect against melting. The working gas is given a swirl component as it enters the nozzle, which serves to stabilize and further constrict the arc inside the nozzle. Due to the constriction of the nozzle and the dramatic increase in temperature, the plasma gas is also accelerated to supersonic speeds inside the nozzle.

As the plasma gas and electric arc exit the nozzle, they pass through a small standoff distance between the cutting torch and the work piece. In this region, the plasma jet passes through a shock, or series of shocks, and the velocity becomes subsonic again. It should be noted that the low density of the hot gas increases the speed of sound, so that while the velocity is subsonic, it is still of the order of thousands of meters per second. In this region, ambient gas is also entrained into the plasma jet. To protect against this, a cold, co-flowing shield gas is employed.

The work piece has a slot cut into it, called the kerf. The plasma gas and electric arc pass into this kerf, where the arc terminates as it attaches to the kerf wall. This results in an enormous heat flux to the kerf wall due to both convective and radiation heat transfer from the plasma gas as well as localized heat transfer from the arc attachment. This heat flux rapidly melts the kerf wall and the high velocity plasma gas flowing through the kerf exerts a drag force which accelerates this molten metal out of the kerf. Thus, as the plasma torch is moved across the work piece, it cuts a slot through the metal.

In the cutting of mild steel, the plasma gas used is often oxygen. This is beneficial because of an exothermic oxidation reaction between oxygen and iron which contributes a significant portion of heat for melting the work piece. The iron oxide also has lower values of surface tension and viscosity than pure iron, which allows it to be more easily removed.

1.3. Motivation

From an industrial perspective, there is always an interest in improving cut speed while maintaining or improving cut quality. Improved cut speed leads directly to increased output in the many areas of manufacturing that plasma arc cutting is applied. Furthermore, improved cut quality leads to less or no machining requirements after the part has been cut. Thus, improving cut quality can also increase output.

In describing cut quality, there are three main measures: 1) bevel angle, 2) cut striations, and 3) dross adhesion. An ideal cut should be perfectly square but in reality, the kerf narrows at the bottom of the work piece, which leaves a bevel angle on the edge being cut. Due to the swirl component of the plasma flow, there is asymmetry in the kerf and the two sides are not identical. This gives rise to a "good side" and a "bad side", where cutting must be performed in the correct direction so the good side is on the finished part and the bad side is on the scrap metal. The physical processes underlying this asymmetry, however, are unknown.

The cut striations are a "waviness" that appears on the face of the cut. This is not unique to plasma arc cutting, but also appears to a greater or lesser extent in the other cutting methods described in section 1.2. To a certain extent, these striations are innocent, but they can become problematic if they are too pronounced and prevent two cut parts from fitting snuggly against each other. These striations clearly come from some sort of periodicity in the cut process, although it is unclear whether the periodicity develops from the plasma flow, the melting, the melt flow, or some combination thereof.

The dross adhesion is perhaps the most serious of the cut quality measures. In some situations, dross adheres to the bottom of the work piece. This dross must then be scraped or ground off as an additional step in the manufacturing process. This slows the production rate and requires additional workers to remove the dross, making it highly undesirable. The formation of dross is closely related to cut speed, which is a relationship that has been well characterized. For a given set of process parameters (current, gas flow rates, plasma gas type, nozzle design) there is a cut speed above which dross adheres. There is also a cut speed below which dross adheres. Thus, there is a range of cut speeds in between for which dross free cutting is achieved. Furthermore, the characteristics of the low speed dross and the high speed dross are different. The low speed dross is more chaotic and unpredictable. It generally consists of larger globules, which are easily scraped off. The high speed dross on the other hand appears more consistently and adheres more tightly to the work piece, requiring grinding for removal. This dross adhesion is certainly related in some way to the surface tension of the metal, the wettability of the work piece underside, and the drag force of the plasma on the melt. The complicated interaction between these effects, however, is not fully understood. Thus, while the presence of dross adhesion can be experimentally predicted as a function of cut speed, the underlying physics leading to dross adhesion are not well understood.

In many cases, an increase in cut speed is more important than an improvement in cut quality. There are two separate limits on the maximum cut speed. The first is the point at which high speed dross forms. To increase the maximum cut speed imposed by the high speed dross, a detailed understanding of the high speed dross must be obtained. If the presence of high speed dross is acceptable in a particular application, then the limit on the maximum cut speed is the point at which the cut no longer extends all the way through the work piece. This could be due either to an insufficient heat flux to melt through the work piece, an insufficient drag force to remove the molten metal, or a combination of the two. Again, a detailed understanding of the physical phenomena is necessary to understand how this limit can be pushed higher.

Thus, from an industrial standpoint, research into plasma arc cutting is well justified. There are, however, also purely scientific reasons for studying plasma arc cutting. Much research in the area of thermal plasma arcs has focused on free burning arcs. While this is certainly a valuable test bed for understanding plasma physics it is a rather simple geometry. The anode attachment is an area of particular interest in thermal plasma research and the physics of such an anode attachment within the geometry of a kerf is unique and has not yet been well characterized.

1.4. Scope of Thesis

In light of both the scientific and industrial interest in the work piece region of plasma arc cutting, the present work focuses on the physical phenomena in this region. Due to the high temperature, strong plasma radiation, and enclosed geometry, this area is very difficult to study experimentally. Thus, the problem is approached with numerical simulation.

In formulating a model, it is necessary to first consider what physics is present and then to decide what can be included in the model. In the work piece region, there are many interconnected phenomena, illustrated in figure 1.2. In the left most box of figure 1.2, a plasma model will give the temperature and velocity distribution throughout the inside of the kerf. From this plasma model, a heat flux to and drag force on the kerf wall can be calculated. This heat flux and drag force will determine the melting of the work piece and removal of the molten metal. The manner in which the work piece is melted and removed determines the shape of kerf, which, in turn, is needed in order to model the way the plasma flows through the kerf. In addition, the chemistry in the melt contributes to both the heat flux, through the exothermic oxidation reaction, and the melt removal, through modifying the surface tension and viscosity.

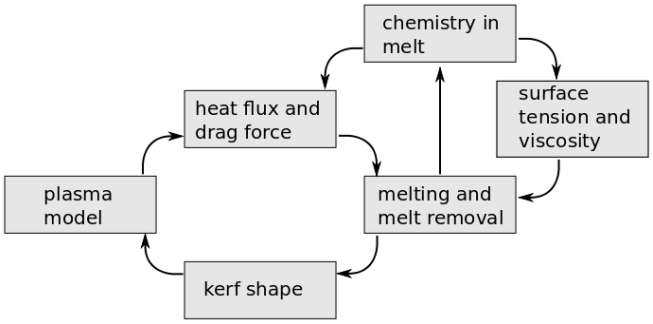

Figure 1.2. Schematic of modeling dependencies in work piece region of plasma arc cutting process.

The inclusion of all of these elements in a single model is beyond the scope of a single thesis. Thus, experimental data and assumptions are used to decouple some elements from each other, as shown in figure 1.3. Instead of predicting the kerf shape from the model, the kerf shape is measured experimentally. The bulk of the present work then consists of numerically modeling the flow of plasma through this kerf. This plasma model gives the temperature, velocity, and current density distribution throughout the inside of the kerf. From this, the heat flux to and drag force on the kerf walls are calculated. Qualitative conclusions about the melting and melt flow can then be drawn. A certain amount of oxidation is assumed, giving an additional energy source

into the melt. It is also assumed that the surface of the melt is entirely oxidized and thus the surface tension corresponds to that of iron oxide.

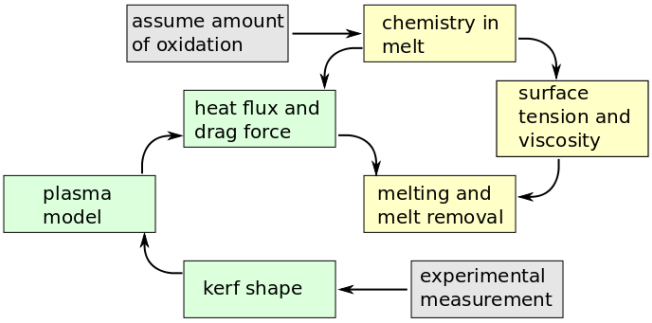

Figure 1.3. Decoupling of modeling dependencies. Grey boxes indicate experiment or assumption. Green boxes indicate quantitative results. Yellow boxes indicate qualitative results.

While the cutting process is clearly a transient process, it becomes a steady process when viewed from the reference frame of the torch. In other words, the torch is viewed as stationary while the work piece moves at a constant speed beneath it. In this way the kerf shape below the torch is also constant. While this allows the use of a steady geometry, the plasma flow is solved using a transient model so that the possibility of a quasi-steady state with a steady oscillation is allowed.

Two main approaches are utilized in modeling the plasma flow. The first of these is the local thermodynamic equilibrium (LTE) formulation, which is the most widely used method of modeling thermal plasmas. This assumes that the kinetic energy of all atoms, ions, and electrons can be described by a single temperature. While this assumption most likely holds in the center of an arc, it falls short in the arc fringes where there are insufficient collisions between electrons and heavy species to equilibrate the temperatures. This shortcoming becomes problematic when dealing with electrode attachments. The low temperature boundary layer near the electrode walls leads to a layer of very low electrical conductivity. The arc is then unable to bridge across this boundary layer and the modeled arc does not attach where a physically accurate model should.

To address the short coming of the LTE formulation, a second approach is applied in the form of a two temperature model. This is not a new technique in thermal plasma modeling literature, but it presents significant additional difficulties, which have not all been thoroughly explored in the literature. In this formulation, the molecules, ions, and atom, called the heavy species, are assumed to have a kinetic energy that is described by a heavy species temperature and the electrons are assumed to have kinetic energy that is described by a separate electron

temperature. Thus, at any given point there are two separate temperatures governed by two separate energy equations. This formulation allows for a high electron temperature in the arc fringes and next to the electrode walls. Because the electrical conductivity is most heavily dependent on the electron temperature, this allows for a sufficiently high electrical conductivity all the way up to the electrodes, leading to a physically accurate arc attachment.

The plasma model is implemented using the general purpose, open source, CFD package OpenFOAM [1]. It is important that the code be open source because significant changes are needed in order to incorporate plasma effects. This is the reason for rejecting a commercial code such FLUENT, which is essentially a black box that has only limited interfaces with which to modify the model. At the same time, OpenFOAM has huge benefits when compared to a code written from scratch because it is not necessary to redevelop the parts that deal with equation discretization, mesh generation and overall code structure. Furthermore, once the solver is developed in OpenFOAM, the general purpose nature of the code structure allows the plasma solver to be applied to any other geometry of interest. The major work required for implementing a plasma model in OpenFOAM consists of adding the code needed to look up the properties from a table as a function of two temperatures, as well as the pressure. The additional equations and source terms particular to plasma modeling can then be added to an OpenFOAM solver using a high level, OpenFOAM specific syntax, which is very easy to use.

This thesis will first discuss the state of current plasma arc cutting research and plasma modeling research in chapter 2. The formulation of the mathematical model is then given in chapter 3. This includes the necessary governing equations but also gives particular attention to the formulation of the two energy equations. Chapter 4 gives the calculations used to obtain the thermodynamic and transport properties that appear in the equations of chapter 3. This is a particularly important part of any plasma model because the properties vary strongly in a non-linear fashion with respect to temperature. Chapter 5 discusses the implementation of the model with respect to numerical methods and model stability. The application of the plasma model to the plasma arc cutting process is described in chapter 6 and the results are shown and discussed in chapter 7. Finally, chapter 8 gives a summary of the results and draws conclusions.

Chapter 2

Background and Relevant Literature

2.1. Plasma Modeling

2.1.1. Beginnings of plasma modeling

The invention of computers has led to the ability to study fundamental physics through numerical simulations. As the speed and capacity of these computers has increased, the quality of numerical simulations has improved as well. In the quest to better understand fluid flow and heat transfer, the field of computational fluid dynamics (CFD) was developed. One of the most notable works in the field of CFD is the book "Numerical Heat Transfer and Fluid Flow" by Patankar [2]. This book lays out the finite volume method (FVM) in which a domain of interest is broken into a large number of small volumes. Governing equations are then discretized to solve the flow of mass, energy, and other variables between the volumes. Patankar also presents the SIMPLE algorithm (Semi-Implicit Method for Pressure Linked Equations) for resolving the coupling between the pressure and the velocity. This algorithm, or slight variations thereof, is still used in almost all general purpose CFD codes for solving steady state problems. This SIMPLE algorithm can also be applied to transient problems, but it is computationally expensive because significant iteration is needed at each time step. An alternative algorithm was developed for transient problems by Issa [3] called the PISO algorithm (Partially Implicit Split Operator). This PISO algorithm is used in most general purpose CFD codes for solving transient problems.

These CFD techniques have also been expanded to the modeling of thermal plasmas. Initially, these models made very restrictive assumptions. Local thermodynamic equilibrium (LTE) was maintained which assumes that the translational energy of all species is described by a single a temperature and that all chemical reactions proceed to equilibrium instantaneously. This LTE assumption allows the calculation of the thermodynamic and transport properties as a

function of temperature and pressure using statistical mechanics and gas kinetics theory [4-6]. These early plasma models were also solved as steady-state problems and had very simple geometries, generally limited to two dimensions. Furthermore, a single plasma gas was used, neglecting the influence of metal vapors and mixing with ambient gases. An excellent example of such a model is found in the work of Hsu et al. [7]. A steady state, free burning arc in pure argon is modeled in two dimensions assuming axisymmetry. Despite the restrictive assumptions, however, quite good agreement was found when compared to experiments. Thus, it is clear that even such a basic model is a valuable tool for studying plasma phenomena, despite the restrictive assumptions.

2.1.2. Advancements to plasma modeling

The more recent advancements in the field of thermal plasma modeling are roughly broken into three categories by Murphy et al. [8]: 1) expansion to complicated three dimensional geometries and transient phenomena, 2) improvements to plasma theory, including chemical and thermal non-equilibrium and multiple plasma gases that are unevenly mixed, and 3) multiphase modeling that includes the electrodes, molten droplets, and particles into the model. The third of these does not directly apply to the present work because only the plasma phase will be modeled here. This will, however, be important for future work in the area of plasma cutting because the flow of the molten metal is of particular interest and should be included in future modeling work. Selected advanced techniques from categories one and two will be used in the present work, so they will be reviewed here.

2.1.2.a. 3D and transient phenomena

The expansion to three dimensional geometries requires far more cells in order to adequately describe the geometry. Furthermore, a small time step and long run time are needed in order to capture transient phenomena. Thus, it is apparent that such three-dimensional geometries and transient phenomena require immense computational resources. Advances in parallel computing have provided these resources and allowed the development of these models.

One such model is found in the work of Trelles et al. [9-14]. They model the interior of a non-transferred plasma spray torch in which the arc stretches between a central cathode and the wall of the nozzle, which serves as the anode. Such a configuration is an inherently 3D process because the arc attaches to only one side of the nozzle at a time, creating an asymmetry. Furthermore, it is an inherently transient process because this arc attachment moves across the

anode over time. Trelles' work nicely captures both the 3D and transient phenomena finding reasonable arc attachment behavior as determined by comparison with experimental voltage traces. Furthermore, the plasma jet emitted from the torch showed similar behavior in both the model and experimental high speed images.

2.1.2.b. Non-equilibrium plasma phenomena

While the first category of improvement has largely piggy-backed on general improvements in CFD techniques, the second category of improvements is directly related to the theory of plasma physics. The most common form of non-equilibrium in thermal plasma is the two-temperature assumption. Under the two-temperature assumption it is noted that the electrons have much less mass than the remaining heavy species. As such, the translational energy of the electrons does not equilibrate with the heavy species as quickly and can deviate significantly from that of the heavy species. Thus, it is assumed that the translational kinetic energy of the electrons follows a Maxwellian distribution described by an electron temperature and the translational energy of the heavy species follows a separate Maxwellian distribution described by a heavy species temperature. The conservation of energy is then described by two separate energy equations that are coupled by the exchange of energy between the electrons and the heavy species.

One of the earliest examples of such a model is the two-temperature model of a free burning arc in argon [15]. This work found that the electron temperature is sometimes higher than the heavy species temperature. This is most noticeable in the fringes of the arc. These results were also compared to experiments and better agreement was found with the two-temperature model than with the LTE model. There have been a number of other such two temperature models, but there is not yet a consensus in the literature as to how the two temperature equations must be formulated. As outlined by Freton et al. [16], there is disagreement in the literature as to whether ionization energy should be stored with the electrons or the heavy species. There is also disagreement about whether the reactive component of thermal conductivity should be attributed to the heavy species or the electrons. It is concluded by Freton et al. that the ionization energy and associated reactive thermal conductivity should be attributed to the electron energy equation while the dissociation energy and associated reactive thermal conductivity should be attributed to the heavy species energy equation. This is still not entirely correct. Rather, the ionization energy can be attributed to either the electrons or the heavy species, so long as the reactive thermal conductivity is attributed the same way. Furthermore, Freton et al. do not consider that there is a

reactive heat flux associated with both the electron temperature gradient and the heavy species temperature gradient, so it is important to specify to what temperature gradient the reactive thermal conductivity relates. The formulation proposed in the present work will be described in chapter 3.

While the two-temperature assumption begins to capture the non-equilibrium phenomena present in a thermal plasma, it still assumes chemical equilibrium. This chemical equilibrium assumption can be dropped, however, to allow chemical non-equilibrium. In this case, an additional species conservation equation is solved for each species present. The reaction rates of these species with each other are included to give the number densities of each species at every point in the plasma. The two-temperature assumption is always included when a chemical non-equilibrium model is used. Conveniently, the complicated reactive thermal conductivity coefficient does not appear in the chemical non-equilibrium model because the reactive energy is governed by the reaction rates in the species conservation equations.

Such chemical non-equilibrium models are rare because of the dramatic increase of computation needed. Besides the additional species conservation equations that need to be solved, the thermodynamic and transport properties are a function of the plasma composition as well as the temperature and pressures. This requires either much larger lookup tables or that the properties be calculated "on the fly", both of which dramatically increase computation time. Furthermore, it is also necessary to look up or calculate a large number of diffusion coefficients that describe how the species diffuse relative to each other. In the work of Ramshaw and Chang[17, 18], a "self consistent effective binary diffusion coefficient" has been utilized which reduces the number of necessary diffusion coefficients to the number of species present. This dramatically improves computation time, but has not been widely adopted in thermal plasma modeling literature. In the work of Haidar[19], the effects of species diffusion relative to each other is neglected and only transient and advective effects on the species are considered. This effectively eliminates the need to compute the diffusion coefficients, further improving computation time. Using this formulation, deviations from chemical equilibrium were found in the region near the cathode.

A more minor form of chemical non-equilibrium that has been found extremely valuable is to include multiple plasma gases that are not fully mixed with each other. This is particularly useful when considering the effects of metal vapors emitted from the electrodes into a plasma arc. Instead of considering the diffusion of all of the plasma species relative to each other, the diffusion of only the two gases relative to each other is considered. This is done with the widely

used method of "combined diffusion coefficients" developed by Murphy [20, 21]. In this method, a combined ordinary diffusion, combined temperature diffusion, and combined pressure diffusion coefficient are calculated which can then be used to give the flux of one gas relative to the other. There is then only one additional gas conservation equation to govern the flow and diffusion of one plasma gas relative to the other.

The most common application of the combined diffusion coefficient method involves the presence of metal vapors emitted from the work piece in plasma arc welding [22]. The two major effects of the metal vapor concern the electrical conductivity and the radiation. The addition of even a small amount of metal vapor dramatically increases electrical conductivity and radiative emission. The increased electrical conductivity leads to a more diffuse anode attachment, while the increased radiative emission cools the plasma.

2.1.3. Electrode considerations

There is a thin layer across the electrodes called the "sheath" that behaves quite differently from the remainder of the plasma. Because the behavior is so different, the standard thermal plasma models no longer apply in this region. As such, these sheath effects are generally neglected and replaced by some sort of simplifying assumptions. This is reasonable because the sheath has relatively little effect on the flow of the plasma as a whole. The assumptions used at the electrodes, however, must be considered.

Gleize et al. [23] summarize the treatment of the cathode into four categories: 1) Impose a reasonable current density profile across the cathode face. 2) Set a voltage drop between cathode and anode, which is updated in an iterative fashion until the correct total current is reached. 3) Solve the flow of current through the solid cathode so that the current density profile at the cathode/plasma interface is determined by the model. 4) Use a detailed model of the cathode sheath. Of these four methods, method one and three are most commonly used when the primary interest is on a particular plasma process rather than electrode phenomena. Method one is used in the present work.

With the current density specified on the cathode, the electric potential is generally set equal to zero on the anode, effectively grounding it. This, however, can give rise to difficulties in modeling. When the LTE assumption is used, the temperature in the thermal boundary layer falls below the first ionization temperature. When this happens the electrical conductivity falls to zero in a layer next to the anode preventing the arc attachment from forming, which is a physically incorrect result. Lowke and Tanaka [24] propose an "LTE-diffusion approximation" that resolves

this by requiring that the mesh size be sufficiently large in front of the anode, where the size is set by a "diffusion length". This was found to work quite well in a free-burning arc model. If such a mesh size restriction is unreasonable, Trelles et al. [12] propose a method in which the electrical conductivity is artificially increased in a thin layer across the surface of the anode. Once the artificial electrical conductivity was increased past a certain point further increases were found to have relatively little effect on the final result, indicating that the result is not being predetermined by the artificial increase. The best method, however, for dealing with this difficulty is to use a two-temperature model instead of an LTE model [11]. When the two-temperature assumption is used, the electron temperature maintains a high value all the way up to the anode. The electrical conductivity is most dependent on the electron temperature, so the electrical conductivity then maintains a high value all the way up to the anode, allowing the physically accurate attachment result.

2.2. Plasma Arc Cutting

The use of an electrical arc to cut metal is first documented in a patent by Gage[25] when it was discovered that constricting a welding arc dramatically increased the heat transfer, leading to a cutting process instead of a joining process. Early improvements were obtained from experiments on the cut speed and working gas. In particular, it was discovered that when oxygen is included in the working gas, either using air or pure oxygen, the cutting process is enhanced[26, 27]. Correlations between the cut speed and the appearance of dross were also established [28]. For a given set of operating parameters, dross appears if the cutting speed is too slow or if the cutting speed is too fast, giving rise to the terms "low speed dross" and "high speed dross". Between these two cut speeds is a "dross free cutting window" which produces preferable cut quality. Furthermore it was noticed that the high speed dross is characteristically different from the low speed dross, being much harder to remove. Nemchinsky[29] established a physical basis for determining the upper and lower limits of this dross free window. He proposes that the appearance of dross can be predicted as a function of the non-dimensional Weber number, $We = \frac{\rho V^2 \Delta}{2\sigma}$ where ρ is the melt density, V is the velocity of the melt, Δ is a characteristic length, and σ is the surface tension of the melt.

While the work piece being cut is ultimately the most important area of the over all process, a significant amount of valuable research has focused on the nozzle region. This is a natural place to start because it is the most easily controlled part of the process. Ramakrishnan et

al. [30, 31] consider the effect of the nozzle bore diameter on the final cut. They use a "two-zone" model in which the electrical arc in the nozzle bore is approximated as a high temperature, low density center zone which carries most of the electrical current and a low temperature, high density outer zone which carries most of the mass flow. From this analysis, they observed that the low density center zone "clogs" the nozzle creating a huge pressure drop through the nozzle bore which is responsible for accelerating the plasma to supersonic speeds. Furthermore, the narrowing of the nozzle bore leads to an even narrower center zone carrying a much high current density which increases the power of the arc. Nemchinsy [32] improves on the two-zone model by solving a two dimensional model of plasma flow in the nozzle bore, giving the distribution of temperature, pressure, velocity, and voltage. He finds that a significant portion of the energy generated by the arc is lost in radiation and the rest passes out the nozzle as a high temperature plasma with only a very small part conducted to the nozzle walls. Gonzales-Aguilar et al. [33] expands this model yet further, providing what can be considered the first true CFD model of plasma arc cutting. This is a fairly simplified plasma model, assuming 2-D, laminar, LTE flow. It includes the entire nozzle geometry, however, and also extends to the region in front of the nozzle. The presence of the kerf is entirely ignored and the model merely assumes that the plasma jet impinges on a flat plate. Despite the many assumptions, this model is extremely valuable, giving the distribution of temperature, pressure, velocity and voltage throughout the nozzle. Freton et al. [34, 35] expand this model further, including turbulence in the plasma model and expanding the geometry to include a hole in the work piece, through which the electrical arc passes. The 3-D nature of the kerf shape is still not considered, but the hole geometry is far more accurate than the simple impingement on a flat plate. The effects of thermal and chemical non-equilibrium inside the nozzle are considered by Ghorui et al. [36] although the geometry is cut off at the exit of the nozzle. The presence and importance of non-equilibrium effects are demonstrated in this work although the results at the exit of the nozzle are suspect, due to unreasonable large increases of velocity (doubling velocity over one grid spacing). The most extensive modeling of plasma flow in the nozzle of a plasma arc cutting process is found in the work of Colombo et al. [37]. This work focuses exclusively on flow inside the nozzle, but the geometry is extended a short distance outside of the nozzle to ensure an accurate boundary condition at the exit of the nozzle. Various geometries and cutting parameters are explored demonstrating the power of numerical modeling to understand how nozzle design affects the cutting process.

While theory and numerical modeling is the primary means of understanding plasma flow inside the nozzle, it can be studied experimentally outside of the nozzle. Spectroscopy is a popular method of studying plasma in the region between the nozzle and the work piece [16, 34, 38-41]. It is limited to this region, however, because of the line-of-sight requirements. Where it can be applied, these spectroscopic techniques provide an experimental measurement of the temperature profile, which, due to high temperatures, cannot be found using any other experimental technique. It is generally assumed that a higher peak temperature and a narrower, more collimated, arc column will result in a better cut process. Thus, spectroscopy can be used to study the effect of the torch parameters on the temperature profile. Furthermore, spectroscopy of the arc column can be used for comparison with numerical modeling results [16, 34].

High speed imaging is also widely used to study the plasma cutting process. In the region between the nozzle and the work piece, images of the arc show various bright and dim bands, which can be correlated to shock structure in front of the nozzle [41]. This shock structure is influenced by nozzle conditions and can be used to validate a numerical model [34]. Images utilizing a very short shutter time can also be used to study transient processes such as arc initiation and work piece piercing [42, 43]. The arc ignition particularly is very difficult or impossible to study with modeling or spectroscopy, making the high-speed images extremely valuable for understanding the process.

In the area where the plasma arc and work piece interact, high speed imaging has been used to locate the position and character of arc attachment. Bemis and Settles [44, 45] use an ultraviolet filter to image a slow speed "edge cut" that only skims the edge of the test work piece. A very bright jet, corresponding to metal vapors ejected from the work piece, is seen at the bottom edge of the work piece, indicating an attachment on the bottom of the work piece. The slow cut speed, however, may be responsible for the arc attachment location found. Teulet et al. [46] use a neutral filter and image the front of the kerf through the arc. A bright spot is found part way down the kerf, which is interpreted as the location of the arc attachment. Kavka et al. [47] image the arc from the back of the kerf and find a moving attachment, which deviates from other results reported in literature. It should be noted, however, that voltage traces taken by Kavka et al. support the moving attachment results. Colombo et al. [48] also finds a moving attachment but only for slower cut speeds. As the cut speed increases, the arc attachment becomes stationary near the top of the work piece. There are two additional studies of the arc attachment that do not use imaging. One [49] uses thermocouples embedded in the work piece at various depths. The depth that records the highest temperature is assumed to be the depth of the arc attachment. This gives

an attachment in the middle to upper portion of the kerf. The other [50] uses the arc voltage as a function of work piece thickness to determine the location of the attachment, finding a stationary attachment in the upper portion of the kerf.

While a range of different results are found for the arc attachment location, a few trends are apparent: 1) A faster cut speed will move the arc attachment higher in the kerf. 2) The arc attachment is generally stationary, which can be verified by the voltage trace. 3) A sufficiently low cut speed seems to lead to a moving attachment. 4) Varying cut parameters will, in general, affect the arc attachment location. In the present work, the cutting parameter corresponds most closely to [50], so modeling results will be compared to that work.

Chapter 3

Mathematical Formulation of the Model

3.1. Assumptions

In any numerical simulation it is important to carefully formulate the mathematical model. In order to do this, simplifying assumptions must be made. In the present work, the first assumption is that the plasma gas behaves as a continuum fluid. This is the fundamental assumption underlying the field of computational fluid dynamic (CFD), which allows the use of the standard continuity, Navier-Stokes, and traditional energy conservation equations. This assumption is valid so long as the cell size of the mesh contains enough particles that no single particle is distinguishable, which is most certainly true for this work.

The next assumption is that the plasma gas passing through the torch is pure oxygen and discharges into an environment of pure oxygen. It is quite certain that any contamination in the gas or copper vapors from the nozzle is minimal and would not affect the results. In reality, however, the torch generally discharges into an air environment, making this assumption not quite correct. It is suspected, however, that including the air environment would have only a small effect on the results while creating huge difficulties in modeling. The effect of iron vapor emitted from the work piece, however, might be important for the final model. As such, the model allows for the emission of iron vapors from the work piece and the diffusion of these vapors through the plasma.

The plasma gas, consisting of oxygen and iron, is made up of a number of different molecular, atomic, and ionic species. These species chemically interact with each other producing a composition of the different species. For this work, chemical equilibrium is assumed, which is to say that chemical reactions between species progress to equilibrium nearly immediately. Thus, the chemical composition depends only on the temperature, pressure and ratio of iron to oxygen.

While chemical equilibrium is widely used in thermal plasma modeling, there would be small improvements in the results of the model if chemical non-equilibrium was allowed. The benefits, however, are not worth the extreme level of complexity added to the model.

The reactions of the numerous species give rise to a great amount of reactive energy. In the calculation of thermodynamic and transport properties, it will be apparent that it is necessary to attribute this reaction energy to either the electrons or the heavy species. In this work, the reactive energy is attributed to the heavy species.

The widely used assumption of quasi-neutrality is also used in this work. This states that the electrons and ions do not separate from each other. In other words, at every point in the plasma, there are enough electrons to balance out every ion and no space charge forms. This is an accurate assumption through much of the plasma , although it breaks down in the thin layer next to the electrodes called the "sheath region". Because this region is so thin, however, the sheaths are simply ignored except to take note of an extra sheath voltage drop when reporting the arc voltage in the model.

The flow of electrical current in a plasma is carried by the electric field driving electrons in one direction and positively charged ions in the other direction. Because the electrons have a much higher mobility than the ions they are responsible for carrying almost all of the current. In this work, the ion contribution is neglected and it is assumed that electrons carry all of the current.

It is assumed that the kinetic energy of all the species follows a Maxwellian distribution described by a single temperature. This assumption, along with the chemical equilibrium assumption is referred to as Local Thermodynamic Equilibrium (LTE). The LTE assumption is widely used in thermal plasma modeling and has been shown to be generally valid in the center of arcs. In the fringes of the arc, however, it is likely that the energy of the electrons deviates from the energy of the heavy species because the electrons are so much less massive. This gives rise to a second competing assumption in which the heavy species follow a Maxwellian distribution described by a heavy species temperature, T_h, and the electrons follow a separate Maxwellian distribution described by an electron temperature, T_e. This is referred to as the two temperature assumption and is less frequently used in plasma modeling because it adds complexity in the form of two separate but coupled energy equations. Both the LTE and the two-temperature assumptions will be used here and they will be compared to each other.

It is assumed that the plasma flow is laminar. This is likely a good assumption in the nozzle bore and in the kerf, but there are certainly turbulent effects present in the area between

the work piece and the nozzle. The inclusion of a turbulence model, however, is beyond the scope of this work, although it could provide a valuable direction for future work.

Viscous dissipation is neglected as it is very small in comparison to the dominant joule heating and radiation source terms. Gravitational forces are also neglected as they are very small compared the inertial and viscous forces of the arc jet, which reaches velocities of thousands of meters per second.

3.2. Governing Equations

The widely used fluid dynamic and heat transfer equations are suitably modified for modeling plasma flow and governing electro-magnetic equations are added. The mass conservation equation is

$$\frac{\partial \rho}{\partial t} + \nabla \cdot \rho \vec{u} = 0 \tag{3.1}$$

The momentum conservation equation is

$$\frac{\partial \rho \vec{u}}{\partial t} + \nabla \cdot \rho \vec{u}\vec{u} = -\nabla p + \nabla \cdot \mu \nabla \vec{u} + \vec{j} \times \vec{B} \tag{3.2}$$

When the LTE assumption is used, the energy equation is

$$\frac{\partial \rho h}{\partial t} + \nabla \cdot \rho \vec{u} h = \nabla \cdot \vec{q} + \frac{Dp}{Dt} + \frac{5}{2}\frac{k_b}{e}(\vec{J} \cdot \nabla T) + \vec{j} \cdot \vec{E} - \dot{Q}_r \tag{3.3}$$

In these equations, ρ is the mass density, $\vec{u}$ is the mass averaged velocity, p is the pressure, μ is the dynamic viscosity, $\vec{j}$ is the electrical current density, $\vec{B}$ is the magnetic field, h is the specific enthalpy, $\vec{q}$ is the diffusive heat flux, k_b is the Boltzmann constant, e is the charge of an electron, $\vec{E}$ is the electric field, and $\dot{Q}_r$ includes all radiation heat loss. Most of the terms in these equations are familiar from the standard heat and fluid flow theory, but a few are particular to plasmas. The final term on the right hand side of the momentum equation accounts for the Lorentz force. The third and fourth terms on the right hand side of the energy equation account for energy flowing through the electrical current causing electrons to drift and the energy produced through Joule heating.

When the two temperature assumption is used, there are two energy equations accounting for the energy carried by the electrons and the energy carried by the heavy species.

$$\frac{\partial \rho h_e}{\partial t} + \nabla \cdot \rho \vec{u} h_e = \nabla \cdot \vec{q}_e + \frac{Dp_e}{Dt} + \frac{5}{2}\frac{k_b}{e}(\vec{j} \cdot \nabla T_e) + \vec{j} \cdot \vec{E} - \dot{Q}_r - \dot{Q}_{eh} \tag{3.4}$$

$$\frac{\partial \rho h_h}{\partial t} + \nabla \cdot \rho \vec{u} h_h = \nabla \cdot \vec{q}_h + \frac{Dp_h}{Dt} + \dot{Q}_{eh} \tag{3.5}$$

where h_e is the enthalpy contained in the electrons per mass of plasma, h_h is the enthalpy contained in the heavy species per mass of plasma, $\vec{q}_e$ and $\vec{q}_h$ are the diffusive energy fluxes, p_e and p_h are the partial pressures of electrons and heavy species, and $\dot{Q}_{eh}$ accounts for the exchange of energy between electrons and heavy species.

In calculating the electro-magnetic variables, an electric potential, ϕ, is first defined such that the electric field is the gradient of the electric potential.

$$\vec{E} = \nabla \phi \tag{3.6}$$

The current density is easily calculated from the electric field as

$$\vec{j} = \sigma \vec{E} = \sigma \nabla \phi \tag{3.7}$$

where σ is the electrical conductivity. Because of the quasi-neutrality assumption, no charge builds up at any point, so the divergence of the current density must be zero everywhere. This gives the governing equation for the electric potential in the form of a Laplacian equation.

$$\nabla \cdot \sigma \nabla \phi = 0 \tag{3.8}$$

A magnetic vector potential, $\vec{A}$, is also defined such that the magnetic field is the curl of the magnetic potential.

$$\vec{\mathrm{B}} = \nabla \times \vec{\mathrm{A}} \tag{3.9}$$

The governing equation for the magnetic potential is given by Ampere's law which takes the form [51]

$$\nabla^2 A = -\mu_0 \vec{j} \tag{3.10}$$

where μ_0 is the permeability of free space.

In order to resolve the diffusion of iron vapors through the oxygen plasma, a conservation equation for the mass fraction of the iron vapor is solved.

$$\frac{\partial \rho \overline{Y_{Fe}}}{\partial t} + \nabla \cdot \rho \vec{u} \overline{Y_{Fe}} = -\nabla \cdot \overline{J_{Fe}} \tag{3.11}$$

where $\overline{Y_{Fe}}$ is the mass fraction of iron vapors and $\overline{J_{Fe}}$ is the mass diffusion flux of the iron vapors. Following the combined diffusion coefficient method of Murphy [20], the mass diffusion flux is written as

$$\overline{J_{Fe}} = \frac{n^2}{\rho}\overline{m_O}\left\{\overline{D_{FeO}^{x}}\nabla\overline{x_O} + \overline{D_{FeO}^{p}}\nabla\ln(p)\right\} - \frac{1}{\overline{m_{Fe}}}\overline{D_{FeO}^{T}}\nabla\ln(T) \tag{3.12}$$

where n is the number density of particles, $\overline{m_O}$ is the average mass of the oxygen species, $\overline{m_{Fe}}$ is the average mass of the iron species, and $\overline{D_{FeO}^{x}}$, $\overline{D_{FeO}^{p}}$, and $\overline{D_{FeO}^{T}}$ are the combined diffusion coefficients, which are calculated in chapter 4.

3.3. Details of the Energy Equation

3.3.1. Diffusive heat fluxes

The diffusive heat fluxes appearing in the energy equations require particular attention. In the LTE formulation, this is simply the heat conduction from Fourier's law

$$\vec{q} = \kappa\nabla T \tag{3.13}$$

where κ is the thermal conductivity calculated in chapter 4.

This becomes more complicated for the two temperature equation. As detailed in chapter 4, the thermal conductivity in the two temperature formulation can be broken into four components: 1) the translational thermal conductivity of the heavy species, 2) the translational thermal conductivity of the electrons, 3) the reactive thermal conductivity with respect to the electron temperature gradient, and 4) the reactive thermal conductivity with respect to the heavy species temperature gradient. These four coefficients correspond to four heat fluxes that must be attributed to either the electron energy equation or the heavy species energy equation. Clearly, the heavy species translation term belongs with the heavy species energy equation and the electron translational term belongs with the electron energy equation. It might be tempting to split the reactional terms between the two equations so that the electron temperature does not appear in the heavy species energy equation. Because the reactive energy is assumed to be stored with the heavy species, however, all reactive diffusion heat fluxes belong with the heavy species diffusive heat flux. Thus, $\vec{q}_e$ and $\vec{q}_h$ take the forms

$$\vec{q}_e = \kappa_e\nabla T_e \tag{3.14}$$

$$\vec{q}_h = \kappa_h\nabla T_h + \kappa_{rh}\nabla T_h + \kappa_{re}\nabla T_e \tag{3.15}$$

3.3.2. Pressure terms

The treatment of the pressure term in the energy equation will be given particular attention here. This appears in equation 3.3 as the material derivative of the pressure and is the dominant term that couples the pressure to the temperature. In the two-temperature formulation, the pressure term must be broken up between the electrons and the heavy species. Almost universally, this is done by using the electron partial pressure in the electron energy equation and the heavy species partial pressure in the heavy species equation, where the partial pressures are defined as

$$p_e = n_e k_b T_e \tag{3.16}$$

$$p_h = \sum_{i \neq e} n_i k_b T_h \tag{3.17}$$

where n_i is the number density of species i, and k_b is the Boltzmann constant. This is the method used in the formulation of equations 3.4 and 3.5. An important and necessary trait of this formulation is that the sum of the electron and heavy species pressure terms equals the total pressure term.

$$\frac{Dp_e}{Dt} + \frac{Dp_h}{Dt} = \frac{Dp}{Dt} \tag{3.18}$$

An alternative method of dividing up the pressure term is suggested by the question: Can the pressure term give rise to thermal non-equilibrium? It seems unlikely that the pressure term would contribute more or less kinetic energy to the electrons than the heavy species. If this is the case, then the pressure must be divided in such a way that that it does not change the non-equilibrium parameter, $\theta = T_e/T_h$. This division is given by

$$\frac{\left.\frac{\partial h_e}{\partial T_e}\right]_\theta}{\left.\frac{\partial h_e}{\partial T_e}\right]_\theta + \left.\frac{\partial h_h}{\partial T_e}\right]_\theta} \frac{Dp}{Dt} + \frac{\left.\frac{\partial h_h}{\partial T_e}\right]_\theta}{\left.\frac{\partial h_e}{\partial T_e}\right]_\theta + \left.\frac{\partial h_h}{\partial T_e}\right]_\theta} \frac{Dp}{Dt} = \frac{Dp}{Dt} \tag{3.19}$$

where the partial derivatives are calculated using finite differences with θ held constant. The first term on the left hand side is attributed to the electron energy equation and the second term on the left hand side is attributed to the heavy species energy equation. It is evident that this still satisfies the requirement that the sum of the electron and heavy species pressure terms must equal the total pressure term.

The two methods of breaking up the pressure term are shown in figure 3.1. It can be seen that they are not the same. In practice, however, the two methods give a minimal difference in the results. Thus, to maintain consistency with the literature, the method of partial pressures is used. It should be noted, however, that these two methods may give different results in different applications.

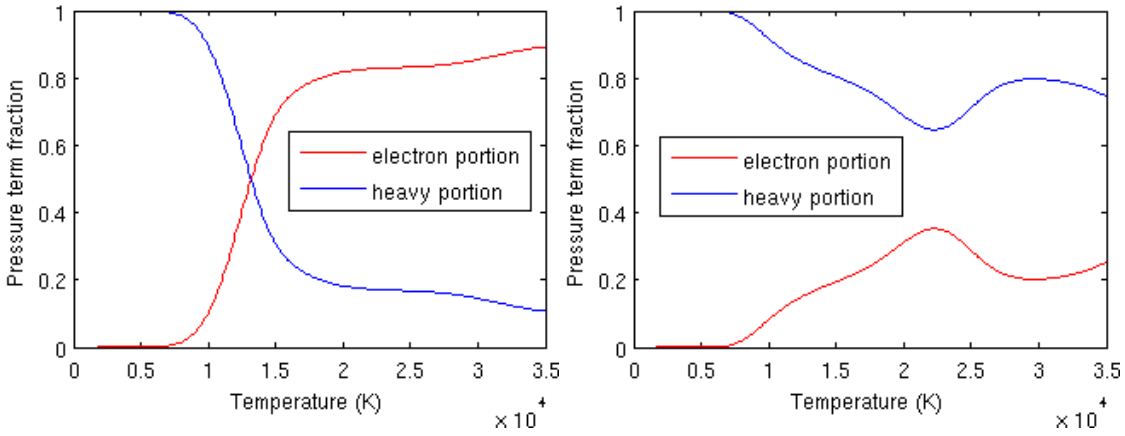

Figure 3.1. The fraction of the pressure term applied to the electron and heavy species energy equations. The division is given by equations 3.16-3.17 on the left and equation 3.19 on the right.

3.3.3. Energy exchange between electrons and heavy species

The final term on the right hand side of equations 3.4 and 3.5 describes the flow of energy between the electrons and heavy species. This term is given as [11]

$$\dot{Q}_{eh} = \sum_{s \neq e} 3k_b \frac{m_e}{m_i} n_e \nu_{ei} (T_e - T_h) \delta_{ei} \tag{3.20}$$

where m_i is the mass of a particle of species i, m_e is the electron mass density, ν_{ei} is the collision frequency, and δ_{ei} is the inelastic collision factor. In essence, this term calculates the energy transferred between electrons and heavy species if all collisions are elastic and then multiplies by the inelastic collision factor to account for inelastic effects. For the monatomic species, nearly all collisions are elastic and the inelastic collision factor is approximately one. For the diatomic species, however, the collisions are generally inelastic because a large portion of energy is transferred to the molecules in the form of vibrational and rotation energy. Thus, the inelastic collision factor is much larger for molecules than for monatomic species. The question of what this factor should be will be discussed in detail in section 7.5.

3.3.4. Choice of enthalpy or temperature in the energy equations

The energy equations present a unique problem that will be addressed here. For simplicity, the inclusion of iron vapors will be neglected until the end of the section. This problem is that both enthalpy and temperature appear in the energy equations. In order to solve these equations with CFD techniques, however, it is necessary to express them as functions of only one independent variable. For the LTE case, this is fairly straight forward because the relationship between enthalpy and temperature is given in the specific heat.

$$c_p = \frac{dh}{dT} \tag{3.21}$$

Using the specific heat, the energy equation can be written in terms of temperature as

$$c_p \frac{\partial \rho T}{\partial t} + c_p \nabla \cdot \rho \vec{u} T = \nabla \cdot \kappa \nabla T + \frac{Dp}{Dt} + \frac{5}{2}\frac{k_b}{e}(\vec{j} \cdot \nabla T) + \vec{j} \cdot \vec{E} - \dot{Q}_r \tag{3.22}$$

and the enthalpy can be easily found because it is tabulated as a function of T and p as described in chapter 4. Alternatively, the energy equation can be written in terms of enthalpy as

$$\frac{\partial \rho h}{\partial t} + \nabla \cdot \rho \vec{u} h = \nabla \cdot \frac{\kappa}{c_p} \nabla h + \frac{Dp}{Dt} + \frac{5}{2}\frac{k_b}{e}(\vec{j} \cdot \frac{1}{c_p} \nabla h) + \vec{j} \cdot \vec{E} - \dot{Q}_r \tag{3.23}$$

and the temperature can then be easily found using an inverted lookup from the tabulation of enthalpy, because the enthalpy is strictly monotonically increasing with temperature.

The two-temperature case is significantly more complicated because the concept of specific heat breaks down. With the introduction of a second temperature and a second enthalpy, it is necessary to specify what enthalpy is changing with respect to what temperature. Thus, we consider the full differential of the heavy species and electron enthalpies, which are functions of T_e, T_h, and p.

$$dh_h = \frac{\partial h_h}{\partial T_e} dT_e + \frac{\partial h_h}{\partial T_h} dT_h + \frac{\partial h_h}{\partial p} dp \tag{3.24}$$

$$dh_e = \frac{\partial h_e}{\partial T_e} dT_e + \frac{\partial h_e}{\partial T_h} dT_h + \frac{\partial h_e}{\partial p} dp \tag{3.25}$$

where six partial derivatives have now taken the place of the specific heat. Using these relationships, the two energy equations can be written in terms of temperature

$$\frac{\partial h_e}{\partial T_e}\left(\frac{\partial \rho T_e}{\partial t}+\nabla\cdot\rho\vec{u}T_e\right)+\frac{\partial h_e}{\partial T_h}\left(\frac{\partial \rho T_h}{\partial t}+\nabla\cdot\rho\vec{u}T_h\right)+\frac{\partial h_e}{\partial p}\left(\frac{\partial \rho p}{\partial t}+\nabla\cdot\rho\vec{u}p\right)$$
$$=\nabla\cdot q_e+\frac{Dp_e}{Dt}+\frac{5}{2}\frac{k_b}{e}(\vec{J}\cdot\nabla T_e)+\vec{j}\cdot\vec{E}-\dot{Q}_r-\dot{Q}_{eh} \tag{3.26}$$

$$\frac{\partial h_h}{\partial T_h}\left(\frac{\partial \rho T_h}{\partial t}+\nabla\cdot\rho\vec{u}T_h\right)+\frac{\partial h_h}{\partial T_e}\left(\frac{\partial \rho T_e}{\partial t}+\nabla\cdot\rho\vec{u}T_e\right)+\frac{\partial h_h}{\partial p}\left(\frac{\partial \rho p}{\partial t}+\nabla\cdot\rho\vec{u}p\right)$$
$$=\nabla\cdot q_h+\frac{Dp_h}{Dt}+\dot{Q}_{eh} \tag{3.27}$$

The heavy species and electron specific enthalpies can then be easily found because they will be tabulated as functions of T_e, T_h, and p as described in chapter 4. These equations could also be written in terms of electron and heavy species enthalpies. The task of finding the electron and heavy species temperatures as functions of the electron and heavy species enthalpies, however, is problematic, requiring a two step inverse lookup interpolation. This interpolation is found to be ill-conditioned, which is to say that a small error in the enthalpy results in a large error in temperature. Furthermore, the problem sometimes gives non-unique solutions, either due to algorithmic of physical problems. Thus, it is clear that the use of an enthalpy formulation for the two temperature equations is unfeasible.

While the enthalpy formulation of the two temperature equations is not viable, there is an alternative temperature formulation that is considered. Instead of using a differential to relate the enthalpy and temperature, they can be directly related using the definition of enthalpy given in chapter 4.

$$h_e=\frac{5}{2}\frac{n_e k_b T_e}{\rho} \tag{3.28}$$

$$h_h=\frac{5}{2}\frac{n_h k_b T_h}{\rho}+\sum_{i\neq e}\frac{n_i E_i}{\rho} \tag{3.29}$$

where n is the number density of particles and the subscripts h, e, and i refer respectively to all heavy species, electrons, and species i. The enthalpy of formation is represented by E_i. The component of enthalpy stored in internal modes of excitation is neglected because it adds significant complexity without much additional accuracy. Using these expressions, the two energy equations can be written as

$$\frac{\partial \frac{5}{2} n_e k_b T_e}{\partial t} + \nabla \cdot \vec{u} \frac{5}{2} n_e k_b T_e = \nabla \cdot q_e + \frac{Dp_e}{Dt} + \frac{5}{2} \frac{k_b}{e} (\vec{j} \cdot \nabla T_e) + \vec{j} \cdot \vec{E} - \dot{Q}_r - \dot{Q}_{eh} \tag{3.30}$$

$$\frac{\partial \frac{5}{2} n_h k_b T_h}{\partial t} + \nabla \cdot \vec{u} \frac{5}{2} n_h k_b T_h + \frac{\partial \sum_{i \neq e} \frac{n_i E_i}{\rho}}{\partial t} + \nabla \cdot \vec{u} \sum_{i \neq e} \frac{n_i E_i}{\rho} = \nabla \cdot q_h + \frac{Dp_h}{Dt} + \dot{Q}_{eh} \tag{3.31}$$

For the sake of clarity, the method used in equations 3.26 and 3.27 will be referred to as the differential method because it uses differentials to write enthalpy in terms of temperature and the method used in equations 3.30 and 3.31 will be referred to as the definition method because it uses the definition of enthalpy to write enthalpy in terms of temperature. The differential and definition methods are not mutually exclusive and different methods could be used for each equation or even each term within the equations. When the numerical schemes are discussed in chapter 5, it will become apparent that the definition method lacks numerical stability. Thus, the present work uses the temperature formulation of the energy equations with the differential method. While either the enthalpy or temperature formulation could be used in the LTE case, the temperature formulation will be used for consistency.

When iron vapor is included, the enthalpies then are a function of the mole fraction of iron as well. Equations 3.24 and 3.25 then take the form

$$dh_h = \frac{\partial h_h}{\partial T_e} dT_e + \frac{\partial h_h}{\partial T_h} dT_h + \frac{\partial h_h}{\partial p} dp + \frac{\partial h_h}{\partial x} dx \tag{3.32}$$

$$dh_e = \frac{\partial h_e}{\partial T_e} dT_e + \frac{\partial h_e}{\partial T_h} dT_h + \frac{\partial h_e}{\partial p} dp + \frac{\partial h_e}{\partial x} dx \tag{3.33}$$

It is evident how the energy equations are formulated with an additional partial derivative. The LTE energy equation is treated similarly, where the differential is

$$dh = \frac{\partial h}{\partial T} dT + \frac{\partial h}{\partial p} dp + \frac{\partial h}{\partial x} dx \tag{3.34}$$

and extra terms are added to the LTE energy equation for pressure and mole fraction of iron.

3.3.5 Radiation

Due to the high temperatures present in plasma arc cutting, the radiation effects of the plasma gas are very significant and must be included in the model. There are two main goals for a radiation model. The first of these is to find the correct energy loss from the plasma due to

radiation emission. In other words, the first goal is to find the correct value of $\dot{Q}_r$ in the energy equations. The second goal is to find the radiative heat flux throughout the domain, which ultimately gives the radiative heat flux to the work piece.

The radiation is governed by the radiative transfer equation [52]

$$\frac{\partial I_\eta}{\partial s} = k_\eta I_{b\eta} - k_\eta I_\eta - \sigma_{s\eta} I_\eta + \frac{\sigma_{s\eta}}{4\pi} \int_{4\pi} I_\eta \Phi_\eta(\hat{s}_i, \hat{s}) \mathrm{d}\Omega_i \tag{3.35}$$

where I_η is the radiative intensity, which is a function of direction, position, and wavelength, η. The radiative transfer equation states that the change in the radiative intensity in the direction s is equal to the radiation emmitted minus the radiation absorbed minus the radiation scattered out of the direction plus the radiation scattered into the direction. Scattering effects will be minimal in a thermal plasma, so the radiative transfer equation simplifies to

$$\frac{\partial I_\eta}{\partial s} = k_\eta I_{b\eta} - k_\eta I_\eta \tag{3.36}$$

which includes only the emission and absorption terms on the right hand side. The variable $I_{b\eta}$ is the black body intensity, which is a function of temperature and wavelength. The variable k_η is the absorption coefficient, which is a property of the plasma gas and is a function of temperature and wavelength.

The radiation heat flux can be found from the radiative intensity as [52]

$$\vec{q}_r = \int_0^\infty \int_{4\pi} I_\eta(\hat{s}) \hat{s} d\Omega d\eta \tag{3.37}$$

here Ω is all solid angles. In effect, this integrates over the radiative intensity of any wavelength coming from any direction. The radiative energy lost from a given control volume is then simply the divergence of this heat flux.

$$\dot{Q}_r = \nabla \cdot \vec{q}_r \tag{3.38}$$

The net emission coefficient model, developed by Lowke [53] in 1974, has become the most popular method of including radiation in thermal plasma models. In this model, each control volume is assumed to be surrounded by a sphere of plasma at the same temperature as the volume. The radius of this sphere is assumed to have some effective radius, R_{eff}, which is approximately the radius of the plasma arc. Radiation is emitted from the chosen control volume and then some of it is reabsorbed by the surrounding sphere. All radiation that escapes the sphere

is assumed to be lost to the ambient. The net emission coefficient is then defined as the radiation emitted in a particular solid angle from the control volume minus any radiation absorbed in the surrounding sphere. Because of the simple spherical geometry and the assumption of constant temperature, this problem can be solved in closed form to give [54].

$$\varepsilon = \int_0^\infty I_{b\eta} k_\eta \exp\left(-R_{eff}\kappa_\eta\right) d\eta \tag{3.39}$$

It is evident from this expression that the net emission coefficient is dependent only on temperature and effective radius. The total energy emitted from the control volume can be found by integrating over all solid angles, and thus, the radiation source term appearing in the energy equations is given as

$$\dot{Q}_r = 4\pi\varepsilon \tag{3.40}$$

The net emission coefficient for pure oxygen is given in [54] and for pure iron is given in [55] for various effective radii. This is plotted in figure 3.2. For a combination of oxygen and iron, the net emission coefficient is assumed to be a simple interpolation between the two gases, weighted by the mole fraction. [22]

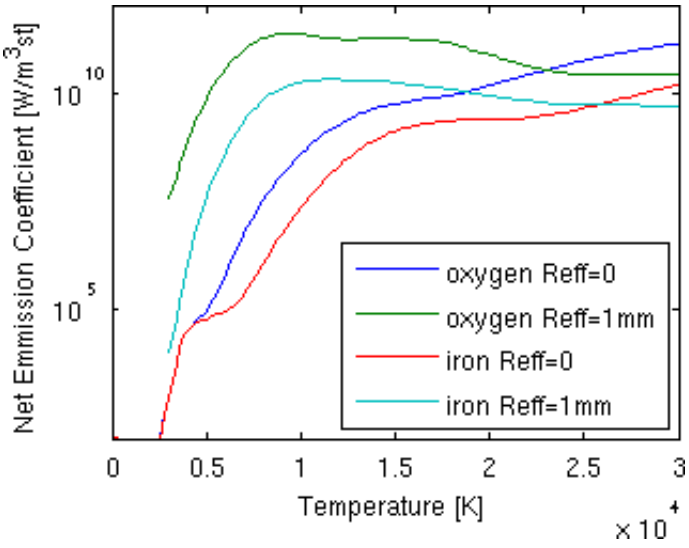

Figure 3.2. Net emission coefficients of oxygen and iron for effective radius of 0 and 1mm.

The major shortcoming of the net emission coefficient is that it does not calculate the heat flux throughout the domain. Thus, the radiation heat transfer to the work piece cannot be calculated. In order to do that, a more complicated radiation model must be used. For the present work, however, it is deemed sufficient to calculate the correct temperature distribution throughout

the plasma. In calculating the heat flux to the work piece, it is noted that there is some additional heat transfer to the work piece due to radiation.

Chapter 4

Thermodynamic and Transport Property Calculations

Obtaining thermodynamic and transport properties is one of the largest challenges present in the modeling of a thermal plasma. Because of the extremely high temperatures present, it is entirely unfeasible to obtain these properties experimentally. Rather, these properties must be calculated using theory developed from statistical mechanics and gas kinetics. The path to calculating the thermodynamic and transport properties is as follows: 1) The equilibrium chemical composition of the plasma is first calculated using mass action laws developed from statistical mechanics. 2) The thermodynamic properties are then calculated based on the chemical composition using equations also developed from statistical mechanics. 3) Finally, the transport properties are calculated using the Chapman-Enskog method, which is based on gas kinetics and an understanding of the collisions between particles. This chapter will detail how each of these three steps were accomplished in the present work.

4.1. Composition

The calculation of the plasma composition first requires a choice of species to be included. In this work, the following species are included: O_2, O_2^+, O, O^+, O^{++}, Fe, Fe^+, Fe^{++}, Fe^{+++}, and electrons. Of particular note, the O_2^+ species has been neglected in all published two-temperature oxygen calculations. It will be shown later that O_2^+ is vital to the stability and accuracy of the model. Also of particular note, the species FeO has been neglected. This species will be present only at low temperatures and will likely have little effect on the transport and

thermodynamic properties. Furthermore, the inclusion of the FeO species would severely complicate the problem of diffusion between iron vapors and oxygen, as will be explained later.

Assuming chemical equilibrium and minimizing Gibb's free energy produces a mass action law [56]. Using the ionization of an oxygen atom as an example, this takes the form

$$\frac{N_e N_{O+}}{N_O} = \frac{Q^e Q^{O^+}}{Q^O} \exp\left(\frac{-E_{ionization}}{k_b T}\right) \tag{4.1}$$

where N denotes the number of the given species in a given volume V, $E_{ionization}$ is the ionization energy of atomic oxygen, k_b is the Boltzmann constant, and T is the temperature. The variable Q denotes the partition function of the given species, which can be written as the product of the translational partition function and the internal partition function. The translational partition function is given by

$$Q_{tr}^i = V\left(\frac{2\pi m_i k_b T}{h^2}\right)^{3/2} \tag{4.2}$$

where V is the volume containing the particles in equation 4.1, m_i is the mass of a particle of species i, and h is the Planck constant. It is customary to divide both sides of equation 4.1 by V so that the left hand side is expressed in number densities and then volume drops out of the partition functions on the right hand side. Following this convention, it is understood hereafter that V is left out of the translational partition function and the left hand side is written in terms of number densities, denoted by a lower case n. The internal partition function can be written as the product of vibrational, rotational, and electronic partition functions, where the vibrational and rotational components do not appear for monatomic species. The electronic partition function of monatomic species is then given as

$$Q_{el}^i = \sum_j g_j exp\left(\frac{-e_j}{k_b T}\right) \tag{4.3}$$

where e_j are the energies of the electronic excitation states and g_j are the corresponding degeneracies. The energy states are generally written such that the ground state of the species has an energy of zero. Each species, however, has a different ground state. Thus, in order to write all electronic partition functions with respect to a single ground state, the electronic partition function becomes

$$Q_{el}^{i} = \sum_{j} g_j exp\left(\frac{-(E_i + e_j)}{k_b T}\right) = \exp\left(\frac{-E_i}{k_b T}\right) \sum_{j} g_j exp\left(\frac{-e_j}{k_b T}\right) \tag{4.4}$$

where E_i is the enthalpy of formation of the species. This enthalpy of formation appears in equation 4.1 in the final exponential term where

$$E_{ionization} = -E_e - E_{O+} + E_O \tag{4.5}$$

This suggests a fictional "reactive partition function" Q_r, such that

$$Q_r^i = \exp\left(\frac{-E_i}{k_b T}\right) \tag{4.6}$$

This is not a true partition function by definition, but it is a useful construct employed to simplify the form of the mass action law. Equation 4.1 then takes the form

$$\frac{n_e n_{O^+}}{n_O} = \frac{Q_{tr}^e Q_{tr}^{O^+}}{Q_{tr}^O} \frac{Q_{int}^e Q_{int}^{O^+}}{Q_{int}^O} \frac{Q_r^e Q_r^{O^+}}{Q_r^O} = \frac{Q^e Q^{O^+}}{Q^O} \tag{4.7}$$

Considering all ten chosen species, there are seven such mass action laws:

$$\frac{n_e n_{O^+}}{n_O} = \frac{Q^e Q^{O^+}}{Q^O} \tag{4.8.a}$$

$$\frac{n_e n_{O^{++}}}{n_{O^+}} = \frac{Q^e Q^{O^{++}}}{Q^{O^{++}}} \tag{4.8.b}$$

$$\frac{n_e n_{O_2^+}}{n_{O_2}} = \frac{Q^e Q^{O_2^+}}{Q^{O_2}} \tag{4.8.c}$$

$$\frac{n_O n_O}{n_{O_2}} = \frac{Q^O Q^O}{Q^{O_2}} \tag{4.8.d}$$

$$\frac{n_e n_{Fe^+}}{n_{Fe}} = \frac{Q^e Q^{Fe^+}}{Q^{Fe}} \tag{4.8.e}$$

$$\frac{n_e n_{Fe^{++}}}{n_{Fe^+}} = \frac{Q^e Q^{Fe^{++}}}{Q^{Fe^+}} \tag{4.8.f}$$

$$\frac{n_e n_{Fe^{+++}}}{n_{Fe^{++}}} = \frac{Q^e Q^{Fe^{+++}}}{Q^{Fe^{++}}} \tag{4.8.g}$$

Furthermore, Dalton's law gives

$$p = \sum_{i=1}^{10} n_i k_b T \tag{4.9}$$

where p is the pressure. The assumption of quasi-neutrality gives

$$n_e = n_{O^+} + 2n_{O^{++}} + n_{O_2^+} + n_{Fe^+} + 2n_{Fe^{++}} + 3n_{Fe^{+++}} \tag{4.10}$$

and for a specified mole fraction of iron vapor

$$\begin{aligned} &\frac{1}{1-\overline{x_{Fe}}}\left(n_O + n_{O_2} + 2n_{O_2^+} + 2n_{O^+} + 3n_{O^{++}}\right) \\ &\qquad = \frac{1}{\overline{x_{Fe}}}\left(n_{Fe} + 2n_{Fe^+} + 3n_{Fe^{++}} + 4n_{Fe^{+++}}\right) \end{aligned} \tag{4.11}$$

where $\overline{x_{Fe}}$ is the mole fraction of iron vapor, which includes all of the iron species plus the requisite number of electrons to keep the iron vapor quasi-neutral.

Thus, it is seen that the chemical composition is described as a function of T, p, and $\overline{x_{Fe}}$ by ten equations with ten unknown number densities. Godin et al. [57] have presented an elegant and robust solution algorithm for this problem formulation, which is implemented for this work.

Once these equations have been formulated and the solution algorithm implemented, the only remaining difficulty is to calculate the correct partition functions. The translational partition functions for all species are easily calculated using equation 4.2. The internal partition function for electrons is simply 2 [56]. The internal partition functions of the monatomic species are calculate using equation 4.3 where the values of e_j and g_j are found in the NIST database [58]. The internal partition function of the diatomic oxygen species are more complicated and are calculated according to the method presented in [59]. The fictional reactive partition function depends on the enthalpy of formation of a species measured relative to some arbitrary zero value. Because it is assumed that the iron and oxygen gases do not chemically react with each other, they each have their own arbitrary zero from which the enthalpy of formation is measured. For this work, it is assumed that the species Fe and O have a zero enthalpy of formation. Furthermore, the electrons are assumed to have zero enthalpy of formation, which is consistent with the assumption that all reaction energy is stored with the heavy species. Following these assumptions, the enthalpy of formation for each species is given in table 4.1. For the monatomic ions, this is simply the energy required to ionize an atom to the given degree. For O_2, this is half the energy needed to dissociate the molecule and is negative because the ground state of O_2 is

lower than O. For O_2^+, this is the dissociation energy appearing for O_2 plus the energy needed to ionize the molecule.

Table 4.1. Enthalpy of formation for each specie

Specie	E_i(ev)	Reference
O_2	-5.12	[56]
O_2^+	6.95	[56, 60]
O	0.000	Assumed
O^+	13.618	[58]
O^{++}	48.739	[58]
Fe	0.000	Assumed
Fe^+	7.902	[58]
Fe^{++}	24.090	[58]
Fe^{+++}	54.741	[58]

The results under the LTE assumption are shown for pure oxygen and for 10% iron in figures 4.1 and 4.2. The results of pure oxygen are compared with those of Colombo et al. [61] and agreement is found. Note that the O_2^+ ion is negligable under the LTE assumption, which is probably the reason that it has been widely neglected. While the composition of the oxygen and iron mixture is more complicated because of the additional species present, the most important aspect to note is that the first ionization reaction and thus the appearance of electrons happens at a lower temperature. In pure oxygen, there is a negligible number of electrons below ~5000K, whereas the presence of iron vapor decreases this negligible electron cutoff to ~3000K. It will be noted later that this has a significant and important effect on the electrical conductivity.

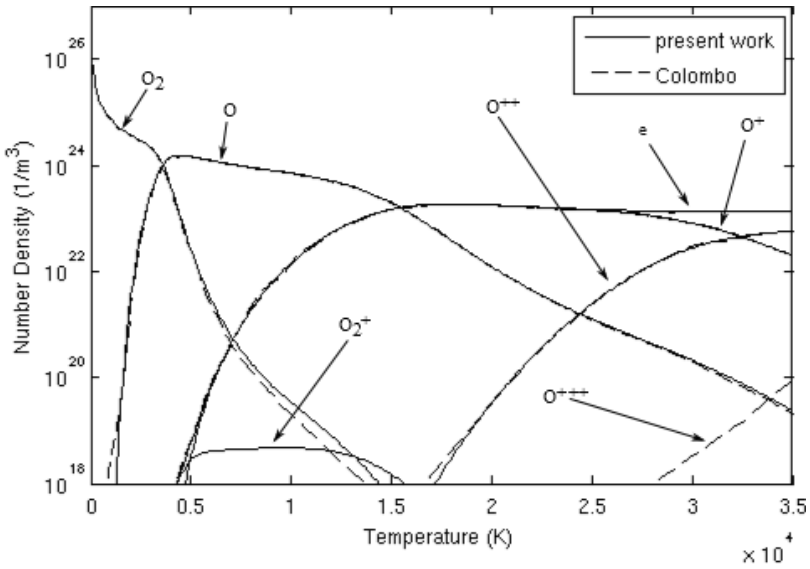

Figure 4.1. The chemical composition of a pure oxygen plasma compared with [61]

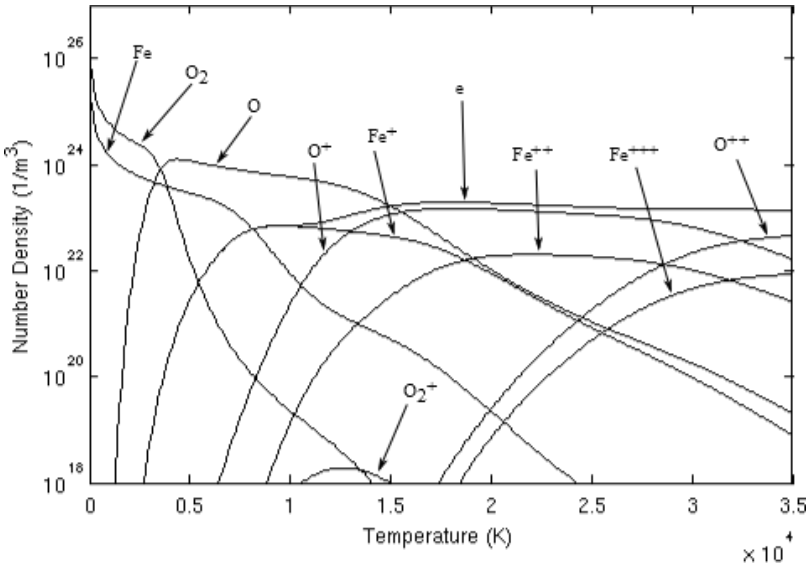

Figure 4.2. The chemical composition of an oxygen plasma containing 10% iron vapor by mole fraction.

When expanding to the two temperature formulation, the composition is a function of four variables: T_e, T_h, p, and $\overline{x_{Fe}}$. Furthermore, it is necessary to consider carefully which temperature belongs in each partition function. Because the electron temperature describes the kinetic energy of the electrons, it is evident that the translational partition function of the electrons uses the electron temperature. Similarly, because the heavy species temperature

describes the kinetic energy of the heavy species, it is evident that the translational partition functions of the heavy species uses the heavy species temperature. It is assumed here that the electronic excitation is best described by the electron temperature, while vibrational and rotational excitation are best described by the heavy species temperature [62]. Thus, the electron temperature is used in the internal partition functions of the monatomic species. A combination of the two temperatures is used in the internal partition function of the diatomic species because both vibrational and rotational excitation are present along with electronic excitation.

The reactive partition functions require particular attention in the two temperature formulation. Ionizing reactions occur when electrons are excited to such a level that they detach from the parent atom. Thus, ionizing reactions will depend on the electronic excitation which depends on the electron temperature. Dissociating reactions, on the other hand, occur when a vibrational mode is excited to such a level that the two atoms tear apart. Thus, the dissociating reactions will depend on the vibrational excitation, which depends on the heavy species temperature. Because of the convenient choice of O and Fe as base species, the reactive partition function for all monatomic ions is a function of T_e, while the reactional partition function for the O_2 molecule is a function of T_h. The reactive partition function of the O_2^+ ion is more complicated and includes both T_e and T_h as given by

$$Q_r^{O_2^+} = \exp\left(\frac{-E_{ionize}}{k_b Te} + \frac{-E_{dissociate}}{k_b Th}\right) \tag{4.12}$$

where $E_{ionize} = 12.070$ is the portion of the enthalpy of formation due to the ionization and $E_{dissociate} = -5.12$ is the portion of the enthalpy of formation due to the combination of oxygen atoms. Furthermore, Dalton's law takes the form

$$p = n_e k_b T_e + \sum_{i \neq e} n_i k_b T_h \tag{4.13}$$

The chemical composition in the case of a two temperature model with a non-equilibrium parameter of $\theta = T_e/T_h = 3$ is shown in figures 4.3 and 4.4. Because the dissociation reaction is most dependent on the heavy species temperature, it is pushed to a higher electron temperature. In the case where the O_2^+ ion is neglected, ionization is not able to occur until this dissociation reaction occurs. Thus, the electron number density remains negligible until this dissociating reaction at ~6000K. This is evident in the results of Colombo et al. [61], which neglects the O_2^+ ion. In the present work, which includes the O_2^+ ion, the molecules are able to ionize before the dissociation reaction, so the electron number density becomes significant at a lower electron

temperature of ~4000K. The electrical conductivity and thus the behavior of the model is heavily dependent on the electron number density, and thus, the inclusion of the O_2^+ ion is vital for an accurate model. As with the LTE results, the inclusion of 10% iron vapors moves the appearance of electrons to an even lower temperature of ~3000K.

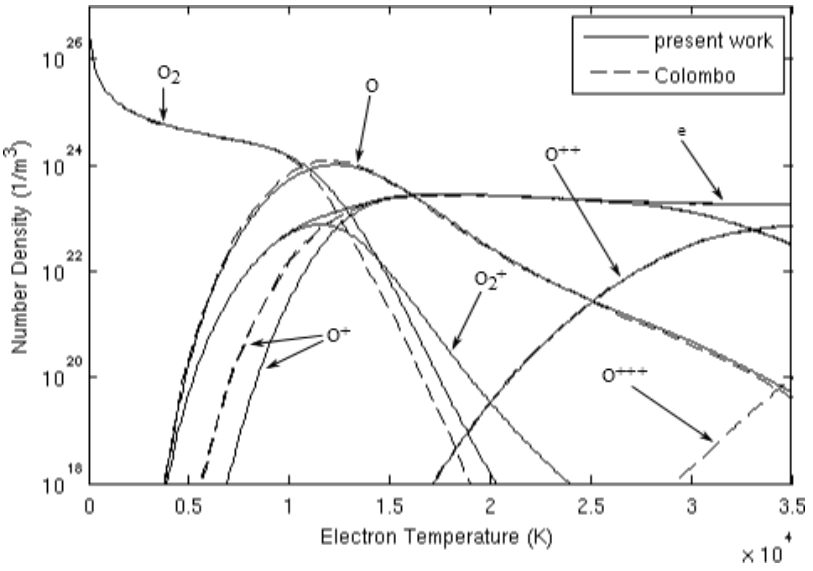

Figure 4.3. The chemical composition of a two-temperature oxygen plasma for $\theta = 3$ compared with [61].

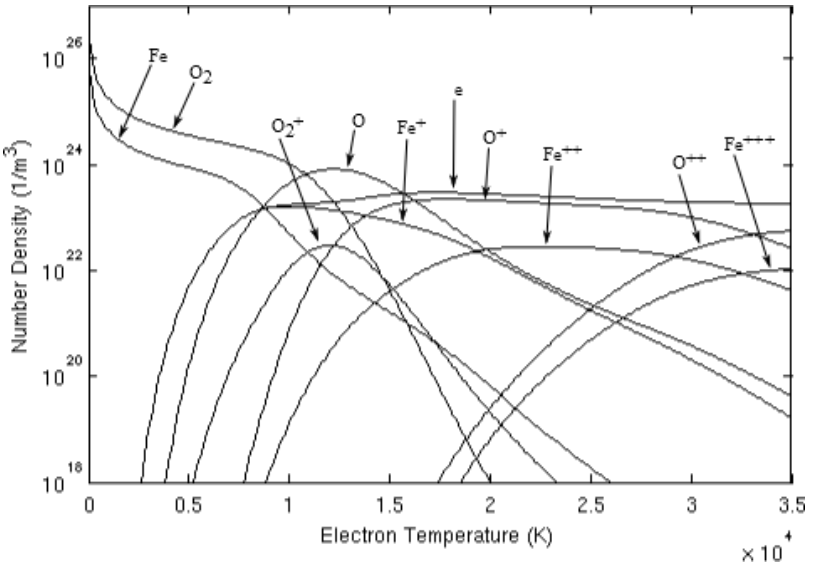

Figure 4.4. The chemical composition of two-temperature oxygen plasma containing 10% iron vapor by mole fraction for $\theta = 3$.

4.2. Thermodynamics

Once the composition has been calculated, giving the number density of each species, the thermodynamic properties can be calculated in a relatively straight forward manner. The mass density is found by summing over the number density of each species times the mass of that species.

$$\rho = \sum_i n_i m_i \tag{4.14}$$

The specific energy of the plasma is best understood by breaking it into components: translational energy of heavy species, translational energy of electrons, energy due to internal modes of excitation, and reactive energy.

$$e_{tot} = e_{htr} + e_{etr} + e_{int} + e_{react} \tag{4.15}$$

Considering first the translation energy, we write the energy of a single particle determined from statistical mechanics [56].

$$\tilde{e} = \frac{3}{2} k_b T \tag{4.16}$$

Multiplying by the number density of each species and summing over all species gives the energy per volume, which is then divided by the density to give the specific energy as energy per mass. As in the calculation of composition, the translational energy of the heavy species is dependent on the heavy species temperature and the translational energy of the electrons is dependent on the electron temperature.

$$e_{tr} = \frac{3}{2}\frac{n_e k_b T_e}{\rho} + \sum_{i \neq e} \frac{3}{2}\frac{n_i k_b T_h}{\rho} \tag{4.17}$$

From this expression, the distinction between electron and heavy species translational energy is easy to make. The first term gives the specific translational energy of electrons and the second term gives the specific translation energy of heavy species. To prevent ambiguity, it is noted here that the term "specific energy of electrons" is defined as the electron energy per mass of gas (not to be confused with the electron energy per mass of electrons, which is neither calculated nor used in this work.)

The energy of a single particle due to internal modes of excitation is also found from statistical mechanics using the internal partition function. [56]

$$\tilde{e}_{int} = k_b T^2 \frac{\partial[\ln(Q_{int})]}{\partial T} \tag{4.18}$$

As with the translational energy, the specific internal energy is then found by multiplying by number density, summing over all species, and dividing by mass density. For electrons, this energy is simply zero because the internal partition function of electrons is simply two. For the monatomic species, the internal partition function is purely due to electron excitation, which is dependent on the electron temperature. Thus, the electron temperature is used in the calculation of the internal energy. For the diatomic species, however, the internal partition function also includes vibrational and rotational excitation modes, which are dependent on the heavy species temperature. Because the amount of energy stored in these vibrational and rotational modes is far greater than the energy stored in electron excitation, the heavy species temperature is used in the calculation of the internal energy for the diatomic species. Thus, the full expression for specific energy due to internal excitation modes is

$$e_{int} = \sum_{i=monatomic} \left(\frac{n_i k_b {T_e}^2}{\rho} \frac{\partial \ln\left(Q_{int}^i\right)}{\partial T_e} \right) + \sum_{i=diatomic} \left(\frac{n_i k_b {T_h}^2}{\rho} \frac{\partial \ln\left(Q_{int}^i\right)}{\partial T_h} \right) \tag{4.19}$$

where the derivatives are calculated using the finite difference method.

Finally, the reactive energy accounts for the energy used in ionizing and dissociating reactions. This energy is the same as the enthalpy of formation listed in table 4.1. Thus, specific reactive energy is given as

$$e_{react} = \sum_{i \neq e} \frac{n_i E_i}{\rho} \tag{4.20}$$

The final form of the total specific energy is given as the sum of all these terms. For the purpose of formulating governing equations, however, it is more convenient to work with specific enthalpy rather than specific energy. Specific enthalpy is defined as $h = e + pv$. Using the ideal gas law, this is written as $h = e + \frac{nk_bT}{\rho}$. The specific enthalpy is broken up into the same components as specific energy and the extra term is absorbed into the translational component. Thus, the specific enthalpy is written as

$$h_{tot} = h_{htr} + h_{etr} + h_{int} + h_{react} \tag{4.21}$$

where

$$h_{etr} = \frac{5}{2}\frac{n_e k_b T_e}{\rho} \tag{4.22}$$

$$h_{htr} = \sum_{i \neq e} \frac{5}{2}\frac{n_i k_b T_h}{\rho} \tag{4.23}$$

$$h_{int} = e_{int} \tag{4.24}$$

$$h_{react} = e_{react} \tag{4.25}$$

For the purpose of two temperature modeling, it is necessary to break the total enthalpy into electron and heavy species enthalpies. Clearly, the electron translational enthalpy belongs with the electron enthalpy and the heavy species translational enthalpy belongs with the heavy species enthalpy. The specific enthalpy due to internal excitation modes belongs with the heavy species enthalpy because this term is simply zero for the electrons. The reactive enthalpy is associated with both heavy species and electrons because both are involved in the ionization reaction. For ease of bookkeeping, however, this term must be assigned to one or the other and not both. In this work, the reactive energy is stored with the heavy species because it is possible to have a non-zero reactive energy due to dissociation without having any electrons present. This is the reason in section 3.1 for assuming all reactive energy is stored with heavy species. Thus, to summarize, the electron and heavy species enthalpies are written as

$$\begin{aligned} h_h = \sum_{i \neq e} \frac{5}{2}\frac{n_i k_b T_h}{\rho} + \sum_{i=monatomic} \left(\frac{n_i k_b {T_e}^2}{\rho} \frac{\partial \ln\left(Q_{int}^i\right)}{\partial T_e} \right) \\ + \sum_{i=diatomic} \left(\frac{n_i k_b {T_h}^2}{\rho} \frac{\partial \ln\left(Q_{int}^i\right)}{\partial T_h} \right) + \sum_{i \neq e} \frac{n_i E_i}{\rho} \end{aligned} \tag{4.26}$$

$$h_e = \frac{5}{2}\frac{n_e k_b T_e}{\rho} \tag{4.27}$$

The single, LTE specific enthalpy is easily obtained by setting $T_e = T_h = T$ and noting that the total enthalpy is simply $h = h_e + h_h$. The total enthalpy, as well as the electron and heavy species components under the LTE assumption, are plotted in figure 4.5. Reasonable agreement is found when comparing to the work of Ghorui et al. [62] and Colombo et al. [61]. For consistency, it is important to note that the electron and heavy species enthalpies sum up to the total enthalpy.

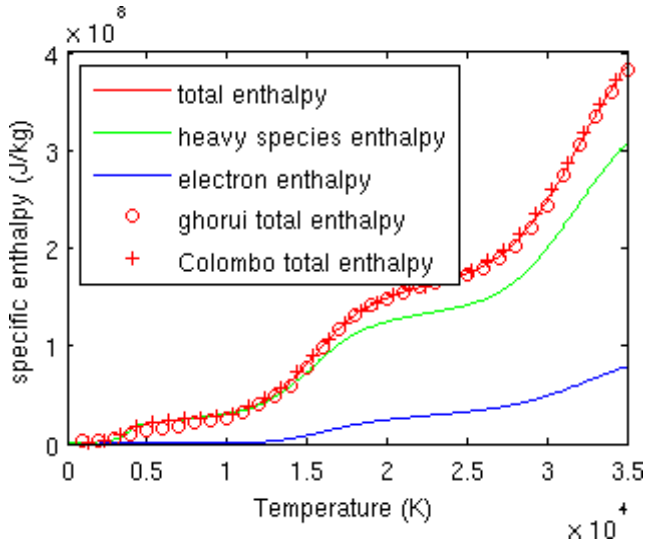

Figure 4.5. Specific enthalpy of an oxygen plasma, compared with literature [36, 61].

For an LTE formulation, where $T_e = T_h = T$, the specific heat is simply the change in enthalpy per change in temperature, which can be easily calculated using the finite difference method.

$$c_p = \frac{dh}{dT} \tag{4.28}$$

This is plotted in figures 4.6 and 4.7 where reasonable agreement is found with values reported in literature.

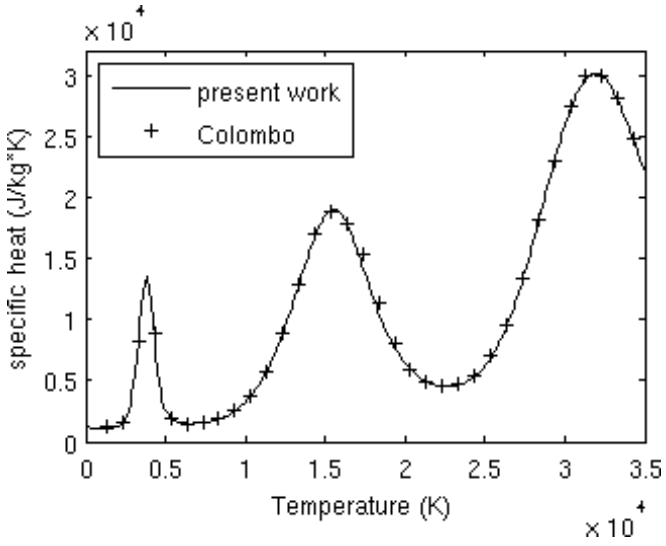

Figure 4.6. Specific heat of an oxygen plasma, compared to the results reported by Colombo et al. [61].

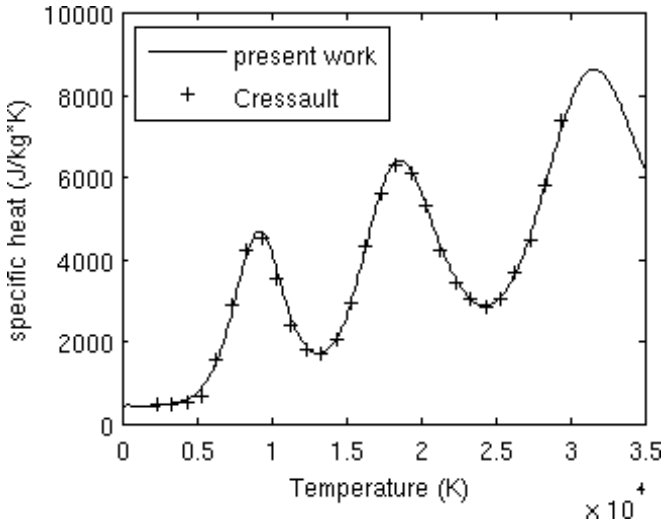

Figure 4.7. Specific heat of a pure iron plasma, compared to the results reported by Cressault et al. [63].

In the two temperature formulation, the concept of "specific heat" loses meaning because one must be more clear about which enthalpy is changing with which temperature. Colombo et al. [61] defines a total specific heat for a two-temperature plasma as the change in total enthalpy with electron temperature, although it is unclear if the heavy species temperature or the factor θ is held constant in this definition. Ghorui et al. [62] reports both a heavy species specific heat and an electron specific heat, but does not state which temperatures and enthalpies are used in the definition of these variables. In this work, the term "specific heat" will be abandoned and it will be noted instead that both the heavy species and electron enthalpy are functions of electron temperature, heavy species temperature, pressure, and, when iron vapors are included, the mole fraction. Thus, following the development in section 3.3.4 the differentials of the enthalpies are written as

$$dh_h(T_e, T_h, p, \overline{x_{Fe}}) = \frac{\partial h_h}{\partial T_e} dTe + \frac{\partial h_h}{\partial T_h} dT_h + \frac{\partial h_h}{\partial p} dp + \frac{\partial h_h}{\partial \overline{x_{Fe}}} d\overline{x_{Fe}} \tag{4.29}$$

$$dh_e(T_e, T_h, p, \overline{x_{Fe}}) = \frac{\partial h_e}{\partial T_e} dTe + \frac{\partial h_e}{\partial T_h} dT_h + \frac{\partial h_e}{\partial p} dp + \frac{\partial h_e}{\partial \overline{x_{Fe}}} d\overline{x_{Fe}} \tag{4.30}$$

It is evident that the specific heat is replaced by eight separate partial derivatives in the two temperature formulation. In the case of pure oxygen, this simplifies to six partial derivatives,

which are plotted in figure 4.8. It is apparent that they are similar to the specific heat, having strong peaks at reaction temperatures. Figure 4.9 shows the eight partial derivatives as a function of temperature for 10% iron vapor. It is observed that the addition of only a small amount of iron does little to change the shape of these curves but reduces the magnitude of the variables.

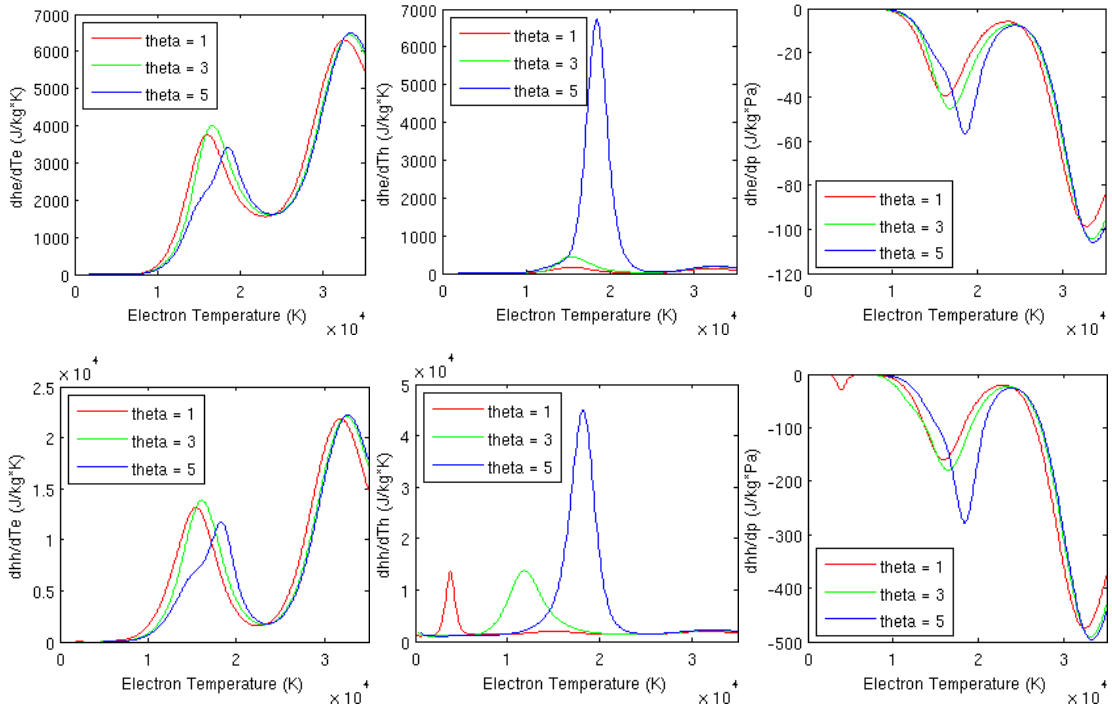

Figure 4.8. Partial derivatives of oxygen enthalpies appearing in equations 4.29 and 4.30.

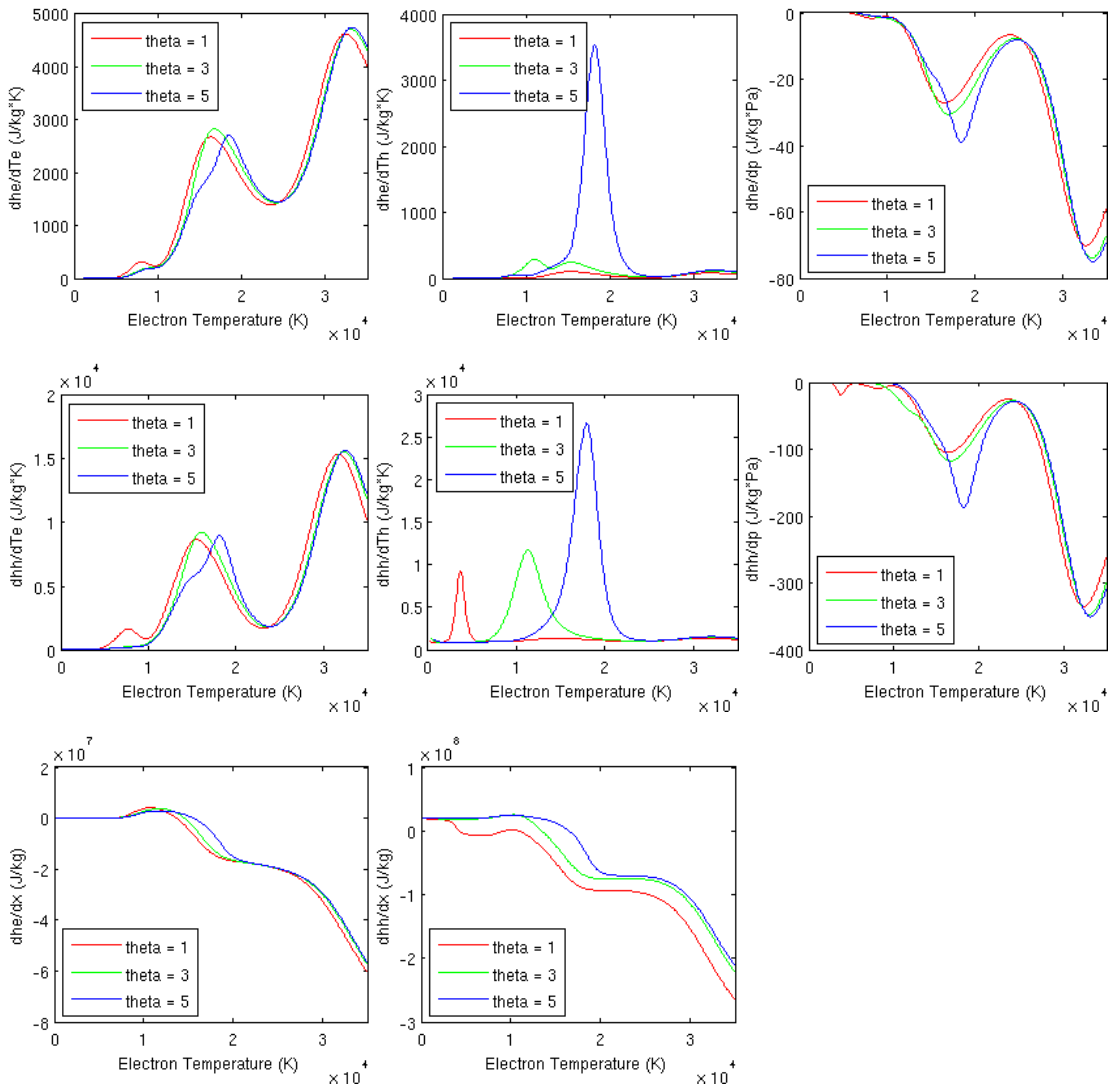

Figure 4.9. Partial derivatives of oxygen with 10% iron appearing in equations 4.29 and 4.30.

4.3. Transport Properties

Before describing the calculation of the transport properties used in the present work, it is worth first considering an overview of the state of transport property research. Once the overall state of transport property research is understood, the approach of the present work can be placed within that context. With the approach clarified, the actual calculations will then be described.

The mathematical development of the Chapman-Enskog method was laid out in the seminal work by Chapman and Cowling in 1932 [64]. All, or nearly all, plasma transport property calculations are based on this method. This method was further developed in the expansive work by Hirshfelder et al. in 1954 [65]. Finally in the late sixties, a series of papers were published by

Devoto [4-6] which expanded the Chapman-Enskog method to an ionized gas, using argon as an example. These papers laid out the calculations in a very clear and replicable manner, making it the standard for all LTE plasma transport property calculations. Since then, no real improvement to the equations used for LTE properties have been made. Expansions of the Devoto methods to a two-temperature formulation have been made, the most commonly cited being the thesis of Bonnefoi [66]. Unfortunately, that thesis is in French, making it inaccessible to many. The equations derived, however, can be found in a paper by Aubreton et al. [67]. In the early 2000's, a series of papers were published by Rat et al. [68-71] arguing that the methods of Devoto, expanded by Bonnefoi, are inadequate for a two-temperature formulation. Rat et al. then bypassed the work of Devoto, rederiving the calculation of the transport properties based on the Chapman-Enskog method. This work is significantly more complicated and more difficult to implement that the methods of Devoto. In 2008, a paper by Colombo et al. [61] implemented both the methods of Devoto and the methods of Rat et al. for a two-temperature formulation and found only minor differences in the results, casting doubt on the necessity of the more complicated Rat et al. method. Thus, Devoto's methods remain the standard for LTE calculations whereas there is no definitive consensus on the best method for two-temperature calculations.

All variations of the Chapman-Enskog method require collision integrals, which quantify the interactions between various species. The difficulty of obtaining these collision integrals rivals that of deriving the equations used for calculating transport properties. The collision integrals are generally found from experiment, theoretical calculations, or a combination thereof. Throughout this field of study, there are numerous possible assumptions used and almost an unlimited amount of research and refinement that could be undertaken. As such, there is often no clear consensus on how a particular collision integral should be obtained. Fortunately, however, large errors in the collision integrals generally have relatively minor effects on the final transport properties, which are the values of real interest.

While it is apparent that there is much work that still needs to be done in the field of transport property calculations, the focus of the present work is on producing a complete model that reasonably describes plasma arc cutting. Thus, only a portion of the present work can be dedicated to the calculation of properties. Because of this limitation, the well established methods of Devoto are used for the calculation of LTE properties and the less accurate expansion of Devoto's method are used for the two-temperature formulation. Furthermore, in obtaining collision integrals, the ease of obtaining a reasonable collision integral is given priority over the

accuracy of that integral. In this way, reasonably accurate transport properties are obtained within the limited time available.

4.3.1. Collision integrals

With the present work placed in context, the interactions between the various species will be considered. These interaction are described by collision integrals. The notation for collision integrals varies from work to work, but the notation of Rat et al. [72] will be used here. A collision integral between species i and species j is defined as

$$\Omega_{ij}^{(l,s)} = \left(\frac{k_b T^*}{2\pi\mu_{ij}}\right)^{1/2} \int_0^\infty \gamma^{2s+3} \exp(-\gamma^2)\, Q_{ij}^{(l)} d\gamma \tag{4.31}$$

T^* is a reduced temperature defined as

$$T^* = \left[\frac{1}{m_i + m_j}\left(\frac{m_i}{T_i} + \frac{m_j}{T_j}\right)\right]^{-1} \tag{4.32}$$

μ_{ij} is a reduced mass defined as

$$\mu_{ij} = \frac{m_i m_j}{m_i + m_j} \tag{4.33}$$

γ is a reduced energy, defined as

$$\gamma^2 = \left(\frac{\mu_{ij}}{2k_b T^*}\right) g^2 \tag{4.34}$$

where g is the relative velocity of the two species colliding. $Q_{ij}^{(l)}$ is the collision cross section, which is sometimes obtained experimentally, but more often calculated as

$$Q_{ij}^{(l)} = 2\pi \int_0^\infty (1 - cos^l \chi) b db \tag{4.35}$$

In this equation, b is an impact parameter and χ is the scattering angle, which is calculated as

$$\chi = \pi - 2b \int_{R_m}^\infty \frac{dr}{r^2 \left[1 - \left(\frac{b^2}{r^2}\right) - \left(\frac{V_{ij}(r)}{e_{ij}}\right)\right]} \tag{4.36}$$

In this equation, r is the distance between two particles in a collision, $V_{ij}(r)$ is the interaction potential of the two species colliding, $e = \frac{1}{2}\mu_{ij} g^2$, and R_m is the value of r for which the expression is brackets equals zero.

Thus, it is seen that the collision integral is a function of the temperature and the species involved which is calculated by performing a triple integral over the distance between particles, the impact parameter, and the kinetic energy of the particles relative to each other. The major decision in performing this calculation is the choice of interaction potential.

Of particular note, if the interaction potential is assumed to be a billiards ball style collision between rigid spheres of diameter σ_{ij}, then the triple integral can be completed analytically to give the closed form expression [72]

$$\left[\Omega_{ij}^{(l,s)}\right]_{rs} = \frac{(s+1)!\,[2l+1-(-1)^l]}{4(l+1)}\left(\frac{kT^*}{2\pi\mu_{ij}}\right)^{1/2}\pi\sigma_{ij}^2 \tag{4.37}$$

It is common to use this to calculate two different reduced collision integrals $\bar{Q}_{ij}^{(l,s)}$ and $\bar{\Omega}_{\mathrm{ij}}^{(\mathrm{l,s})}$, defined as

$$\bar{Q}_{ij}^{(l,s)} = \pi\bar{\Omega}_{\mathrm{ij}}^{(\mathrm{l,s})} = \pi\sigma_{ij}^2\frac{\Omega_{\mathrm{ij}}^{(\mathrm{l,s})}}{\left[\Omega_{\mathrm{ij}}^{(\mathrm{l,s})}\right]_{\mathrm{rs}}} \tag{4.38}$$

It is important to note that the values $\Omega_{\mathrm{ij}}^{(\mathrm{l,s})}$ $\bar{Q}_{ij}^{(l,s)}$, and $\bar{\Omega}_{\mathrm{ij}}^{(\mathrm{l,s})}$ are all simply referred to as "collision integrals" in various places in the literature although $\bar{Q}_{ij}^{(l,s)}$ is also sometimes called the "average collision cross section". Furthermore, different notations are sometimes used for these values. Thus, it is important to always be clear which of these values is being reported in the literature. Throughout the present work, the collision integral being used will always be clarified by consistently using the notation present in the above equations.

Neutral-Neutral

The collision integrals, $\bar{\Omega}_{\mathrm{ij}}^{(\mathrm{l,s})}$, for the interactions O-O, O-O_2, O_2-O_2, are given by Capitelli et al. [73] in the form of a polynomial with tabulated fitting coefficients. The interactions for Fe-O, Fe- Fe, and Fe-O_2 are a bit more complicated to obtain because they are not explicitly tabulated anywhere in literature. In order to avoid performing the triple integration, which can be quite complicated, non-dimensionalized collision integrals based on the Lennard-Jones interaction potential, which have been tabulated [65], are used. The Lennard-Jones potential may not be the best choice of interaction potential in the temperature range used, but the convenience of tabulated integrals outweighs the possibility of improved accuracy with other

interaction potentials. To use this tabulation, it is still necessary to obtain the coefficients of the Lennard-Jones potential function, which is defined as

$$V(r) = 4\varepsilon_{ij}\left[\left(\frac{\sigma_{ij}}{r}\right)^{12} - \left(\frac{\sigma_{ij}}{r}\right)^{6}\right] \tag{4.39}$$

where most values ε_{ij} and σ_{ij} can be found in the literature [63, 73] and are given in table 4.2. Where values of these coefficients are not available in literature, combination rules are used [74].

$$\varepsilon_{ij} = \sqrt{\varepsilon_{ii}\varepsilon_{jj}} \tag{4.40}$$

$$\sigma_{ij} = \frac{1}{2}(\sigma_{ii} + \sigma_{jj}) \tag{4.41}$$

Table 4.2. Lennard-Jones coefficients used in neutral-neutral collisions

Interaction	ε(K)	σ(m)	Reference
$O - O$	106.700	3.050e10	[73]
$O_2 - O_2$	113.000	3.433e10	[73]
$Fe - Fe$	3000.00	4.300e10	[63]
$Fe - O$	565.774	3.675e10	Combination rules
$Fe - O_2$	582.237	3.866e10	Combination rules

Neutral-Charged

The interactions O-O^+ and O_2-O_2^+ are given in [73] in the form of a polynomial fit. The remaining neutral-charged interactions, O-O^{++}, O-O_2^+, O-Fe^+, O-Fe^{++}, O-Fe^{+++}, O_2-O^+, O_2-O^{++}, O_2-Fe^+, O_2-Fe^{++}, O_2-Fe^{+++}, Fe-O_2^+, Fe-O^+, Fe-O^{++}, Fe-Fe^+, Fe-Fe^{++}, and Fe-Fe^{+++} are all found using the polarizability model . This is given in closed form as [73]

$$\bar{\Omega}_{ij}^{(1,1)}(T) = 425.4\frac{Z\sqrt{\alpha}}{\sqrt{T}} \tag{4.42}$$

$$\bar{\Omega}_{ij}^{(1,2)}(T) = 0.8333\bar{\Omega}_{ij}^{(1,1)}(T) \tag{4.43}$$

$$\bar{\Omega}_{ij}^{(1,3)}(T) = 0.7292\bar{\Omega}_{ij}^{(1,1)}(T) \tag{4.44}$$

$$\bar{\Omega}_{ij}^{(2,2)}(T) = 0.8710\bar{\Omega}_{ij}^{(1,1)}(T) \tag{4.45}$$

The variable Z depends on the charged species and is 1 for singly ionized species, 2 for doubly ionized species, and 3 for triply ionized species. The variable α depends on the neutral species and is given in table 4.3.

Table 4.3. Polarizability constants used in charge-neutral collisions

Species	α(m^3)	Reference
O	0.77e-30	[73]
O_2	1.60e-30	[73]
Fe	8.400e-30	[63]

Neutral-Electron

The interactions e-O and e-O_2 are given by [73] as a polynomial fit. The interaction e-Fe is found using the polarizability model presented in equations 4.42-4.45. This is likely a fairly poor model to use, but it is used because of its convenience and it seems to give reasonable results for the transport properties. Because higher values of s are needed for the collision integrals involving electrons, the following recursive relationship is used [74].

$$\bar{Q}_{ij}^{(1,s+1)} = \bar{Q}_{ij}^{(1,s)} + \frac{T}{s+2}\frac{\partial \bar{Q}_{ij}^{(1,s)}}{\partial T} \tag{4.46}$$

Using this relationship, we can then obtain a closed form of the polarizability potential for higher values of s.

$$\bar{\Omega}_{ij}^{(1,4)}(T) = 0.6562\bar{\Omega}_{ij}^{(1,1)}(T) \tag{4.47}$$

$$\bar{\Omega}_{ij}^{(1,5)}(T) = 0.6016\bar{\Omega}_{ij}^{(1,1)}(T) \tag{4.48}$$

Charge-Charge

All of the interactions between two charged species are obtained using a shielded Coulomb potential for the interaction potential. This is given in closed form by Devoto [6] as

$$\bar{Q}_{ij}^{(1,s)} = \left[\frac{4\pi}{s(s+1)}\right] b_0^2 \left[\ln(\Lambda) - \frac{1}{2} - 2\bar{\gamma} + \psi(s)\right] \tag{4.49}$$

$$\bar{Q}_{ij}^{(2,s)} = \left[\frac{12\pi}{s(s+1)}\right] b_0^2 [\ln(\Lambda) - 1 - 2\bar{\gamma} + \psi(s)] \tag{4.50}$$

where $\bar{\gamma} = 0.5772$ is Euler's constant, $\psi(s) = \sum_{n=1}^{s-1}(1/n)$, $\Lambda = 2d/b_0$, and b_0 is the average closest impact parameter defined as

$$b_0 = \frac{Z_i Z_j e^2}{8\pi\epsilon_0 k_b T_e} \tag{4.51}$$

In these expressions, e is the elementary charge and d is the Debye length, which is a measure of the distance needed to screen a charge in a plasma and is defined as [61]

$$d = \sqrt{\frac{\epsilon_0 k_b T_e}{e^2 n_e}} \tag{4.52}$$

where ϵ_0 is the permittivity of free space.

4.3.2. Viscosity

The viscosity for the LTE formulation is given as [4]

$$\mu = \frac{-5(2\pi k_b T)^{1/2}}{2\left|\hat{q}_{ij}^{00}\right|} \begin{vmatrix} \hat{q}_{ij}^{00} & n_i m_i^{1/2} \\ n_j & 0 \end{vmatrix} \tag{4.53}$$

where n_j is a horizontal vector, $n_i m_i^{1/2}$ is a vertical vector, and the $\hat{q}_{ij}^{00}$ variable is a sub-matrix given by

$$\hat{q}_{ij}^{00} = 8n_i \left(\frac{m_i}{m_j}\right) \sum_l \frac{n_l m_l^{1/2}}{(m_i + m_l)^{3/2}} \left[\frac{10}{3} \bar{Q}_{il}^{(1,1)} (\delta_{ij} - \delta_{jl}) m_j + 2m_l \bar{Q}_{il}^{(2,2)} (\delta_{ij} + \delta_{jl})\right] \tag{4.54}$$

Here, the summation is over all the heavy species, neglecting the electrons. The variable δ_{ij} is the Dirac delta function, which is one, if the subscripts are equal, and zero, if the subscripts are not equal. The expansion to a two-temperature formulation is very straightforward, being identical to equation 4.53, but with the heavy species temperature used.

The results of the viscosity calculation are found in figure 4.10. Good agreement is found with published results [61-63, 75] for $\theta = 1$. The disagreement for higher values of theta can be explained by the inclusion of the O_2^+ ion. At low temperatures, neutral-neutral collisions dominate

and, as the temperature increases, the mean free paths increase, causing the viscosity to increase. Upon ionization, however, the charge-neutral and charge-charge collisions become more important. These types of collisions have much larger collision cross-sections causing the mean free paths to decrease and the viscosity to decrease again. Thus, the peak in the viscosity is determined by the appearance of ions and electrons. The inclusion the O_2^+ ion generates electrons and ions at a lower temperature, as shown in figure 4.3 and 4.4, causing the peak in the viscosity to shift towards a lower temperature for θ greater than 1. It should also be noted that a small addition of iron vapor has relatively little effect on the viscosity, decreasing it slightly.

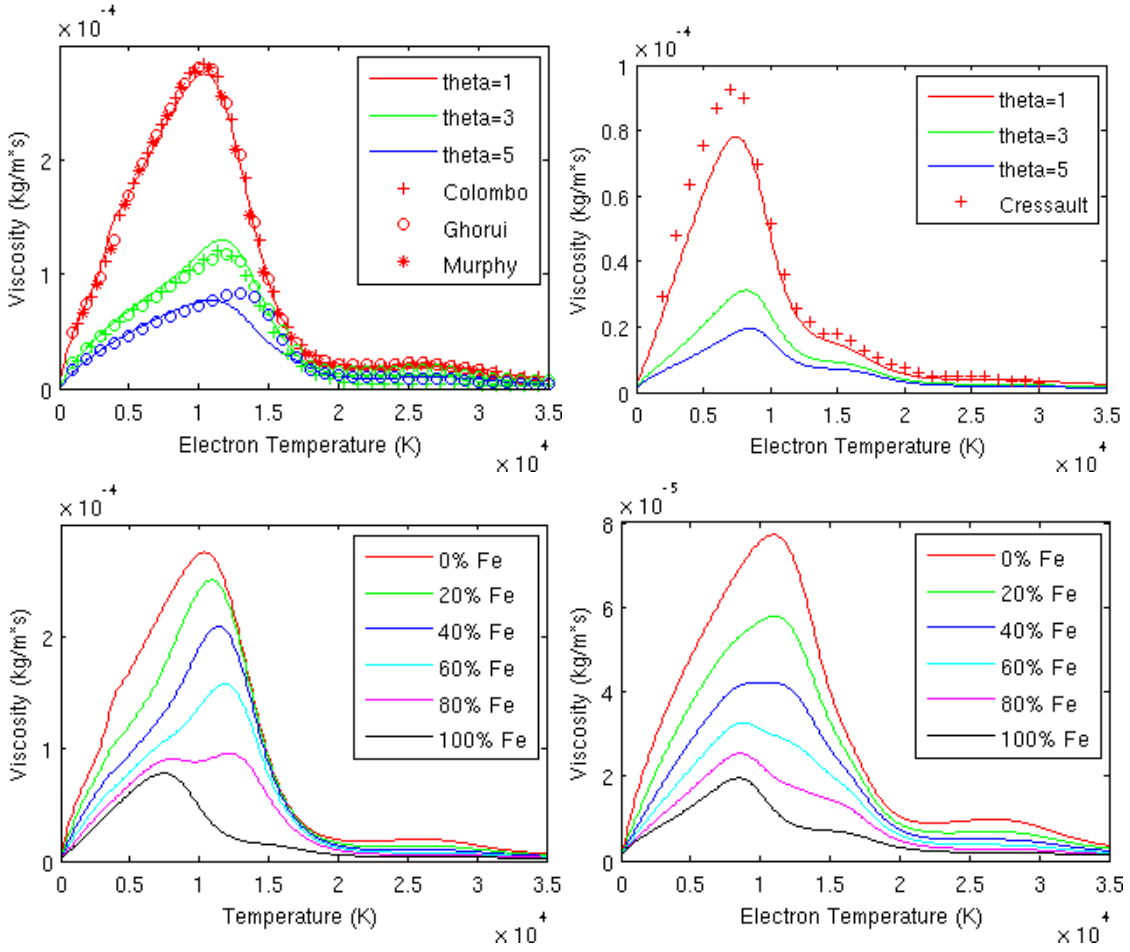

Figure 4.10. Viscosity as a function of electron temperature for various mole fractions and θ values. Pure oxygen appears top left; pure iron appears top right; $\theta = 1$ appears bottom left; $\theta = 5$ appears bottom right.

4.3.3. Electrical conductivity

The electrical conductivity for the LTE formulation is given as [5]

$$\sigma = \frac{\frac{3e^2{n_e}^2}{2k_bT}\left(\frac{2\pi k_bT}{m_e}\right)^{\frac{1}{2}}\begin{vmatrix} q^{11} & q^{12} \\ q^{21} & q^{22} \end{vmatrix}}{\begin{vmatrix} q^{00} & q^{01} & q^{02} \\ q^{10} & q^{11} & q^{12} \\ q^{20} & q^{21} & q^{22} \end{vmatrix}} \tag{4.55}$$

In this equation, e is the elementary unit of charge and the q variables are defined as

$$q^{00} = 8\sum_{j\neq e} n_e n_j \bar{Q}_{ej}^{(1,1)} \tag{4.56}$$

$$q^{01} = 8\sum_{j\neq e} n_e n_j \left[\frac{5}{2}\bar{Q}_{ej}^{(1,1)} - 3\bar{Q}_{ej}^{(1,2)}\right] \tag{4.57}$$

$$q^{11} = 8\sqrt{2}n_e^2\bar{Q}_{ee}^{(2,2)} + 8\sum_{j\neq e} n_e n_j \left[\frac{25}{4}\bar{Q}_{ej}^{(1,1)} - 15\bar{Q}_{ej}^{(1,2)} + 12\bar{Q}_{ej}^{(1,3)}\right] \tag{4.58}$$

$$q^{02} = 8\sum_{j\neq e} n_e n_j \left[\frac{35}{8}\bar{Q}_{ej}^{(1,1)} - \frac{21}{2}\bar{Q}_{ej}^{(1,2)} + 6\bar{Q}_{ej}^{(1,3)}\right] \tag{4.59}$$

$$\begin{aligned} q^{12} = {} & 8\sqrt{2}n_e^2\left[\frac{7}{4}\bar{Q}_{ee}^{(2,2)} - 2\bar{Q}_{ee}^{(2,3)}\right] \\ & + 8\sum_{j\neq e} n_e n_j \left[\frac{175}{16}\bar{Q}_{ej}^{(1,1)} - \frac{315}{8}\bar{Q}_{ej}^{(1,2)} + 57\bar{Q}_{ej}^{(1,3)} - 30\bar{Q}_{ej}^{(1,4)}\right] \end{aligned} \tag{4.60}$$

$$\begin{aligned} q^{22} = {} & 8\sqrt{2}n_e^2\left[\frac{77}{16}\bar{Q}_{ee}^{(2,2)} - 7\bar{Q}_{ee}^{(2,3)} + 5\bar{Q}_{ee}^{(2,4)}\right] \\ & + 8\sum_{j\neq e} n_e n_j \left[\frac{1225}{64}\bar{Q}_{ej}^{(1,1)} - \frac{735}{8}\bar{Q}_{ej}^{(1,2)} + \frac{399}{2}\bar{Q}_{ej}^{(1,3)} - 210\bar{Q}_{ej}^{(1,4)}\right. \\ & \left. + 90\bar{Q}_{ej}^{(1,5)}\right] \end{aligned} \tag{4.61}$$

$$q^{10} = q^{01} \tag{4.62}$$

$$q^{20} = q^{02} \tag{4.63}$$

$$q^{21} = q^{12} \tag{4.64}$$

Here, the subscript e has been used to denote variables associated with the electrons and the summation in each term is over all species except the electrons. The expansion to a two-temperature formulation is again very straightforward, being identical, except that the electron temperature is used in equation 4.55.

The results of the electrical conductivity calculation are shown in figure 4.11. The shape of the curve for $\theta = 1$ is consistent with published results. The magnitude of the electrical conductivity is slightly higher than that reported by Colombo et al. [61] and Murphy et al. [75] and slightly lower than that reported by Ghorui et al. [62]. Thus, the overall agreement for $\theta = 1$ is deemed reasonable. For larger values of θ, in the temperature range $6000 < T_e < 15000$, the results presented here differ dramatically from those reported in the literature. This is due to the inclusion of the O_2^+ ion. It has been assumed that the electrical current is carried entirely by the electrons, and thus, if there are no electrons, the electrical conductivity is near zero. Neglecting the O_2^+ ion prevents electrons from appearing until the molecules dissociate at higher electron temperatures, which is reflected in the lower values for electrical conductivity reported by the literature in this temperature range. With the O_2^+ ion included, however, electrons appear when the molecules are ionized at a lower temperature, which is reflected in the higher values of electrical conductivity reported by the present work in the temperature range $6000 < T_e < 15000$.

The inclusion of even a small fraction of iron vapor dramatically affects the electrical conductivity as well. Specifically, the lower ionization temperature of iron causes electrons to appear at a lower temperature, raising the electrical conductivity. It is evident that only a small fraction of iron is necessary in order for this effect to be manifested. This effect can be restated by saying that pure oxygen is an electrical insulator at temperatures below ~6000K whereas even a small fraction of iron vapor lowers this cutoff temperature to ~4000K. This potentially has dramatic effects on a model near an electrode where iron might be present and where such temperatures appear.

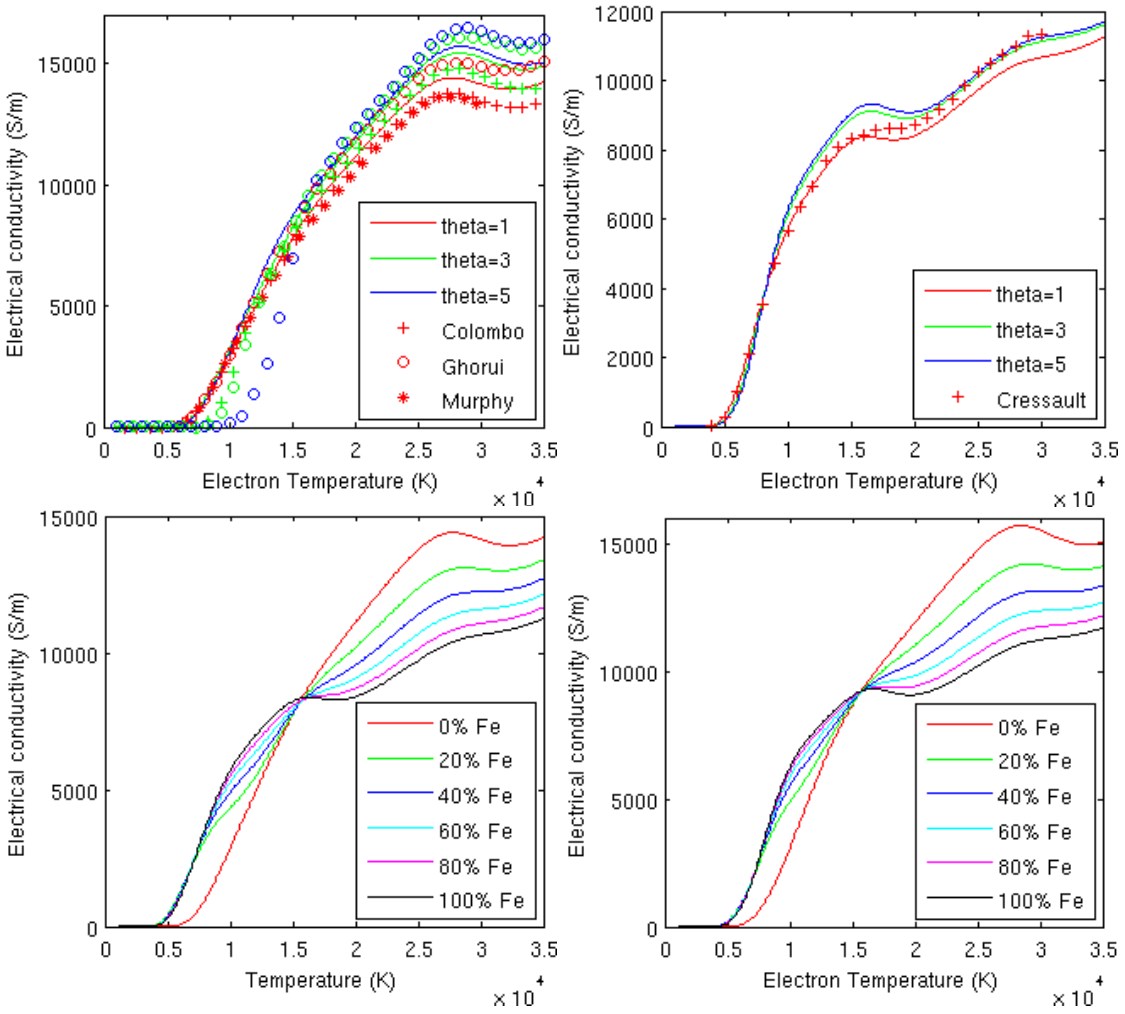

Figure 4.11. Electron conductivity as a function of electron temperature for a range of mole fractions and θ values. Pure oxygen appears top left; pure iron appears top right; $\theta = 1$ appears bottom left; $\theta = 5$ appears bottom right.

4.3.4. Thermal conductivity

The thermal conductivity can be broken into three components: the translational thermal conductivity of electrons, the translational thermal conductivity of heavy species, and the reactive thermal conductivity.

Using the LTE formulation, the translational thermal conductivity of electrons is [5]

$$\kappa_e = \frac{75 n_e^2 k_b}{8} \left(\frac{2\pi k_b T}{m_e} \right)^{1/2} \frac{1}{q^{11} - \frac{(q^{12})^2}{q^{22}}} \tag{4.65}$$

where the q variables are given above in equations 4.56-4.64. This is expanded to the two-temperature formulation by simply using T_e in equation 4.65. The results for the electron translational thermal conductivity are shown in figure 4.12. As shown, increasing θ and including iron vapors has a very minimal effect on this property. It is effectively zero at low temperatures where electrons are not present and then increases steadily with temperature as the electrons gain more translational energy. Reasonable agreement is found with the results in published literature [61-63, 75].

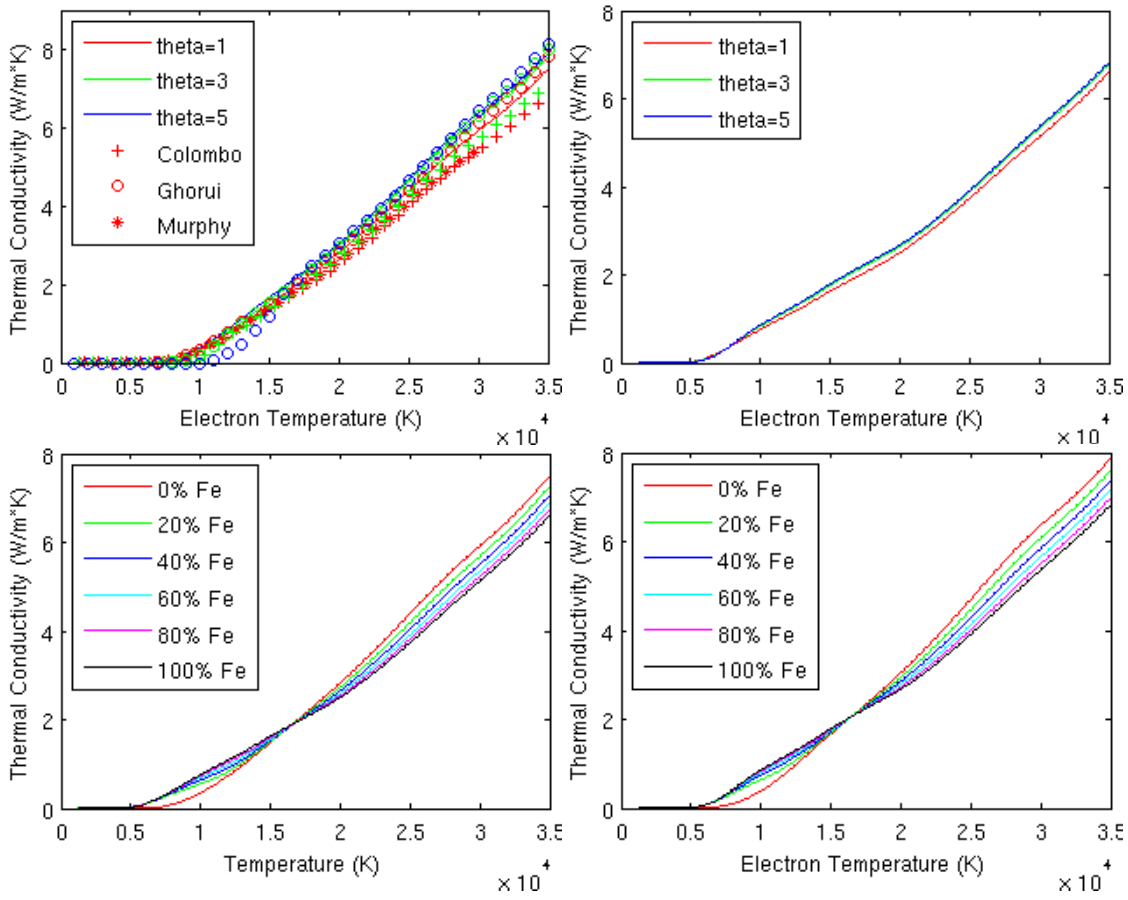

Figure 4.12. Electron translational thermal conductivity as a function of electron temperature for a range of mole fractions and θ values. Pure oxygen appears top left; pure iron appears top right; $\theta = 1$ appears bottom left; $\theta = 5$ appears bottom right.

Using the LTE formulation, the translational thermal conductivity of heavy species is given as [4]

$$\kappa_h = -\frac{75k_b}{8}\frac{(2\pi k_b T)^{1/2}}{\begin{vmatrix} q_{ij}^{00} & q_{ij}^{01} \\ q_{ij}^{10} & q_{ij}^{11} \end{vmatrix}} \begin{vmatrix} q_{ij}^{00} & q_{ij}^{01} & 0 \\ q_{ij}^{10} & q_{ij}^{11} & n_i \\ 0 & n_j/m_j^{1/2} & 0 \end{vmatrix} \tag{4.66}$$

In this equation, the q_{ij}^{mp} variables are sub-matrices given by

$$q_{ij}^{00} = 8\sum_l \frac{n_l m_i^{1/2}}{(m_i+m_l)^{1/2}}\bar{Q}_{il}^{(1,1)}\left[n_i\left(\frac{m_l}{m_j}\right)^{1/2}(\delta_{ij}-\delta_{jl}) - n_j\frac{(m_l m_j)^{1/2}}{m_i}(1-\delta_{il})\right] \tag{4.67}$$

$$q_{ij}^{01} = 8n_i\left(\frac{m_i}{m_j}\right)^{\frac{3}{2}}\sum_l \frac{n_l m_l^{\frac{3}{2}}}{(m_i+m_l)^{\frac{3}{2}}}\left[\frac{5}{2}\bar{Q}_{il}^{(1,1)} - 3\bar{Q}_{il}^{(1,2)}\right](\delta_{ij}-\delta_{jl}) \tag{4.68}$$

$$q_{ij}^{10} = \left(\frac{m_j}{m_i}\right)q_{ij}^{01} \tag{4.69}$$

$$\begin{aligned} q_{ij}^{11} = 8n_i\left(\frac{m_i}{m_j}\right)^{3/2}\sum_l \frac{n_l m_l^{1/2}}{(m_i+m_l)^{5/2}}\Big\{(\delta_{ij}-\delta_{jl})\Big[\frac{5}{4}(6m_j^2+5m_l^2)\bar{Q}_{il}^{(1,1)} \\ - 15m_l^2\bar{Q}_{il}^{(1,2)} + 12m_l^2\bar{Q}_{il}^{(1,3)}\Big] + (\delta_{ij}+\delta_{jl})4m_j m_l \bar{Q}_{il}^{(2,2)}\Big\} \end{aligned} \tag{4.70}$$

where the summation is over only the heavy species. The expansion to two-temperatures is again as simple as using the heavy species temperature in equation 4.66. The results of this are shown in figure 4.13. The character of the results is very similar to that for the viscosity. Good agreement is found with literature [61-63, 75] for $\theta = 1$ while disagreement is found for higher values of θ. The reason for this is the same as the reason for the deviation from the literature of the viscosity. Also, a small addition of iron vapor has only a minimal effect on the magnitude of the heavy species translational thermal conductivity.

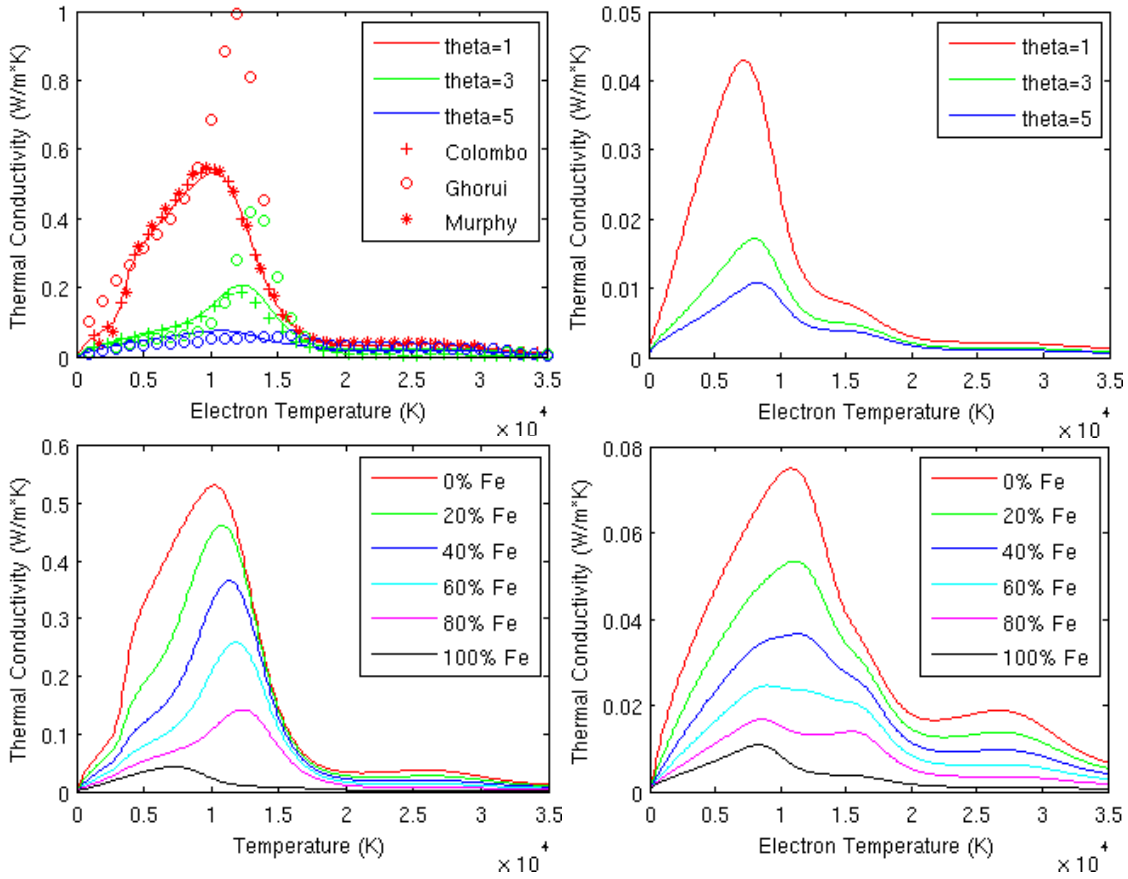

Figure 4.13. Heavy species translational thermal conductivity as a function of electron temperature for a range of mole fractions and θ values. Pure oxygen appears top left; pure iron appears top right; $\theta = 1$ appears bottom left; $\theta = 5$ appears bottom right.

The calculation of the reactive thermal conductivity is based on the work of Ghorui et al. [62], although the equations are rederived here. We begin by noting that, due to the assumption of chemical equilibrium, a gradient in temperature will give rise to gradients in the number density of each species. Given such gradients in the number densities, the equation for the number flux of a species i is given as [65]

$$\Psi_{\mathrm{i}} = \frac{n^2}{\rho} \sum_j m_j D_{ij}^a \nabla \left(\frac{n_j}{n} \right) \tag{4.71}$$

where n is the total number density and D_{ij}^a is the ordinary ambipolar diffusion coefficient, which will be defined in section 4.3.5. Because we assume chemical equilibrium, it is implicitly assumed that as these species diffuse, they immediately undergo whatever reactions must occur in

order to maintain chemical equilibrium. These reactions release or consume energy, resulting in an associated heat flux. The heat flux associated with the diffusion if a single particle is found by subtracting the enthalpy of the component atoms and electrons from the enthalpy of the species:

$$\Delta h_e = h_e - h_e = 0 \tag{4.72.a}$$

$$\Delta h_{O_2} = 2h_O - h_{O_2} \tag{4.72.b}$$

$$\Delta h_{O_2^+} = 2h_O - h_{O_2^+} - h_e \tag{4.72.c}$$

$$\Delta h_O = h_O - h_O = 0 \tag{4.72.d}$$

$$\Delta h_{O^+} = h_{O^+} - h_O - h_e \tag{4.72.e}$$

$$\Delta h_{O^{++}} = h_{O^{++}} - h_O - h_e - h_e \tag{4.72.f}$$

$$\Delta h_{Fe} = h_{Fe} - h_{Fe} = 0 \tag{4.72.g}$$

$$\Delta h_{Fe^+} = h_{Fe^+} - h_{Fe} - h_e \tag{4.72.h}$$

$$\Delta h_{Fe^{++}} = h_{Fe^{++}} - h_{Fe} - h_e - h_e \tag{4.72.i}$$

$$\Delta h_{Fe^{+++}} = h_{Fe^{+++}} - h_{Fe} - h_e - h_e - h_e \tag{4.72.j}$$

The enthalpy of a single particle of each species is calculated above in section 4.2. The total heat flux associated with the reactions is then found by multiplying the number flux of each species by the enthalpy associated with a single particle of each species.

$$q_{react} = \sum_i \Delta h_i \frac{n^2}{\rho} \sum_j m_j D_{ij}^a \nabla \left(\frac{n_j}{n}\right) \tag{4.73}$$

For the purpose of formulating a model, we would like this heat flux to be in terms of a thermal conductivity coefficient multiplying a temperature gradient. This is achieved by multiplying equation 4.73 by $\frac{\partial T}{\partial T}$, so that it takes the form

$$q_{react} = \sum_i \Delta h_i \frac{n^2}{\rho} \sum_j m_j D_{ij}^a \frac{\partial \left(\frac{n_j}{n}\right)}{\partial T} \nabla T = \kappa_r \nabla T \tag{4.74}$$

where the reactive thermal conductivity κ_r is defined as

$$\kappa_r = \sum_i \Delta h_i \frac{n^2}{\rho} \sum_j m_j D_{ij}^a \frac{\partial \left(\frac{n_j}{n}\right)}{\partial T} \tag{4.75}$$

The LTE reactivity thermal conductivity is plotted as a function of temperature in figure 4.14. As expected, this property shows peaks around dissociation and ionization temperatures. Reasonable agreement is found with literature[61, 62, 75], although the dissociation peak is a bit high and the second ionization peak is a bit low. These deviations may be due to different methods for calculating the reactive thermal conductivity or they may be due to differing order of approximation in calculating the diffusion coefficients.

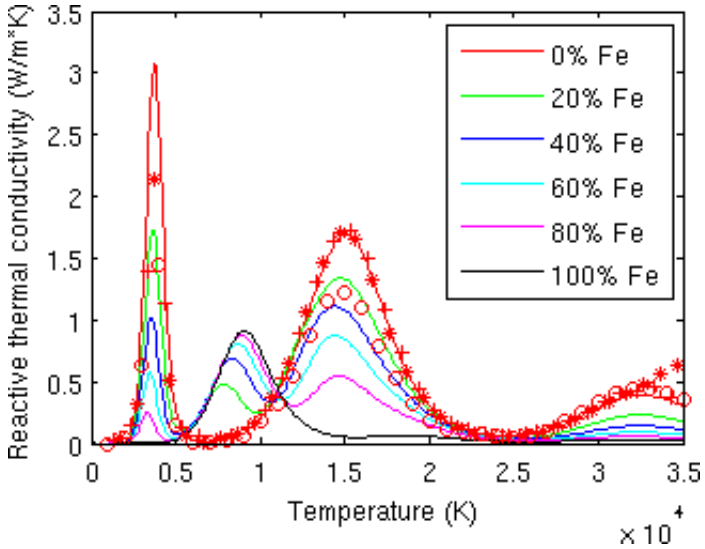

Figure 4.14. Reactive thermal conductivity for a range of iron mole fractions. Comparison with literature is shown for pure oxygen where circles designate [62], plus signs designate [61], and asterisks designate [75].

In the case of the two temperature formulation, there will be a reactive heat flux associated with the gradient in the electron temperature and a reactive heat flux associated with the gradient in the heavy species temperature. The equation for the reactive heat flux then takes the form

$$\begin{aligned} q_{react} &= \sum_i \Delta h_i \frac{n^2}{\rho} \sum_j m_j D_{ij}^a \frac{\partial \left(\frac{n_j}{n}\right)}{\partial T_e} \nabla T_e + \sum_i \Delta h_i \frac{n^2}{\rho} \sum_j m_j D_{ij}^a \frac{\partial \left(\frac{n_j}{n}\right)}{\partial T_h} \nabla T_h \\ &= \kappa_{re} \nabla T_e + \kappa_{rh} \nabla T_h \end{aligned} \tag{4.76}$$

where there are now two reactive thermal conductivities that correspond to the flow of reactive energy due to the electron temperature gradient and due to the heavy species temperature gradient.

$$\kappa_{re} = \sum_i \Delta h_i \frac{n^2}{\rho} \sum_j m_j D_{ij}^a \frac{\partial \left(\frac{n_j}{n}\right)}{\partial T_e} \tag{4.77}$$

$$\kappa_{rh} = \sum_i \Delta h_i \frac{n^2}{\rho} \sum_j m_j D_{ij}^a \frac{\partial \left(\frac{n_j}{n}\right)}{\partial T_h} \tag{4.78}$$

These properties are plotted in figures 4.15 and 4.16. The electron reactive thermal conductivity shows peaks corresponding to the ionization but not the dissociating reaction. This is quite reasonable because the ionization is most dependent on the electron temperature and the dissociation reaction is most dependent on the heavy species temperature. The combination of oxygen and iron shows the peaks of the oxygen ionization becoming smaller and the peaks of the iron ionization becoming larger for increasing iron vapor fraction. The heavy species reactive thermal conductivity for oxygen shows a single peak corresponding to the dissociation reaction of oxygen. This peak moves to higher electron temperatures for larger θ because the dissociating reaction will happen at near the same heavy species temperature regardless of the electron temperature. For pure iron, the heavy species reactive thermal conductivity is very minimal because no dissociating reactions occur in the iron and thus reactions are dominated by the electron temperature. For a combination of oxygen and iron at $\theta = 5$, the heavy species reactive thermal conductivity shows a very odd behavior. There is a range of temperatures and mole fractions for which the heavy species reactive thermal conductivity has a negative value. This is suspect and could indicate a problem in the property calculations. Because the goal of this work is to get a working model and not to advance the field of property calculations, this problem is not solved here. It is noted, however, that this is very small relative to the other components of thermal conductivity, so it will not have much effect on the overall thermal conductivity. Furthermore, this particular range of temperatures and mole fractions does not appear in the final model, meaning no component of the thermal conductivity is negative anywhere in the final model

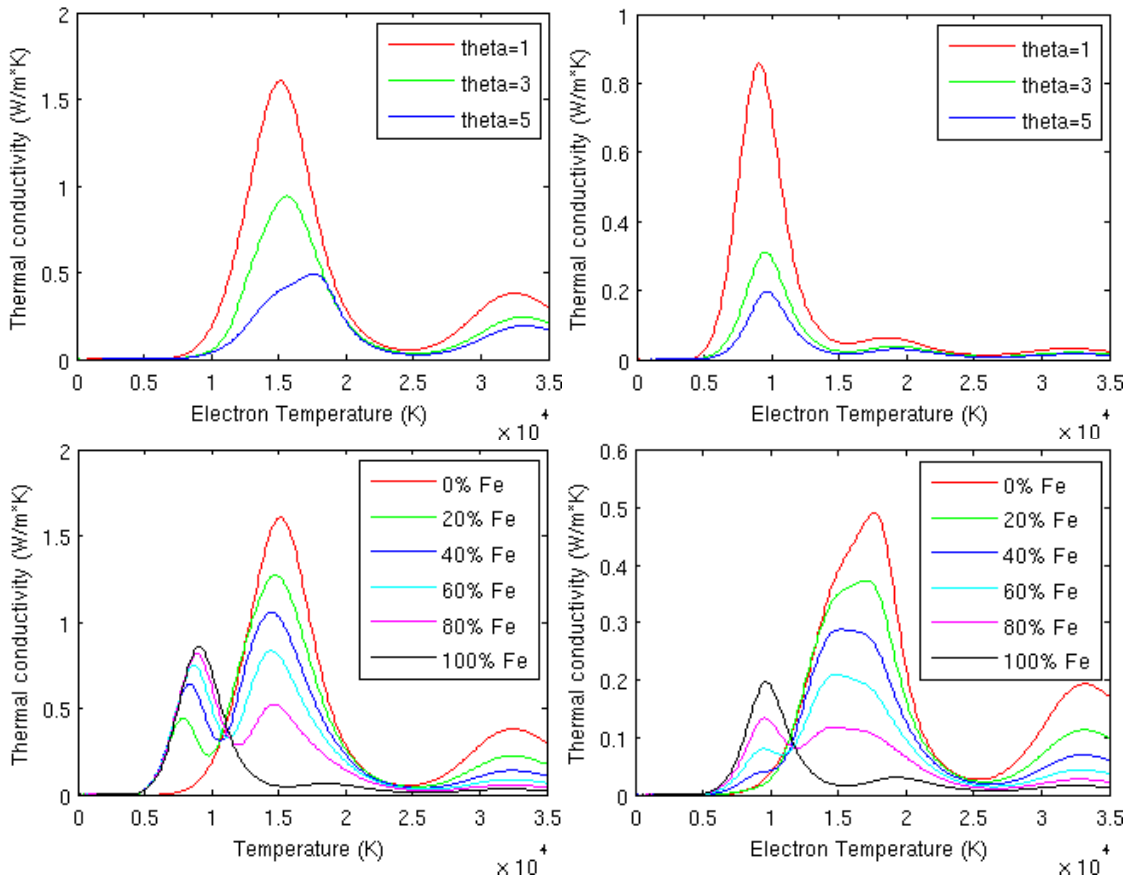

Figure 4.15. Electron reactive thermal conductivity as a function of electron temperature for a range of mole fractions and θ values. Pure oxygen appears top left; pure iron appears top right; $\theta = 1$ appears bottom left; $\theta = 5$ appears bottom right.

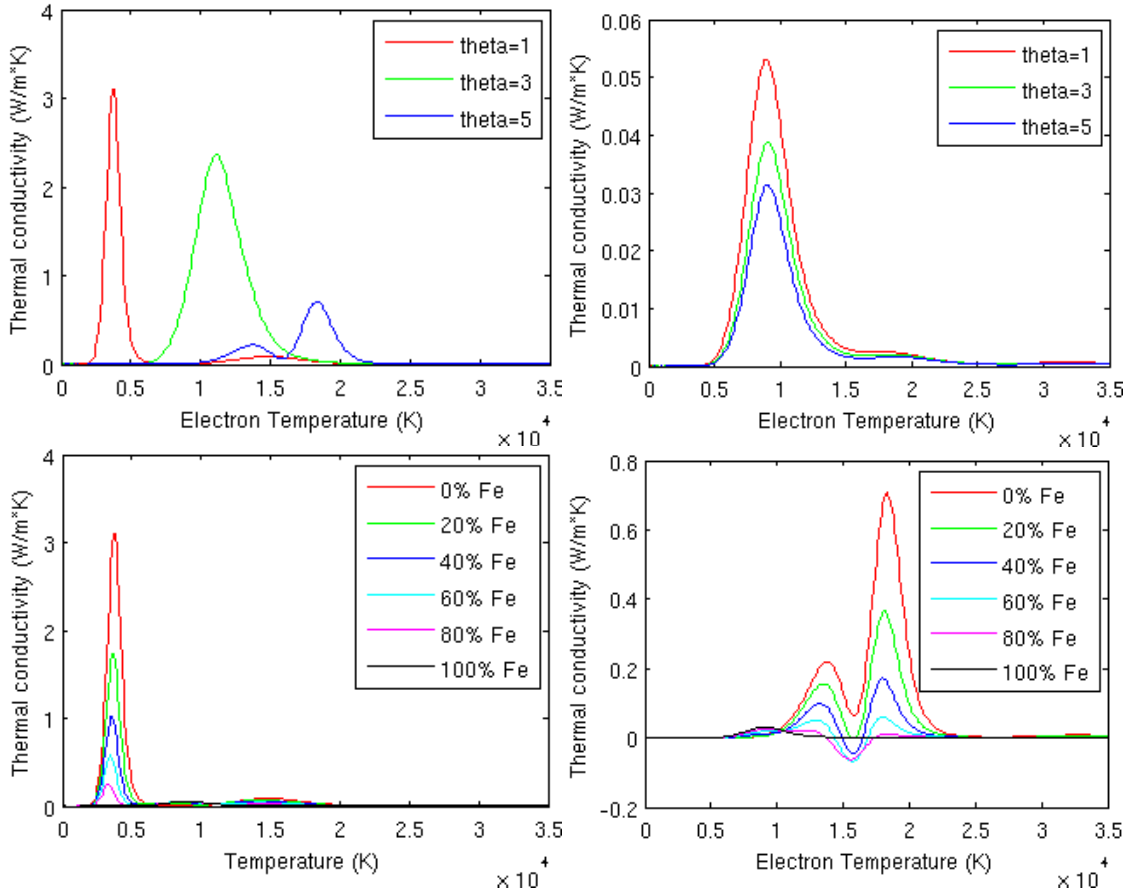

Figure 4.16. Heavy species reactive thermal conductivity as a function of electron temperature for a range of mole fractions and θ values. Pure oxygen appears top left; pure iron appears top right; $\theta = 1$ appears bottom left; $\theta = 5$ appears bottom right.

4.3.5. Diffusion coefficients

Because of the chemical equilibrium assumption, the end goal is not to model how the species diffuse relative to each other. The reactive thermal conductivity, however, includes diffusion coefficients, so it is still necessary to calculate them. Furthermore, both oxygen and iron vapor are included in the model and it is necessary to model how these two gases as a whole diffuse relative to each other. This will be done using only three combined diffusion coefficients [20]. The calculation of these combined diffusion coefficients, however, requires numerous other diffusion coefficients which must be calculated first.

First, binary diffusion coefficients will be calculated, which describe how one species diffuses relative to another if there are only the two species present. The ordinary diffusion coefficient will be calculated from this, which describes how one species diffuses relative to

another if all the other species are also present. Finally, the ordinary ambipolar diffusion coefficient will be calculated. The ambipolar correction accounts for the effects caused by charged particles diffusing while maintaining quasi-neutrality. The thermal diffusion coefficient will also be calculated and the ambipolar correction then applied to that as well.

The binary diffusion coefficient in LTE for two species, i and j, is given as [4]

$$\mathfrak{D}_{ij} = \frac{3}{16n}\sqrt{\frac{2\pi k_b T}{\mu_{ij}}}\frac{1}{\bar{Q}_{ij}^{(1,1)}} \tag{4.79}$$

The ordinary diffusion coefficients are calculated from this as [65]

$$D_{ij} = \frac{F^{ji} - F^{ii}}{m_j|F|} \tag{4.80}$$

Here, F is a matrix, whose elements F_{ij} are given by

$$F_{ij} = \left\{\frac{n_i}{\rho\mathfrak{D}_{ij}} + \sum_{l\neq i}\frac{n_l m_j}{\rho m_i \mathfrak{D}_{il}}\right\}\left(1-\delta_{ij}\right) \tag{4.81}$$

The notation F^{ij} is defined as

$$F^{ij} = (-1)^{i+j}\begin{vmatrix} F_{1,1} & \cdots & F_{1,j-1} & F_{1,j+1} & \cdots & F_{1,last} \\ \vdots & & \vdots & \vdots & & \vdots \\ F_{i-1,1} & \cdots & F_{i-1,j-1} & F_{i-1,j+1} & \cdots & F_{i-1,last} \\ F_{i+1,1} & \cdots & F_{i+1,j-1} & F_{i+1,j+1} & \cdots & F_{i+1,last} \\ \vdots & & \vdots & \vdots & & \vdots \\ F_{last,1} & \cdots & F_{last,j-1} & F_{last,j+1} & \cdots & F_{last,last} \end{vmatrix} \tag{4.82}$$

This is quite complicated looking, but the matrix is simply the F matrix with the ith row and jth column removed. The ambipolar correction is next calculated following the work of Murphy [20].

$$D_{ij}^{a} = D_{ij} + \frac{\alpha_i}{\beta}\sum_{l} Z_l D_{lj} \tag{4.83}$$

where

$$\alpha_i = \sum_j n_j m_j Z_j D_{ij} \tag{4.84}$$

$$\beta = -\sum_i\sum_j Z_i Z_j n_j m_j D_{ij} \tag{4.85}$$

These are the diffusion coefficients used in equations 4.73-78 for calculating the reactive thermal conductivity.

The thermal diffusion coefficient of the electrons is calculated as [5]

$$D_e^T = -\frac{15{n_e}^2}{4}\frac{\sqrt{2\pi m_e k_b T}}{q^{01} - q^{00}q^{11}/q^{01}} \tag{4.86}$$

where the q terms are given in equations 4.56-64. The thermal diffusion coefficients of the heavy species are given to as [4]

$$D_i^T = \frac{15n_i\sqrt{2\pi m_i k_b T}}{4|q|}\begin{vmatrix} q_{hk}^{00} & q_{hk}^{01} & 0 \\ q_{hk}^{10} & q_{hk}^{11} & n_h \\ \delta_{ki} & 0 & 0 \end{vmatrix} \tag{4.87}$$

where the q terms are defined in equations 4.67-70. The ambipolar correction is then applied to these thermal diffusion coefficients using the equation given by Murphy [20]

$$D_i^{Ta} = D_i^T + \frac{\alpha_i m_i}{\beta}\sum_l \frac{Z_l D_l^T}{m_l} \tag{4.88}$$

where α_i and β are defined in equations 4.84-85.

The diffusion coefficients under the two-temperature assumption are calculated in the same way using equations 4.79-88. The only difference is that a reduced temperature, given in equation 4.32, is used instead of the LTE temperature in equation 4.79, the electron temperature is used in equation 4.86, and the heavy species temperature is used in equation 4.87.

4.3.6. Combined diffusion coefficients

Because ten species are used in the model, there are a total of one hundred ordinary ambipolar diffusion coefficients and ten thermal diffusion coefficients. Because we assume chemical equilibrium, however, we are only really interested in how the iron vapor diffuses relative to the oxygen and not how each of the individual species diffuse relative to each other. As such, the combined diffusion coefficient method of Murphy [20] is an ideal option because it reduces the diffusion problem to three coefficients. It should be noted that this method requires that each heavy species be attributed to one and only one gas. This is a large part of the reason that FeO was neglected in the calculations of plasma composition and properties. The species FeO would belong to both the iron and the oxygen gas, making it impossible to use the combined diffusion coefficient method.

We will adopt here the species numbering convention used by Murphy. The electrons correspond to species 1. The oxygen species, O, O_2, O_2^+, O^+, O^{++} correspond to species 2 through p. The iron species, Fe,Fe^+, Fe^+, Fe^{+++} correspond to species $p+1$ through q, where there are a total of q species. The diffusion mass flux of iron gas through oxygen gas is then given by

$$\overline{J_{Fe}} = \overline{m_{Fe}}\frac{n^2}{\rho}\overline{m_O}\left\{\overline{D_{FeO}^x}\nabla\overline{x_O} + \overline{D_{FeO}^p}\nabla\ln(p)\right\} - \overline{D_{FeO}^T}\nabla\ln(T) \tag{4.89}$$

here, the bar across the top of a variable designates that the variable pertains to an entire gas and not just a single species. The gas averaged mass variables are defined as

$$\overline{m_O} = \frac{\sum_{k=2}^{p}(m_k x_k + m_1 Z_k x_k)}{\sum_{k=2}^{p} x_k} \tag{4.90}$$

$$\overline{m_{Fe}} = \frac{\sum_{k=p+1}^{q}(m_k x_k + m_1 Z_k x_k)}{\sum_{k=p+1}^{q} x_k} \tag{4.91}$$

where x is the mole fraction of a specie. The mole fraction of the oxygen gas in equation 4.89 includes both the oxygen species and the electrons needed to maintain the quasi neutrality of those species.

$$\overline{x_O} = \sum_{k=2}^{p}(1+Z_k)x_k \tag{4.92}$$

The variables $\overline{D_{FeO}^x}$, $\overline{D_{FeO}^p}$, and $\overline{D_{FeO}^T}$ are respectively the combined ordinary diffusion coefficient, the combined pressure diffusion coefficient, and the combined thermal diffusion coefficient. These are defined as follows:

$$\overline{D_{FeO}^x} = \frac{1}{\overline{m_O}}\sum_{i=p+1}^{q} s_i \sum_{j=1}^{q} m_j D_{ij}^a \frac{\partial x_j}{\partial \overline{x_O}} \tag{4.93}$$

$$\overline{D_{FeO}^p} = \frac{1}{\overline{m_O}}\sum_{i=p+1}^{q} s_i \sum_{j=1}^{q} m_j D_{ij}^a \left(x_j - \frac{m_j n_j}{\rho} + P\frac{\partial x_j}{\partial P}\right) \tag{4.94}$$

$$\overline{D_{FeO}^T} = \overline{m_{Fe}}\sum_{i=p+1}^{q} s_i \left(\frac{D_i^{Ta}}{m_i} - \frac{n^2}{\rho}\sum_{j=1}^{q} m_j D_{ij}^a T\frac{\partial x_j}{\partial T}\right) \tag{4.95}$$

Here, s is defined as

$$s_i = 0 \qquad i = 1 \tag{4.96.a}$$

$$s_i = \frac{b_i \sum_{k=2}^{p} x_k}{\sum_{k=2}^{p} b_k x_k} \qquad 2 \le i \le p \tag{4.96.b}$$

$$s_i = \frac{b_i \sum_{k=p+1}^{q} x_k}{\sum_{k=p+1}^{q} b_k x_k} \qquad p+1 \le i \le q \tag{4.96.c}$$

where b is 1 for monatomic species and 2 for diatomic species.

In expanding to the two temperature formulation, it is assumed that most of the thermal diffusion depends on the heavy species and thus the heavy species temperature is used in the calculation of the combined diffusion coefficients. Otherwise, no change was made between the LTE formulation and two-temperature formulation. It should be noted that the two temperature combined diffusion coefficients are likely a weak area of the present research. In comparing the method of Rat et al. to the method of Devoto, Colombo et al. found the largest deviation in the diffusion coefficients.

These combined diffusion coefficients are plotted in figure 4.17.

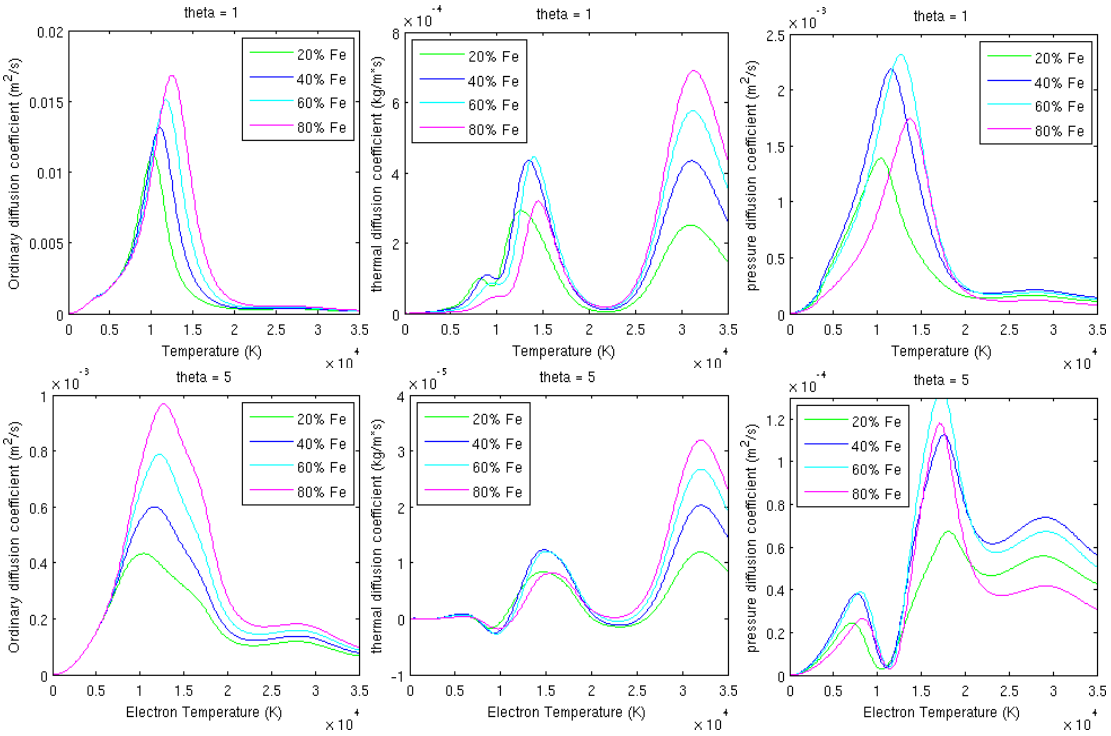

Figure 4.17. Combined diffusion coefficients of an oxygen iron mix at $\theta = 1$ and $\theta = 5$.

4.4. Application to the Plasma Model

This chapter has shown how for a given pressure, electron temperature, heavy species temperature, and mole fraction of iron the necessary plasma properties are calculated. In practice, it is cumbersome and computationally expensive to perform these calculations during the simulation of the plasma flow in the cutting process. Instead, lookup tables are generated before hand and then used when the properties are required in the plasma model. These tables are generated for a larger range of temperatures and pressures than are expected to appear in the final results because there is a very real possibility that unphysical high or low values will appear in the model for a short period due to unphysical initial conditions.

The LTE properties are simply tabulated as a function of temperature, pressure and mole fraction of iron. The choice of independent variables in tabulating the two-temperature properties requires a bit more attention. It is quite common to tabulate the properties as a function of pressure, electron temperature, non-equilibrium parameter $\theta = T_e/T_h$, and mole fraction. This has the advantage of producing a smaller property table because θ only ranges at most from one to ten. In the present work, however, the properties are tabulated as a function of pressure, electron temperature, heavy species temperature, and mass fraction. This produces a larger table because T_h must range from 100 to 40000K. This is necessary, however, and the need can be explained with a thought experiment:

Consider the situation in which $p = 1atm$, $T_e = 6000K$, and $T_h = 4000K$. This is a situation that is likely to occur somewhere within the plasma simulation domain. This gives a value of $\theta = 1.5$. If the properties of the plasma are tabulated using θ in steps of 1, and T_e in steps of 100 then the lookup value for this situation will be interpolated between $\theta = 1$ and $\theta = 2$, which corresponds to $T_h = 3000K$ and $T_h = 6000K$, giving only $3000K$ resolution. The value of $\frac{\partial h_h}{\partial T_h}$ is plotted in fig 4.18 for $\theta = 1$ and $\theta = 2$. It is apparent that the interpolated value will fall somewhere much below the dissociation peak in this property, when, in fact, it should be somewhere close to the peak. This particular situation can be remedied by decreasing the θ step to 0.5. This, however, still only gives a T_h resolution of $1500K$, which is insufficient to resolve the dissociation peak in $\frac{\partial h_h}{\partial T_h}$, which is most dependent on the heavy species temperature. An extremely small θ step would be required in order to resolve this, which dramatically increases

the size of the property table. Thus, it is much more reasonable to simply write the table in terms of heavy species temperature instead of θ.

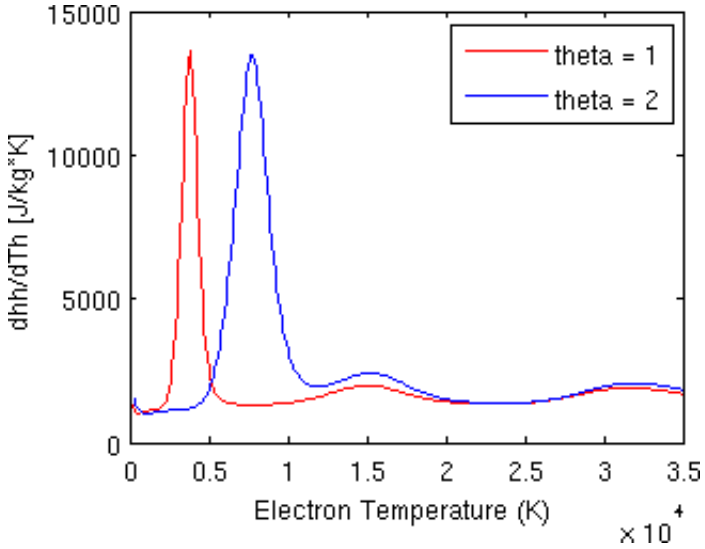

Figure 4.18. Partial derivative of heavy species enthalpy with respect to heavy species temperature for consecutive values of theta.

Chapter 5

Numerical Implementation of the Model

In undertaking the present numerical simulations, the mathematical formulations presented in chapters 3 and 4 are arguably the most import aspect because they reflect the physical realities. In order to obtain results for the numerical simulation, however, it is necessary to discretize these equations across a domain of interest and implement an algorithm or set of algorithms to solve these equations. Doing this in such a way that it is both accurate and numerically stable is no small undertaking. Thankfully, the field of computational fluid dynamics (CFD) is already quite well developed. Thus, it is neither necessary nor within the scope of this work to redevelop the field of CFD. It will be sufficient to state that the finite volumes method is used, for which the details can be found in textbooks [2, 76]. Furthermore, the fundamentals of discretization and solution algorithms are largely built into OpenFOAM. Thus, the use of OpenFOAM dodges many difficulties with respect to numerical stability.

There is still, however, a significant amount of work that needs to be done in order to obtain a numerically stable plasma model, which will be discussed in this chapter. While, over all, finite volume discretization is used, it is necessary to choose what particular schemes are used for each term. This will vary from term to term within the governing equations. It is also necessary to consider the use of implicit versus explicit discretization. Because implicit discretization will give rise to sparse, diagonally dominate matrices that must be solved, consideration will then be given to the matrix solvers used. OpenFOAM has a number of built in solvers, of which some are better suited to the problem at hand than others. Attention must also be given to the overall algorithm used to resolve the coupling between all of the equations. This will be based off of the PISO algorithm with additional attention given to the two temperature

energy equations. There are also some stability issues particular to the electro-magnetic equations which will be given specific attention. Finally, the parallelization of the code will be discussed.

5.1. Discretization of Individual Terms

5.1.1. Finite volume discretization schemes

There are numerous available discretization schemes that can be chosen within OpenFOAM. It is beyond to the scope of this work, however, to explore all of these in detail. Rather, the schemes chosen for different terms will be given and some notes made on the reason for choosing them. There are, roughly speaking, four different types of terms: transient, advective, diffusive and reactive. Each of these is treated somewhat differently in discretization, and so, they will be approached one at a time.

A transient term has the general form

$$\frac{\partial \rho \varphi}{\partial t} \tag{5.1}$$

where φ is the variable being solved for. OpenFOAM offers a choice between Euler explicit, Euler implicit, or Crank Nicholson discretization with respect to time. Because of the strong non-linear character of the plasma equations, the Euler explicit is clearly a poor choice for stability reasons. The Crank Nicholson method would seem the best choice because it has second order accuracy where as the Euler implicit has only first order accuracy. In practice, however, it was not possible to achieve numerical stability with the Crank Nicholson method and thus the Euler implicit scheme was used for all temporal discretization in the present work.

A diffusive term has the general form of a laplacian

$$\nabla \cdot \alpha \nabla \varphi \tag{5.2}$$

where φ is the variable being solved for and α is some coefficient that is a property of the fluid. This term is commonly solved using a Gaussian linear discretization. OpenFOAM also utilizes a correction to this scheme to account for non-orthogonality of the mesh. This scheme was used because it is very standard, has second order accuracy, and produces satisfactory numerical stability.

The reactive term is simply a source term having the general form

$$S_u + S_p \varphi \tag{5.3}$$

where φ is the variable being solved for and S_u and S_p are source coefficients. Because of the simplicity of the source term, the only choice present is between implicit or explicit discretization of S_p. For numerical stability, implicit discretization is chosen when possible.

The advective term has the general form

$$\nabla \cdot \psi\varphi \tag{5.4}$$

where ψ is the flux through the faces and φ is the variable being solved for. This term generally produces the greatest difficulties with regard to numerical stability. If the velocities present are small relative to the rate of diffusion, the second order accurate Gaussian linear discretization can be used. At higher velocities, such as are present in the current work, this quickly becomes unstable. The simplest fix is to use an upwind discretization, which takes the flux values at faces from the upstream direction. This is very stable but at the cost of having only first order accuracy. The desire for a stable, second order accurate discretization of advection terms has led to the development of a family of total variation diminishing (TVD) discretization schemes which apply a "limiter" that prevents numerical instability. OpenFOAM makes available a number of these schemes, but only the "limitedLinear" TVD schemes was tested in this work. Unfortunately, while the 2nd order TVD scheme was generally stable, it still produced occasional instabilities that could not be fixed using smaller time steps, relaxation factors, or any other commonly used techniques. Thus, the upwind scheme exclusively was used in the results presented in chapter 7. This will have the effect of introducing numerical diffusion that will tend to smooth out steep gradients and flow instabilities. The overall trends of the plasma flow, however, will still be correctly solved.

5.1.2. Implicit versus explicit discretization

The concept of implicit and explicit discretization is mentioned above with respect to transient and source terms. More detail is given here.

Consider a partial differential equation that is being solved for a given variable, φ, at a time denoted by $n + 1$, where the value of φ is known every where at the time n. The simplest method to discretize each term would involve using the value of φ at time n. This is refered to as explicit discretization and gives the value of φ at time $n + 1$ at each cell entirely in terms of know values. The down side of this method is that is places very tight restrictions on the length of time step that can be used while maintaining numerical stability. Alternatively, each term could be discretized using the value of φ at time $n + 1$. This is referred to as implicit discretization and

gives the value of φ at time $n+1$ at each cell in terms of unknown values of φ at time $n+1$ in the surrounding cells. Thus, implicit discretization produces N equations with N unknows where N is the number of cells in the domain of interest. These equations produce a sparse, diagonally dominant matrix that must be solved. While, on the face of it, implicit discretization seems more complicated than it is worth, it has excellent numerical stability.

Because of the extremely beneficial numerical stability arising from implicit discretization, it is used wherever possible. Specifically, this occurs in the advection and diffusion terms of the governing equations. In light of implicit vs. explicit discretization, particular attention must be given to the term that captures the exchange of energy between the electrons and heavy species in the two temperature formulation. This expression is given as in equation 3.20

$$\dot{Q}_{eh} = \sum_{s \neq e} 3k_b \frac{m_e}{m_i} n_e \nu_{ei} (T_e - T_h) \delta_{ei} \tag{5.4}$$

In this form, it cannot be discretized implicitly because it does not match the form of Sp in equation 5.3. Explicit discretiztion, however, leads to severe instabilities. Given explicit discretization and too large of a time step, instead of the two temperatures equilibrating towards each other, they will over shoot each other and move apart in the opposite direction on a given time step. On the next time step, they will overshoot and move further apart in the original direction. This oscillation quickly grows out of control and the model diverges. In order to avoid this instability, the term is rewritten as

$$\dot{Q}_{eh} = \sum_{s \neq e} 3k_b \frac{m_e}{m_i} n_e \nu_{ei} \delta_{ei} T_e - \sum_{s \neq e} 3k_b \frac{m_e}{m_i} n_e \nu_{ei} \delta_{ei} T_h \tag{5.5}$$

This now matches the form given in equation 5.3 where the first term can be discretized implicitly in the electron energy equation and the second term can be discretized implicitly in the heavy species energy equation.

5.2. Sparse Matrix Solvers

The use of implicit discretization produces a sparse diagonally dominant matrix. Direct solution of such matrices is generally inefficient, but OpenFOAM provides a variety of iterative matrix solvers to choose from. Each has advantages and disadvantages. The available solvers will first be described and then the choice of solvers will be explained.

5.2.1 Available matrix solvers

One of the most intuitive matrix solvers is the Gauss-Seidel solver. At each iteration, each cell is updated using currently stored data from the surrounding cells. After a sufficient number of iterations, each cell will reach the calculated value for the new time and thus each cell will be calculated based on the new values calculated for the surrounding cells. The simplicity of this solver makes it computationally very cheap to set up at each iteration. The major drawback of the Gauss-Seidel solver is that it can take a large number of iterations to converge. In particular, data can only "move" one cell space per iteration. Thus, if the boundaries strongly influence the interior of the domain, it will take a significant number of iterations before the middle of the domain will even "see" the boundaries.

The generalized geometric-algebraic multi-grid (GAMG) solver fixes some of the problems with the Gauss-Seidel method. The domain is first agglomerated into a very course grid and the equation is solved on this course grid. This is then mapped to progressively finer grids and solved on those, eventually becoming refined to the original grid. Because the coarsest grid has so few cells and each refinement starts with an excellent guess, relatively few iterations are required to solve the equation at each stage. The GAMG solver excels particularly when information needs to be communicated everywhere in the domain at once because the course mesh does this in very few iterations. The drawback of the GAMG solver is that the complexity makes it computationally more expensive to set up at each iteration.

OpenFOAM also supplies a preconditioned bi-conjugate gradient (PBiCG) solver for asymmetrical matrices and a preconditioned conjugate gradient (PCG) solver for symmetric matrices. These are slightly more complicated to set up than the Gauss-Seidel method requiring slightly more computation time to set up, but converge in fewer iterations, making them overall computationally cheaper. The PBiCG and PCG solvers are widely used as the defaults in OpenFOAM although they have been rejected in this work because they are found to have unknown stability problems in the present application.

5.2.2 Chosen matrix solvers

The equations governing magnetic potential and electric potential are purely laplacian type equations. This means that the effect of each boundary condition is felt everywhere in the domain. As such, the GAMG solver is ideal for solving these equations, whereas the Gauss-Seidel solver was sometimes found to require 100-1000 times more iterations to converge.

Because of the very high velocities in the present work, the energy, momentum, and mass fraction of iron are primarily affected by the cells relatively near to them (primarily those shortly upstream). Thus, in solving the governing equations for these, relatively few Gauss-Seidel iterations are needed to reach a converged result, making it the ideal solver. The GAMG solver on the other hand requires so much additional computation time to set up that it is computational more expensive for these field.

The character of the pressure equation lies somewhere in the middle. Early in the simulation, when the initial conditions are still washing out of the domain, a very large number of Gauss-Seidel iterations may be necessary in order to reach a converged solution. As the simulation approaches a steady or quasi-steady state, however, there are only small changes in the pressure field and it converges in only a few iterations. Thus, because the majority of the simulation is concerned with approaching steady state, the Gauss-Seidel solver was found to be computational cheaper.

5.3. PISO Algorithm

It is necessary to pay particular attention to the method used to resolve the coupling of the governing equations. The two most widely used methods for solving flow equations are the SIMPLE (Semi-Implicit Method for Pressure Linked Equations) algorithm [2] used for steady state simulations and the PISO (Partially Implicit Split Operator) algorithm [3] used for transient simulations. In the present work, the PISO algorithm is used in order to capture transient effects. For the LTE formulation, the version already implemented in OpenFOAM can be used with relatively little modification. This is outlined in figure 5.1. The only modifications involve the addition of the plasma specific terms in the energy and momentum equations, the use of the plasma properties, and the inclusion of the electromagnetic (E&M) equations.

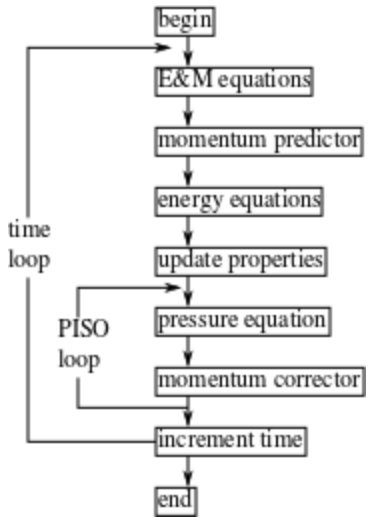

Figure 5.1. Schematic of PISO algorithm

5.3.1. Solution of two-temperature energy equations

To a large extent the PISO algorithm displayed in figure 5.1 can also be used for the two-temperature formulation. The solution of the energy equation, however, which becomes two separate, but tightly coupled, equations requires particular attention. While these two equations are coupled through a number of terms, as well as the thermodynamic and transport properties, the most important coupling term is the electron/heavy species energy exchange term. As explained in section 5.1.2, a great degree of stability is achieved in this term by using a partially implicit instead of a fully explicit discretization. Even this, however, is often not sufficient to achieve stability. To explore the stability of the term further, we define a variable

$$q_{eh}(p, T_e, T_h, Y) = \sum_{s \neq e} 3k_b \frac{m_e}{m_i} n_e \nu_{ei} \delta_{ei} \tag{5.6}$$

such that

$$\dot{Q}_{eh} = q_{eh}(T_e - T_h) \tag{5.7}$$

It is evident that q_{eh} can be calculated ahead of time and tabulated in the same way as the properties in chapter 4. This property is plotted in figure 5.2 where it is evident that even a small change in temperature can give rise to very large changes in q_{eh}. This characteristic causes instabilities. At one time step, the value of q_{eh} may be too large, causing the temperatures to overshoot the correct value relative to each other. This causes q_{eh} to be too small when it is updated for the next time step. The temperatures then overshoot the correct values relative to each other in the opposite direction. The resulting oscillation around the correct value can grow out of

control causing the results to diverge. It should be noted that this is not a problem for the properties in chapter 4 because they do not change by orders of magnitude over just a few thousand degrees Kelvin. The net emission coefficient, shown in figure 3.2, however, does have this characteristic. In practice, however, q_{eh} causes the greatest problems.

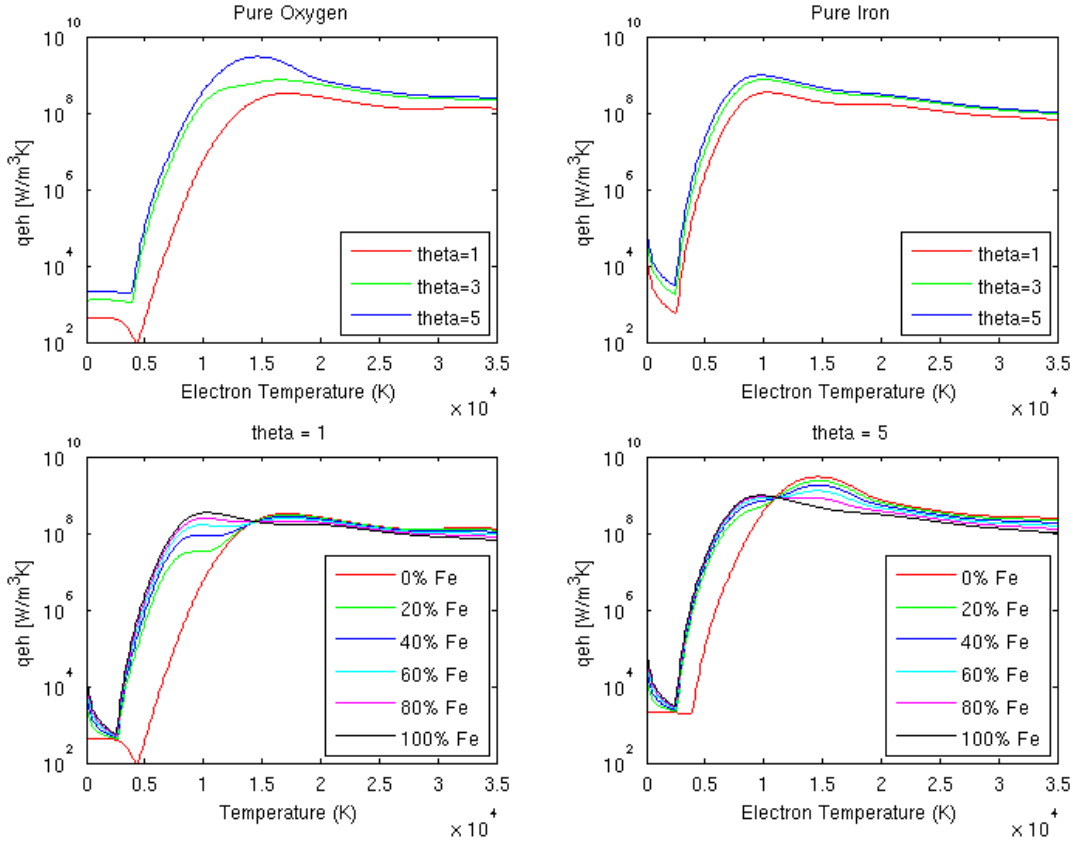

Figure 5.2. The q_{eh} coefficient in the energy transfer term between electrons and heavy species. Pure oxygen appears top left; pure iron appears top right; $\theta = 1$ appears bottom left; $\theta = 5$ appears bottom right.

In order to avoid this instability, the solution method illustrated in figure 5.3 is employed. A pair of sparse matrices containing the non-coupling terms is first built and stored. A pair of sparse matrices containing the full equations is built and stored by adding the coupling terms to the non-coupled matrices. A very strict relaxation factor of .1 is applied to these matrices and they are solved. The net emission coefficient and q_{eh} property are then updated using the new temperature values. A new pair of sparse matrices are again generated, relaxed and solved by adding the coupling terms again to the original non-coupled matrices. This is iterated until the residual is less than a given criterion. At this point, it is assumed that the correct values of q_{eh}

and the net emission coefficient have been obtained and sparse matrices for the entire equations are rebuilt and solved.

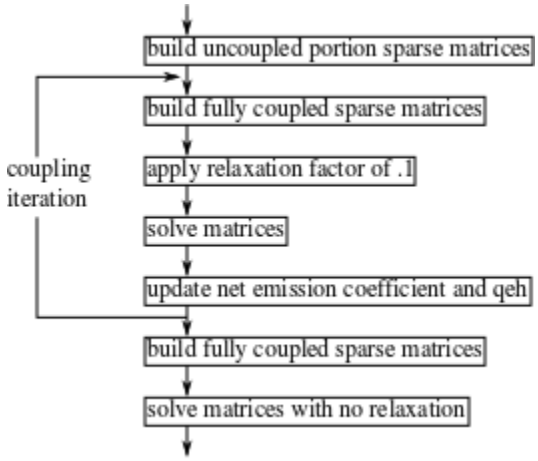

Figure 5.3. Schematic of algorithm used to solve coupled, two temperature, energy equations within the PISO algorithm.

Very few Gauss-Siedel iterations are needed to solve the relaxed energy equations at each coupling iteration. Thus, the largest part of the computational expense comes from setting up the sparse matrices that describe the equations and in updating the net emission coefficient and q_{eh} property at each coupling iteration. Because of the number of iterations needed to resolve the coupling of the energy equations, the majority of computation time is spent on solving the energy equations.

In doing this, the reason for using the derivative method of formulating the energy equations instead of the definition method in section 3.3.4 becomes clear. The definition method does not use the partial derivatives in the energy equations, but uses the number density of each species in the term that contains reactive energy. The number densities all have a characteristic similar to the q_{eh} property that they can change by orders of magnitude over a just a few thousand degrees Kelvin, which has a destabilizing effect on the simulation. This could be resolved using the same coupling iterations that are used to resolve the difficulties with q_{eh}. However, this requires that the ten additional number densities are also updated for each coupling iteration instead of just the net emission coefficient and q_{eh} property. Because the updating of properties is a major computational cost of this iteration method, this would add significantly to the overall computational cost of the simulation.

There is an additional stability problem in the two temperature equation that cannot be resolved through iteration. At low temperatures, there is no ionization and thus no electrons. The electron energy equation, however, must still be solved in these low regions. Thus, following the methods of Trelles [11], it is assumed that the electron temperature rapidly equilibrates to the heavy species temperature at low temperatures. This is enforced by artificially increasing the exchange term between electrons and heavy species by setting the electrons density in equation 5.6 as suggested by Trelles.

$$n_e = \max(n_e, 1e18) \tag{5.8}$$

This has no effect on the core of the arc and only serves to lower the electron temperature to the heavy species temperature in the far fringes of the arc.

5.4. Electromagnetic Equations

5.4.1. Stability of electric potential equation

The equation governing the electric potential is a simple laplacian type equation with the electrical conductivity serving as a diffusion type coefficient.

$$\nabla \cdot \sigma \nabla \phi = 0 \tag{5.9}$$

The electrical conductivity has values as high as 15000 S/m, but also approaches zero at low temperatures. As the electrical conductivity approaches zero, it causes severe stability problems because the coefficient itself is less than the convergence tolerance of the sparse matrix solver.

To a certain degree, stability can be obtained by setting an extreme tight convergence tolerance. While this helps, the tighter convergence criterion requires an order of magnitude or more increase in computation time. Even then, it does not always fix the stability problem. A superior solution consists of artificially increasing the electric conductivity by a set amount everywhere in the domain. An addition of 1 S/m was found to stabilize the solution while having no effect on the final result or computation time.

5.4.2. Time step considerations

The electromagnetic equations are troublesome when trying to optimize the code to run quickly and efficiently. As mentioned above, they are laplacian type equations, which communicate information everywhere in the domain all at once. As such, for a given sparse matrix solver, they take 10-100 times as many iterations to reach a converged solution. This is somewhat alleviated by using the AMG solver as mentioned in section 5.2. The solution of the

electromagnetic equations, however, still requires a much larger computation time than the pressure or momentum equations.

The computation time for the electromagnetic equations can be greatly reduced, however, by considering the time step used. The time step used in the PISO algorithm is set by the stability and accuracy requirements needed for the pressure, energy, and momentum equations. The electromagnetic equations, on the other hand, are purely diffusive, steady state equations, so they place no stability restrictions on the time step. Furthermore, the time dependence of the electromagnetic fields comes only from the coupling to the other equations through the electrical conductivity. As such, small changes in the pressure, energy, and velocity fields have only a negligible effect on the electromagnetic fields. As a result, there is a much looser accuracy restriction on the time step.

In light of the loose time step restriction on the electromagnetic equations, they are only solved every ten time steps. This was found to have no effect on the final result but decreases the computation time used for the electromagnetic equations by a factor of ten.

5.5. Parallelization

While many considerations have been given to numerical stability and computational efficiency in this chapter, the 3-D, transient nature, and complicated geometry of the problem make it prohibitively expensive to solve on a single processor. A solution on even a very course grid requires at least 400 hours. This makes parallelization of the code essential.

OpenFOAM uses the OpenMPI library to parallelize the sparse matrix solvers using domain decomposition. This was tested on the developed plasma solver and found to give near linear speedup, which is to say that parallelization to two processors requires half the run time, parallelization to four processors requires a quarter the run time, etc. Furthermore, no limit was found to the number of processors that can be utilized. Thus, the built in parallelization was used on all final runs using large clusters at the Minnesota Supercomputing Institute.

Chapter 6

Application to Plasma Arc Cutting

The mathematical model and numerical implementation presented in the previous chapters are quite valuable. The practical value of the model, however, is found in the application of this plasma solver to the plasma arc cutting process. In order to capture the physics of the plasma arc cutting process, a suitable geometry for the domain of interest is chosen and boundary conditions specified on the edges of this domain. The geometry must be chosen in such a way that it both includes the phenomenon of interest and the boundaries are located far enough away that they do not affect the results at the point of interest. The boundary conditions, in general, are a simplification of physical reality, but can be chosen in such a way that the plasma arc cutting process is still accurately described. Initial conditions are also prescribed, but the final result will be independent of the initial condition. Never the less, a reasonable initial condition is necessary in order to achieve numerical stability.

6.1. Geometry

Ultimately, the domain of interest is the interior of the kerf. It is impossible, however, to accurately describe the plasma jet at the top boundary of this region. Thus, it is necessary to extend the calculation domain upwards and include the interior of the nozzle. The nozzle geometry is that of a Hypertherm HPR 260 torch, extending up to the swirl ring. The outside front surface of the nozzle is assumed to be a flat surface, which is not technically true, but has little effect on the plasma flow inside the kerf. The ambient environment between the nozzle and the work piece extends 10mm from the torch axis, which is sufficiently far that the boundary does not affect the flow in the kerf. The shape of the kerf that extends into the work piece is taken from experimental measurements. The chosen domain then ends at the bottom of the kerf because the

present work is not concerned with the flow of plasma once it has exited the kerf. This geometry is shown in figure 6.1.

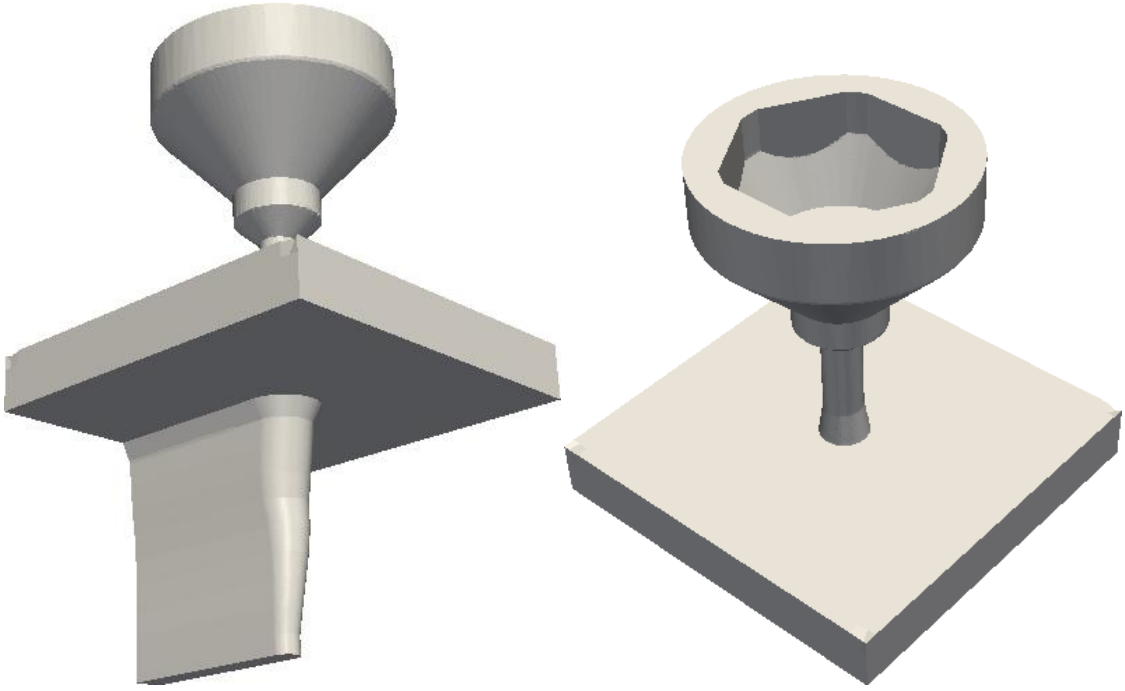

Figure 6.1. Geometry viewed from two different angles.

The shape of the kerf warrants particular attention because assumptions are used in order to produce a 3D geometry out of measured points. The kerf shape was measured by abruptly shutting off the torch at a precise time. The position of the torch axis relative to the work piece at shut off is then known. Thus, all kerf measurements are taken relative to the torch axis. Three measurements are taken, as indicated in figure 6.2, at a range of evenly spaced depths within the work piece. First the position of the left and right kerf walls relative to the torch axis are measured in a region of the kerf that is distant from the cutting front. These two measurements can be used to determine a total kerf width and a kerf centerline. It is important to note that the kerf centerline does not necessarily pass through the torch axis, although it might. The position of the kerf front is then measured as the distance from the torch axis along the kerf centerline.

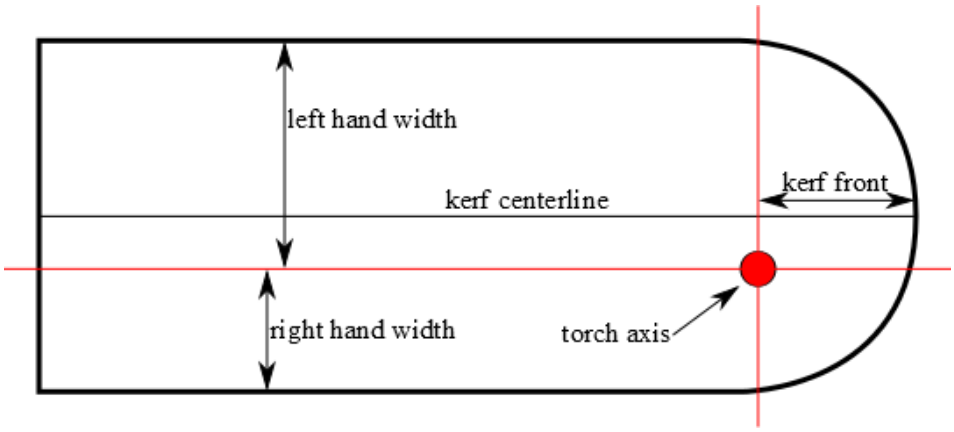

Figure 6.2. Position of kerf measurements at each depth.

It should be stressed that the kerf centerline as well as the three measurements will not be the same at each depth in the kerf. However, the measurements and the kerf centerline at each depth can be positioned relative to each other because the torch axis will be in the same global location at each depth. The measured shape of the kerf walls and the kerf front are given fig 6.3. The kerf is strongly asymmetric due to the swirl of the plasma flow. The kerf is also the widest at the top and narrows significantly at the bottom.

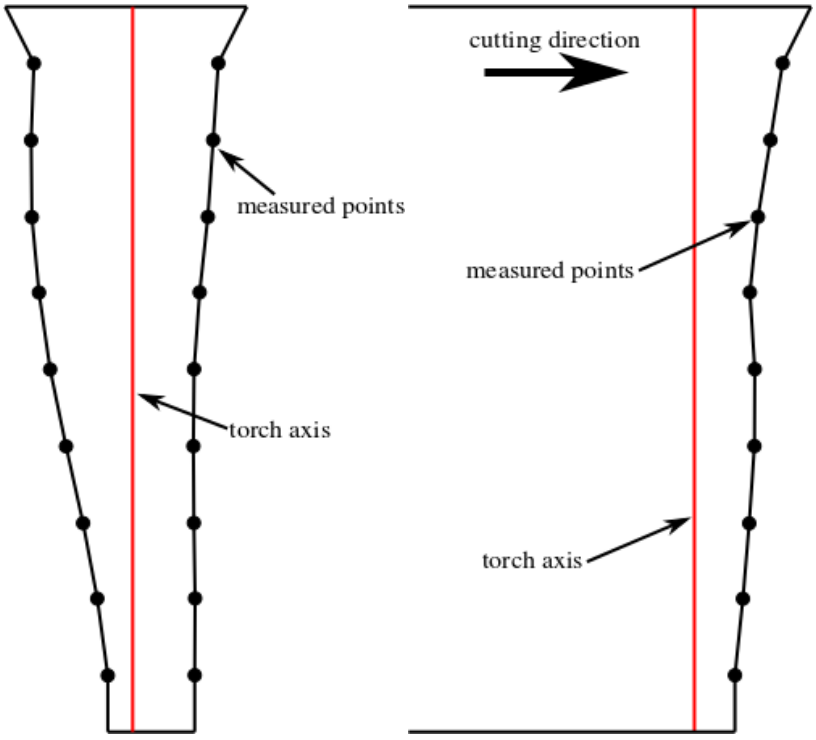

Figure 6.3. Measured kerf width, on left hand side, and kerf front, on right hand side.

In order to create a three dimensional kerf shape from these measurements, it is assumed that the kerf front takes the shape of a half circle that has a diameter equal to the kerf width. The center of this half circle is located on the kerf centerline one half kerf width behind the kerf front. When these assumptions are made at each depth within the kerf and positioned relative to each other using the torch axis location, a three dimensional kerf geometry is generated as shown in figure 6.4.

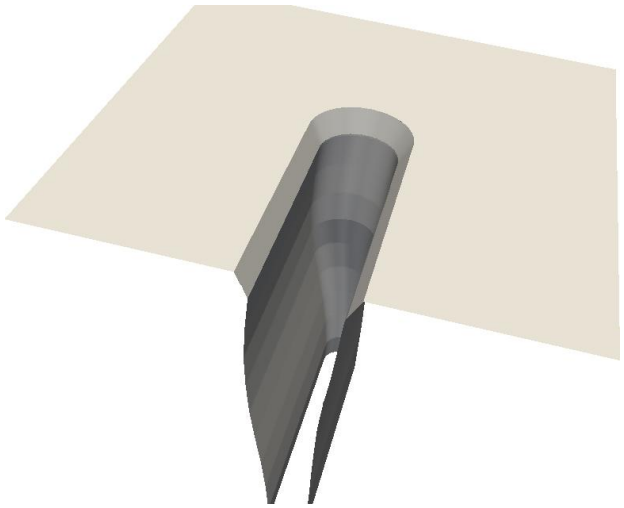

Figure 6.4. Three dimensional kerf shape

Once the geometry capturing the entire computational domain has been defined, it is necessary to generate a computational mesh that fits that geometry. A mesh made entirely of tetrahedral cells is easiest to fit to the irregular geometry, which makes it seem attractive. While OpenFOAM can handle any arbitrary cell shape, however, the numerical stability is far better for a mesh made of hexagonal cells. A compromise is found in the open source mesher, snappyHexMesh, that is bundled with OpenFOAM. This generates a mesh that is predominantly hexagonal cells with irregularly shaped tetrahedral or prismatic cells used to fit the mesh to the geometry at the boundaries. Additionally, localized cell refinement is used to provide more resolution in areas of interest and decrease compute time in areas that are not important.

6.2. Boundary Conditions

The correct assignment of appropriate boundary conditions is vital for the accurate description of the plasma arc cutting process. While the chosen boundary conditions are generally more simple than reality, they can be chosen in such a way that the model still accurately describes the physics present. Boundary conditions must be defined for velocity, pressure, temperature, electric potential, and magnetic potential.

6.2.1. Velocity

The velocity at the inlet assumes plug flow with a constant velocity that gives the correct total mass flow rate. This inlet velocity is also given a uniform swirl component defined by the angle θ where

$$\tan(\theta) = \frac{radial\ velocity\ component}{axial\ velocity\ component} \tag{6.1}$$

The "no-slip" assumption is then used across all nozzle and electrode walls, which states that the velocity adjacent to these surfaces is uniformly zero. The no-slip assumption is also used across the entire work piece boundary. This is not technically correct at the kerf front, where the flowing melt has a velocity in the range of 10-100 m/s. The melt flow velocity, however, is very low compared to the velocity of the plasma flow, so the no-slip assumption is nearly accurate. A zero gradient boundary condition is used on the outflow boundaries at the kerf bottom and surrounding ambient gas. This effectively determines the velocity on the boundary from inside the calculation domain. For the outlet at the back of the kerf, a wall is assumed and the no-slip boundary condition is used. This is certainly not accurate, but it greatly stabilizes the solution process and has no effect on the plasma flow in the front portion of the kerf. Thus, the results in the back of the kerf (which are uninteresting anyways) should be considered unphysical.

6.2.2. Pressure

At the solid boundaries, a zero gradient boundary condition is imposed on the pressure, this includes all of the nozzle surfaces, all of the work piece surfaces and the fictional wall on the back of the kerf. The outlets at the bottom of the kerf and the surrounding ambient will be at very nearly atmospheric pressure, which suggests imposing a constant value on the pressure. Such a boundary condition, however, is inadequate for compressible flow because pressure waves will "bounce" off a fixed value boundary condition, which is certainly not physically accurate. Instead, a "wave transmissive" boundary condition is included with OpenFOAM. This gives a

value that tends towards a fixed value but still maintains flexibility to allow pressure waves to pass through the boundary instead of reflecting. This wave transmissive boundary condition is used for the pressure at the outlet boundaries. The inlet pressure is simply set to a zero gradient, which determines the pressure at the boundary from the pressure inside the domain.

It is noteworthy that the total pressure drop through the torch is not specified in the boundary conditions. Rather, the inlet pressure will rise until the pressure drop is sufficient to drive the mass flow rate that is specified in the velocity boundary conditions. Alternatively, the inlet pressure, and hence the total pressure drop, could be specified instead of the mass flow rate. The inlet velocity would then take on a zero gradient boundary condition. In the actual operation of a cutting torch, however, the mass flow rate is set. Thus, in order to be consistent with physical reality, it is best to also set the mass flow rate in the model.

6.2.3. Temperature

Due to its proximity to the plasma, the nozzle may become quite hot. Through water cooling, however, it's temperature is maintained well below the melting temperature of copper. As such a fixed temperature of 500 K is imposed on the nozzle and cathode surfaces. This is not correct at the hafnium insert in the cathode, where the hafnium is molten. More likely, the hafnium temperature is approximately 3000 K. This difference, however, has no effect on the results of the model so the convenient uniform temperature of 500K is used instead. The inflow gas is approximately room temperature but a slightly higher temperature of 500 K is used for convenience. This has no effect on the results when compared to a boundary temperature of 300 K. On the work piece, a temperature of 1500K is used at the kerf front which approximately corresponds to the melting temperature of iron. A temperature of 1000K is imposed everywhere else on the work piece where it is assumed the metal is hot due to conductive heating, but not molten. At the outlets an "inlet/outlet" boundary condition is used. This boundary conditions imposes a constant value if the velocity is pointed into the domain and a zero gradient if the velocity is pointed out of the domain. In essence, this says that gas flowing out of the domain takes its temperature from the interior of the domain, but gas flowing into the domain is at room temperature.

The practice of fixing a constant temperature at solid walls is somewhat suspect. In reality, there are enormous temperature gradients near the walls. This leads to particles within one mean free path of the wall that are significantly hotter than the wall. In other words, the continuum assumption of section 3.1 breaks down next to the wall. A more accurate boundary

condition would involve some sort of "slip" assumption in which the plasma temperature next to the wall tends towards the wall temperature but does not actually reach it. The development of such a boundary condition, however, is beyond the scope of this work, so the fixed temperature boundary condition will be maintained. The simplification in the theory of the boundary condition likely introduces more error than the approximate nature of the wall temperature estimations. Thus, it would be a waste of effort to refine the estimations of wall temperature.

Under the two temperature approximation, the boundary conditions on the heavy species temperature are identical to the boundary conditions on the LTE temperature. The boundary conditions on the electron temperature, however, are different at solid walls. Because the electrons are orders of magnitude less massive than the atoms that make up the walls, the electrons are assumed to elastically scatter off the walls. Thus, the electrons impart no energy to the walls and a zero gradient is imposed at the solid walls. It is noted that a boundary condition accounting for the small transfer of electron energy was tested but had no affect on the results.

6.2.4. Electric Potential

The boundary conditions of the electric potential implicitly determine the boundary conditions of the current density. At the cathode, however, it is assumed that the current density is known, rather than the electric potential. Specifically, the current density is assumed to have a profile given by [77]

$$j(r) = j_o \exp\left(-\left(\frac{1.3r}{R}\right)^3\right) \tag{6.2}$$

where R is the radius of the hafnium and j_o is chosen so as to give the correct total arc current. Other profiles could be used, but they seem to have a negligible effect on the plasma flow in the kerf so they are not explored in this work. Using the assumed current density profile, the electric potential boundary condition on the cathode is set as

$$\frac{\partial \phi}{\partial \hat{n}} = \frac{j(r)}{\sigma} \tag{6.3}$$

The electric potential at the work piece is simply assigned a constant value of zero, which effectively states that the work piece is grounded. All remaining boundary conditions including the nozzle walls and the outlets are given a zero gradient boundary condition, which effectively states that they are electrically insulated and no current flows to them.

6.2.5. Magnetic Potential

The boundary conditions for the magnetic potential present a difficulty. In literature, a zero gradient boundary condition is commonly used, where one boundary is given a value of zero in order to fix the absolute value of the magnetic potential field. In the present work, however, this approach gave clearly unphysical results for the magnetic field. Thus, a fixed value condition on all boundaries was tested. This gave reasonable results with a magnetic field that curls around the path of the electrical current. The question of what value to use is then raised, but it can be found through vector calculus that the value does not matter:

Consider an arbitrary vector potential $\vec{A}$ such that

$$\vec{B} = \nabla \times \vec{A} \tag{6.4}$$

Assume also that $\vec{A} = 0$ on all boundaries of some domain. Consider now a vector field $\overrightarrow{A^*}$ that is the gradient of a scalar field C, where C is chosen to give $\overrightarrow{A^*}$ some arbitrary collection of values on the boundaries of the domain. Because C is the gradient of a scalar field, vector calculus relations state that [51]

$$\vec{B} = \nabla \times (\vec{A} + \overrightarrow{A^*}) \tag{6.5}$$

where $\left(\vec{A} + \overrightarrow{A^*}\right)$ has the arbitrary collection of values on the boundaries of the domain.

Thus, it is apparent that if the boundaries of the magnetic potential are fixed at some arbitrary values, it will give the same magnetic field as it would if the boundaries of the magnetic potential are fixed at zero. Because the value fixed on the boundaries of the magnetic field have no effect on the magnetic field, they are fixed at zero for convenience. This method of dealing with the magnetic potential has not been reported in literature anywhere, making it suspect. It provides the most reasonable results, however, so it is used in the present work.

6.3. Initial Conditions

Because the model is being run until it reaches a quasi-steady state, all of the initial conditions eventually wash out of the domain and they are not important for the accuracy of the model. The initial conditions are, however, very important for the stability of the solution. Because the physics to simulate arc initiation are not included in the model, the arc will simply not form if the gas is cold initially. Thus, the initial temperature must be high enough to support the electrical arc. This, however, gives rise to difficulties with the boundary conditions. Initially, cold walls in the nozzle rapidly cool the gas in the nozzle, causing it to contract and produce a

pressure lower than atmospheric pressure. This then causes reverse flow through the nozzle bore, pulling cooler atmospheric gas into the nozzle which is physically unreasonable and numerically unstable.

The difficulties with initial boundary conditions are solved by using "warm-up" boundary conditions. The entire domain, including the boundary conditions is initially at 10,000K. Over the first 100 milliseconds, the temperature of the boundaries is linearly ramped from 10,000K to the physically accurate boundary condition. This prevents the initial conditions from destabilizing the model while still giving physically accurate results after the initial conditions and warm up boundary conditions have washed out of the domain. To maximize the stability, the current density is also ramped from zero to the physically accurate value during the warm up period.

6.4. Iron Vapors

For simplicity, the model will initially be run with iron vapors neglected. In physical reality, however, there is likely a certain amount of iron vaporized from the work piece that enters the plasma. The amount and location of vaporization is unknown, which makes the problem of boundary conditions particularly tricky. The best way to model the vaporization would include the molten and solid portions of the work piece in the simulation domain so that the temperature of the work piece and the vaporization rate could be self consistently modeled. This, however, is clearly beyond the scope of the present work.

Somewhat simpler, the vaporization process can be resolved using "vapor pressure methods" [22]. This requires only that the temperature of the work piece be known. This is widely used in plasma arc welding models, where a temperature profile can be assumed for the work piece. Unfortunately, the calculation of the surface temperature is also beyond the scope of this thesis and a constant surface temperature is being assumed as described above. This constant surface temperature is certainly a very poor assumption for the purpose of introducing iron vapors because more vapor emission is expected in the region of the arc attachment, where heat fluxes are enormous. Thus, vapor pressure methods cannot be used.

In order to capture the distribution of vaporization across the face of the work piece, the vaporization is assumed to be proportional to the heat flux. This will effectively give large vaporization at the point of arc attachment, less across the rest of the front of the kerf, and almost none elsewhere. Thus, it will be assumed that 1% of the heat flux goes into vaporization of the metal and the remainder is conducted further into the work piece where it serves the purpose of melting the metal etc.

Chapter 7

Results

In the analysis of numerical simulation results, it is important to remember that simplifications have been made to the model, and thus, the model results will not exactly match physical reality. As such, the change in a numerical value (ex. total heat transfer to work piece) with respect to a change in modeling parameter is far more useful than the absolute numerical value itself. The absolute value will likely have a certain degree of error due to modeling assumptions. Because the assumptions are constant across all modeling results, the trends that emerge in the model results are probably quite accurate. That being said, it is still important for the absolute values of the results to have a certain degree of agreement with physical reality in order to verify that the assumptions made are valid and the model was implemented correctly.

7.1. Calculation of the Boundary Fluxes

One of the major goals in this work is to determine how the plasma interacts with the work piece. In order to do this, fluxes on the boundary must be calculated. The heat flux to the work piece is calculated as [78]

$$q'' = (\kappa_h + \kappa_{rh})\frac{\partial T_h}{\partial n} + j\phi_a + j\left(\frac{2k_b T_e}{e}\right) \tag{7.1}$$

where the first term on the right hand side is the familiar term for Fourier conduction. This is simply the heavy species thermal conductivity, $\kappa_h + \kappa_{rh}$, times the temperature gradient normal to the work piece. The second term accounts for the "condensation" of the electrons, in which the process of incorporating the electron into the solid anode releases a certain amount of energy. The work function, ϕ_a, is the amount of energy, in electron volts, released when incorporating a single electron into the work piece and j is the current density. The last term in the right hand side

describes the amount of electron energy that is carried into the anode by the electrons that are incorporated into the work piece. k_b is the boltzmann constant and e is the elementary charge.

There are several assumption implicit in this calculation of the heat flux. Most importantly the radiation heat flux is neglected, which is certainly a major mode of heat transfer in the plasma. It is likely, however, that the radiation is very diffuse and thus the radiation is fairly even across the face of the work piece. Thus, it can simply be assumed that the presently calculated heat flux is a low estimate but the distribution is accurate. It is also assumed that the electric current is carried entirely by the electrons. In actuality, a small portion of the current is carried by the ions. The ion portion of the current is very small, however, perhaps 1% of the total current, because the electron mobility is so much larger than the ion mobility. Thus the assumption that the electrons carry all current is satisfactory. Lastly, the voltage drop across the anode sheath is neglected. In actuality, a voltage change across the sheath accelerates the electrons due to sheath effects, which changes the heat flux slightly. This, however, is very small relative to the overall heat flux.

The thermal conductivity appearing in the heat flux calculation presents some particular difficulties. The temperature gradient is calculated using the temperature at the boundary and the temperature in the cell adjacent to the boundary. At first look, it would seem reasonable to take the thermal conductivity from either the boundary or this adjacent cell. If the thermal conductivity is taken from the boundary, however, it is fixed by the chosen boundary condition and is much too low of a value. Taking the thermal conductivity from the adjacent cell is just as problematic because the value varies widely depending on whether the cell temperature is above, below, or on the dissociation peak. A change in cell size can change the cell temperature, and thus the thermal conductivity, without actually changing the temperature gradient. This too is clearly unreasonable, so the thermal conductivity is obtained by integrating over the thermal conductivity between the boundary temperature and the adjacent cell temperature.

$$\kappa_h = \frac{1}{T_{cell} - T_{boundary}} \int_{T_{boundary}}^{T_{cell}} \kappa_h(T) dT \tag{7.2}$$

The drag force, or momentum flux, to the work piece is also of particular interest. The drag stress is calculated as

$$\sigma = \mu \frac{\partial u}{\partial n} \tag{7.3}$$

where μ is the viscosity and the gradient is the gradient in the normal direction of the velocity parallel to the boundary. The viscosity presents the same difficulty in equation 7.3 as the thermal

conductivity presents in equation 7.1. The same method of calculation shown in equation 7.2 is used for the viscosity.

7.2. Chosen Best two-temperature Result

The best choice of net emission coefficient, inelastic collision factor, and kerf offset will become apparent in the following sections. Here, it will be simply stated that it is best to use an effective radius of 1mm, an inelastic collision factor of 1000, and a kerf offset of .3mm. The distribution of temperature, velocity, and electrical current is best shown by taking a vertical slice through the domain parallel to the direction of cutting. This is shown in figure 7.1. The electron and heavy species temperatures look very similar with a peak temperature close to 35000K in the nozzle bore where the arc is most constricted. In contrast, the temperature profile immediately in front of the cathode is quite broad, which is caused by a recirculation flow in this region. The temperature maintains a high value outside of the nozzle although the profile begins to broaden. In the lower part of the kerf, where joule heating is no longer present, the temperature decreases rapidly. While the electron and heavy species temperature distributions look very similar, differences are evident in the fringes of the arc. In these fringes, the electron temperature is slightly higher, as expected. This effect is especially noticeable at the top edge of the kerf, where it is responsible for the behavior of the arc attachment.

The velocity is relatively low until it reaches the nozzle bore, where it accelerates dramatically. It reaches a peak velocity of over 10000 m/s as it exits the nozzle, but decelerates once it enters the kerf. This deceleration is caused both by the drag of the kerf walls as well as increasing density of the gas as it cools.

The electrical current density is very informative, explaining much of the behavior of the temperature field. The arc stretching between the cathode and the work piece is evident. The current density reaches its highest value inside the nozzle bore where it is forced to flow through a small cross sectional area, leading to immense Joule heating. This arc attaches to the kerf wall slightly below the top edge. The location of this attachment is influenced by the temperature field, where the temperature at the top edge of the kerf is low, giving a negligible electrical conductivity and forcing the arc down into the kerf to a point where the temperature is high enough to produce an electrical conductivity that can sustain the arc.

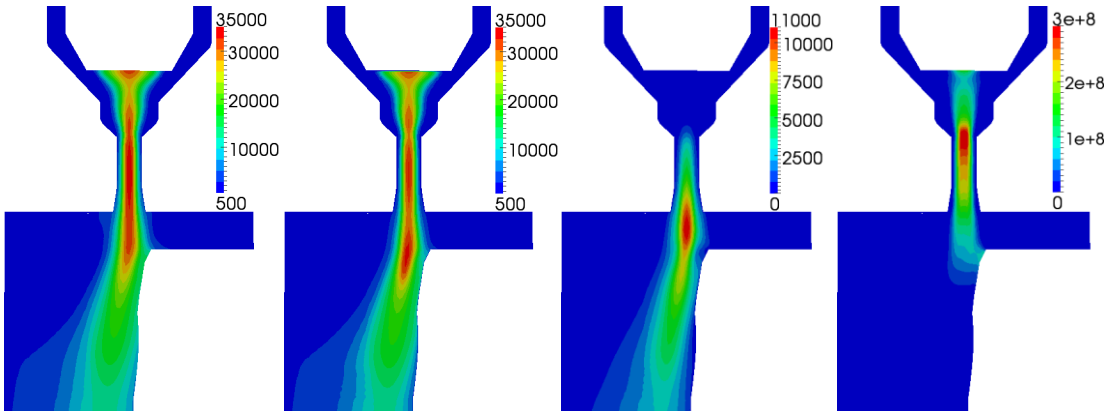

Figure 7.1. From left to right: electron temperature in (K), heavy species temperature (K), velocity (m/s), electrical current density (A/m^2).

The location and shape of the arc attachment, shown in figure 7.2, is of particular importance. This figure looks at the front kerf wall from the rear of the cut. A dominant, constricted attachment is apparent on the front of the kerf at a depth of about 1mm. There is also a separate smaller attachment on right hand side. This appears only on the right hand side due to the asymmetry of the kerf, where the right hand side is closer to the torch axis than the left hand side. The physical reality of two stationary, side by side attachments is suspect. If more than one attachment is present, they most likely are moving. As such, the attachment on the right hand side of the kerf is most likely an artifact of modeling assumptions. Specifically, it is probably caused by the approximate nature of the kerf shape, which is based on only a few measurements.

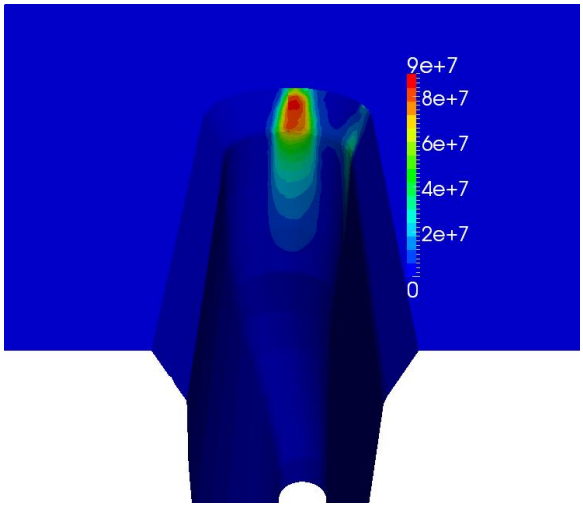

Figure 7.2. Electrical current density (A/m^2) along kerf face.

The heat flux distribution and drag force across the kerf face is of particular interest because it governs how the metal is melted and removed. These distributions are plotted in figure 7.3. As is expected, the heat flux has a peak value at the point of arc attachment. This is due to the electrons moving into the anode, both carrying enthalpy with them and releasing recombination energy. Additionally, the arc produces strong Joule heating all the way up to the wall, which raises the temperature near the wall, leaving only a thin thermal boundary layer, which conducts a lot of heat. The effect of the thinned boundary layer also produces a high conduction heat flux below that attachment for a distance until the thermally boundary layer can redevelop. The drag force does not show a peak at the point of attachment but there is a region of high drag immediately below the attachment. This is also due to the thinned boundary layer because the increased temperature near the wall leads to increased plasma viscosity, which exerts a higher drag force.

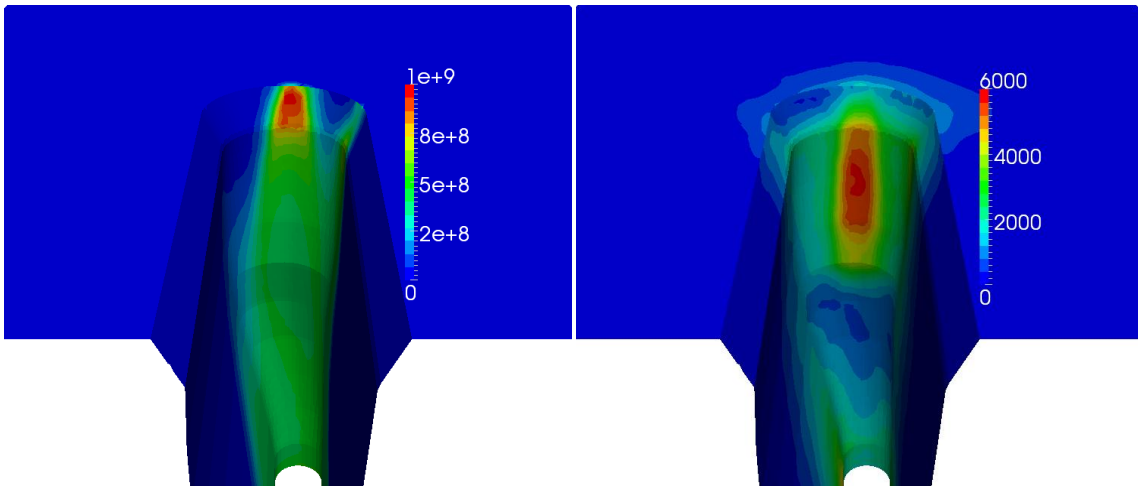

Figure 7.3. Heat flux (W/m^2) on left and drag force (N/m^2 on left across kerf face.

While figures 7.1-3 present the results as if they were in a steady state, this is not exactly true. In fact, there is a very slight oscillation in the result. The relative division of the total current flow between the front arc attachment and the right hand side arc attachment varies slightly in time, although the front attachment remains dominant. Because the right hand attachment is probably an artifact of modeling assumptions, this transient character is probably also an artifact of modeling assumptions.

7.2.1. Validation

The result most easily compared to experiment is the arc voltage. The arc voltage can be easily measured experimentally and was found to be 145 volts. The model gives an arc voltage of

153. The sheaths can have an effect of ~10 volts and it will be shown in section 7.4 that the radiation model can have a huge effect on the arc voltage. As such, the voltage is considered to be in reasonable agreement with experiments.

The distribution of velocity, temperature, and electrical current are difficult to compare to experiment because these are things that cannot be measured experimentally well. A lot of experimental work, however, has gone into locating the arc attachment, providing a source of validation. The present work most closely matches the work presented in [50]. Osterhouse et al. found a stationary attachment at a depth of between 1.5mm and 3.4mm for a similar cutting set up. The present modeling work has an approximately stationary attachment at a depth of 1mm, which is shallower. The present work neglects shield flow, however, which would normally serve to constrict the arc and drive the arc attachment deeper into the kerf. As such, the present work provides reasonable agreement with the experimental work in [50].

In current knowledge, there is no way to experimentally measure the heat flux distribution into the work piece. There are, also, only a few available calculations for the total transfer of energy to the work piece. In the present work, this heat flux will be validated by considering the following limiting case: The volume of metal removed per unit time is found from the cut speed and the area of the kerf. The minimum necessary energy transferred to the work piece must be the amount of energy needed to raise the given volume of metal from room temperature to melting point and then to melt that metal. This is given by the equation

$$\dot{Q}_{min} = \rho A U \left(\int_{T=300K}^{T=1811K} c_p dT + L \right) \tag{7.4}$$

where ρ is the density of the metal, A is the cross sectional area of the kerf, U is the cut speed, c_p is the specific heat of the metal, and L is the latent heat of melting the metal. For the present work, this gives a minimum energy transfer rate of approximately 23kW. The results presented here give a total energy transfer rate of 44kW. There is further energy transferred to the metal due to radiation effects and a significant amount of energy generated in the metal due to oxidation of the iron. As such, the results of the model give far more energy than the minimum required. This is physically very reasonable because some energy is lost in conduction to the solid metal and some energy is lost in super heating the molten metal before it is removed.

Similarly, the distribution of the drag force cannot be experimentally measured. An approximate minimum, however, can be found from [79]. Assuming the viscosity of the molten metal is negligible, the drag force needs only be sufficient to overcome the surface tension retaining the molten metal. This surface tension is given as

$$F_{surface\ tension} = \gamma D \tag{7.5}$$

where γ is the surface tension coefficient, which is a property of the molten metal, and D is the diameter of the kerf. From this, it can be calculated that the total drag force must be at least .0013 N/m^2. The modeling results give a total drag of .28 N/m^2. Thus, the drag is much greater than that needed to overcome surface tension, which is quite reasonable because the molten metal is accelerated dramatically out of the kerf.

7.3. LTE Results

A selection of results using the LTE formulation is shown here to demonstrate the inadequacies. The LTE model never actually settles to a steady state, but rather develops a strong instability in the nozzle which propagates unphysical results through the rest of the domain. A snap shot of the results at a particular time are shown in figure 7.4. Inside the nozzle, the arc bends dramatically to the left, which actually moves the arc to the left all the way down through the rest of the domain instead of producing an arc centered on the torch axis. As time progresses, the bend moves around the nozzle as the swirl flow pushes it. The physical reason for this would probably be the electro-magnetic kink instability. In an actual cutting process, however, this is certainly not happening because the arc bends so dramatically that it would melt the nozzle and lead to a very poor cut quality, which is not seen in the physical process.

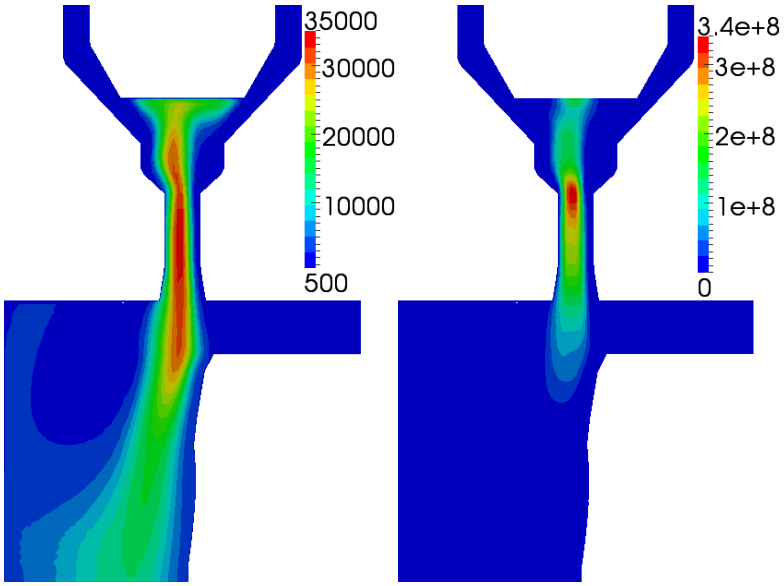

Figure 7.4. LTE temperature (K) on left and electrical current density (A/m^2) on right.

The off center character of the arc also produces a very unreasonable arc attachment, shown in figure 7.5. A large portion of the current flows through just a few cells on the top edge of the left side of the kerf. The remainder of the current flows through a very diffuse attachment as well as a small portion through the rim along the top front edge of the kerf. As the arc moves around in the nozzle due to the instability, this attachment wanders around the front and sides of the kerf.

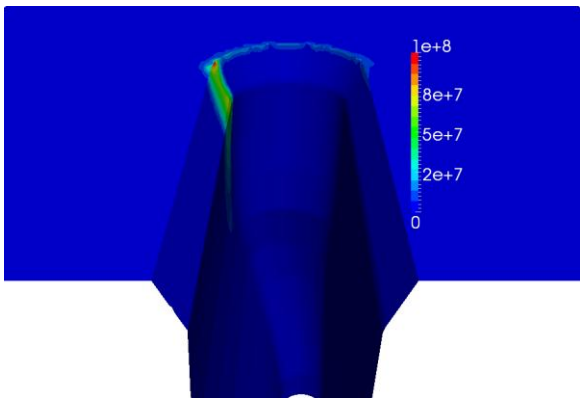

Figure 7.5. Arc attachment (A/m^2) for LTE model.

The results for the LTE model are clearly unphysical, but it is difficult to explain why. It may be due to numerical problems, but that is unlikely because the LTE formulation has been widely used as the more numerically stable option. More likely, constriction of the cold inflowing gas hitting the arc creates very steep gradients that develop a fluid dynamic instability. In the two temperature case, this is probably avoided because the thermal conductivity of the electrons is so high that the electron temperature profile is broadened.

7.4. Influence of Net Emission Coefficient

As explained in section 3.3.5, the net emission coefficient is overwhelmingly the most popular way of handling radiation in a plasma. In using this, however, it is necessary to choose an "effective radius", which characterizes the plasma. In a simple constricted arc, this would simply be the radius of the electric arc. For the complicated geometry in the present work, however, the radius of the arc is not constant and in the extinguishing plasma below the arc attachment, there is not even an arc to speak of. Assigning different effective radii to different locations in the model would be extremely complicated, negating the very reason for using the net emission coefficient.

As such, a single radius is used, and the model was run with an effective radius of 1mm and with an effective radius of 0mm (aka optically thin) to capture the influence of the effective radius.

The results for an effective radius of 1mm are those given in section 7.2. For the optically thin case, the results seemed to be approaching a steady state but then develop a fluid dynamic instability in the nozzle that is similar to the instability in the LTE case in section 7.3. The results as they first appear to approach steady state are shown in figure 7.6. The overall character is similar to the case with an effective radius of 1mm, but the peak temperatures are lower because more heat is lost through radiation. The lower temperature results in a lower electrical conductivity and thus a much higher arc voltage of 171V. This deviates significantly from the experimentally measured arc voltage, indicating that an effective radius of 1mm is much closer to physical reality. The dramatic change in voltage illustrates the influence the radiation model has on the arc voltage, giving a fairly large uncertainty in the absolute value of the arc voltage produced by the model.

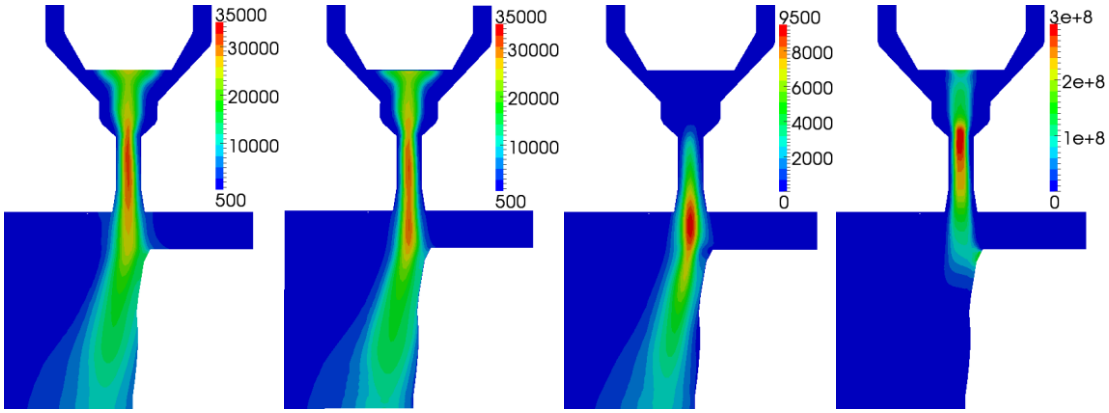

Figure 7.6. From left to right: electron temperature (K), heavy species temperature (K), velocity (m/s), electrical current density (A/m^2).

7.5. Influence of Inelastic Collision Factor

Section 3.3.3 briefly discussed an inelastic collision factor which appears in the energy term governing the transfer of enthalpy between electrons and heavy species. Collisions between electrons and atoms are very nearly elastic, so in these cases the inelastic collision factor is simply one. The collision between an electron and a molecule, however, is fundamentally inelastic because significant energy is transferred to rotational and vibrational modes of energy in the molecule. Unfortunately, the details of these inelastic collisions are poorly understood. No publication of an inelastic collision factor for oxygen molecules was found in literature. Megli et

al. [80] present the most thorough approach to this factor in a study of a Hydrogen-Nitrogen arc jet thruster. Megli et al. recognize that little data is available and the available data has a huge uncertainty. As such, they did a parametric study with their numerical model where a range of inelastic collision factors is tested and the results compared with experiment. The most reasonable results were then assumed to have the correct value of inelastic collision factor. For their study, Megli et al. tested inelastic collision factors of 30, 300, and 3000 and found 3000 to give the most reasonable result. In the present work, inelastic collision factors of 10, 100, and 1000 were tested.

The results of the velocity and heavy species temperature are nearly identical for varying inelastic collision factor. There is, however, a noticeable difference in the electron temperature, shown in figure 7.7. As the inelastic collision factor increases, the electron temperature in the fringes decreases. This is to be expected because molecules and electrons are present together only in the fringes of the arc. In this region, the increased inelastic collision factor will more rapidly equilibrate the electron and heavy species temperature, which effectively reduces the electron temperature because the specific heat of the heavy species is much higher in this temperature range.

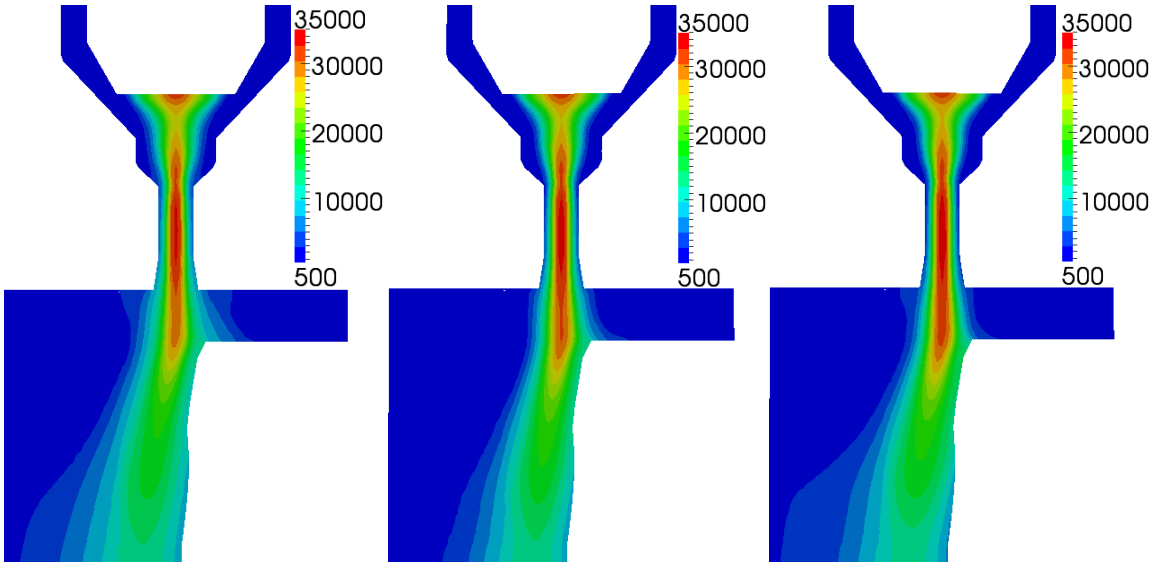

Figure 7.7. Electron temperature (K) for varying inelastic collision factor. From left to right, inelastic collision factor for electron/molecular collisions is: 10, 100, 1000.

This reduction of the electron temperature in the fringes has a significant effect on the arc attachment because the character of the attachment is determined by how it crosses the thermal boundary layer next to the kerf wall. The effect of the inelastic collision factor on the arc

attachment is shown in figure 7.8. As the inelastic collision factor increases and the electron temperature in the fringes of the arc decreases, the arc attachment becomes more constricted and moves deeper into kerf. For an inelastic collision factor of 10, the electrical conductivity is sufficiently high along the kerf face that the arc simply follows the shortest path to the top edge of the kerf. For an inelastic collision factor of 1000, however, a layer of lower electrical conductivity is present across the kerf face and the arc must bridge across this in a small area, giving the constricted attachment.

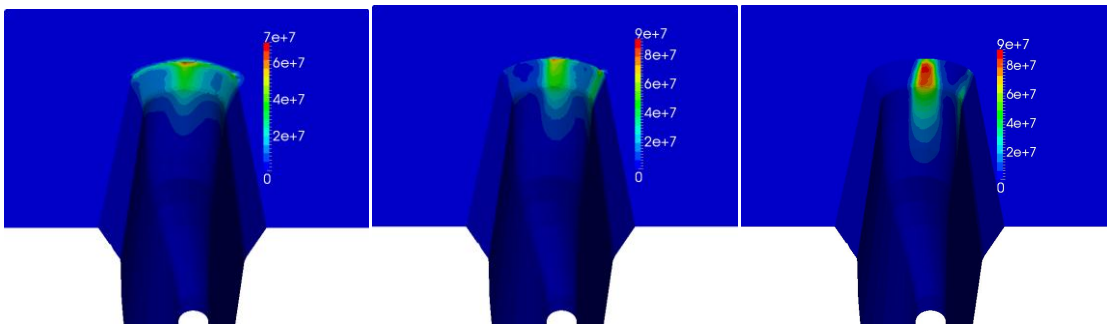

Figure 7.8. Arc attachment location (A/m^2) for varying inelastic collision factor. From left to right, inelastic collision factor for electron molecular collision is: 10, 100, 1000.

An inelastic collision factor of 1000 seems to give the most reasonable result, and so, was used for this work. It should be noted, however, that this is still a fairly broad approximation. In reality, this factor is a function of both electron and heavy species temperatures. A full understanding of this factor, however, would require a detailed gas kinetics study that is far beyond the scope of the present work. It is sufficient here to observe that the results obtained with the single value approximation are reasonable, showing that the approximation is valid.

7.6. Influence of Kerf Position Shift

The geometry of the kerf was experimentally measured very carefully. The need for a shifted geometry becomes apparent when the model is run with this originally measured kerf geometry. The arc attachment, shown in figure 7.9, is clearly unphysical. While the expected attachment on the front of the kerf is present, there is a second and more dominant attachment on the right hand side of the kerf. Such an arrangement would lead to excessive heat transfer on the right hand side, resulting in enhanced melting that would produce a different kerf shape. As with the attachment presented in section 7.2, there is a slight variation in time, with the relative

strength of the two attachments changing slightly. At all times, however, the right hand attachment remains dominant.

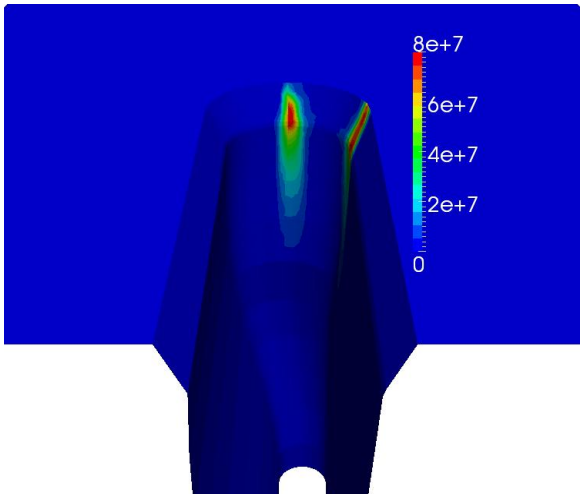

Figure 7.9. Arc attachment (A/m^2) with no kerf offset.

Because of the asymmetry of the kerf, the right hand side of the kerf is closest to the torch axis. Noting that the arc follows the path of least resistance, it becomes apparent that the right hand attachment appears because that kerf wall is so close. Because an attachment on the front of the kerf is physically more reasonable, it is concluded that the kerf must be shifted so that the kerf front is closer to the torch axis. While this seems at first to be an arbitrary change to the model, it can be grounded in physical reality because there is some uncertainty in the measured kerf shape due to the presence or absence of a layer of molten metal. During the cutting process, there is certainly a layer of molten metal on the kerf front. When the torch is abruptly shut off, however, it is unclear whether this molten layer solidifies in place or is removed before kerf measurements are taken. If this layer is removed, than the measured kerf shape after cooling will be slightly different than the kerf shape during the cut process and the kerf front will, in fact, be closer to the torch axis during the actual cutting process.

While it is reasonable to assume a kerf shift, it is not immediately evident how much the kerf should be shifted. For this reason, three displacements for the shift are tested: .2mm, .3mm, and .4mm. The relationship between the kerf shift and the results can then be established and a "best" value chosen. The arc attachment for each shift is shown in figure 7.10. The result for .3mm is the same as that shown in section 7.2 with a dominant attachment on the front of the kerf and a smaller, probably unphysical attachment, on the right hand side. There is also a slight fluctuation in time with the front attachment remaining dominant. At first look, a shift of .2mm

seems to give a better result, with a more minor right hand side attachment. For this case, however, the fluctuation in time is quite large, with the entirety of the current flowing through the right hand side attachment at times. A shift of .4mm gives somewhat bizarre results with strong fluctuations of the arc attachment between one on the left hand side, one on the right hand side and one on the front. The moment captured in figure 7.10 has the particularly odd arrangement in which the attachment is present on both sides but not the front.

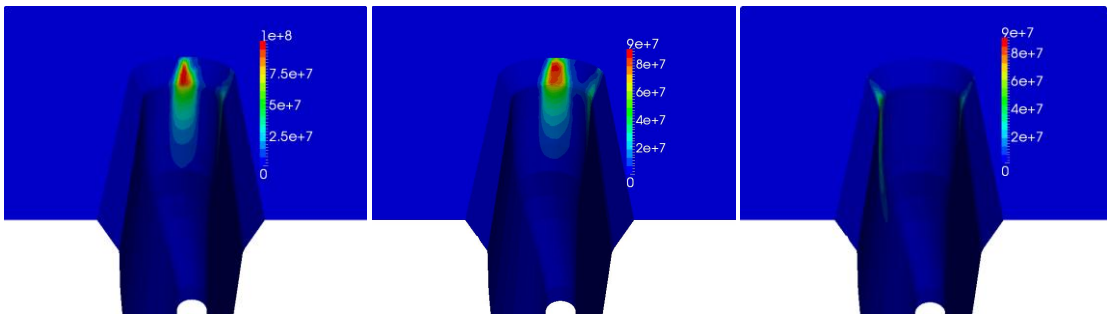

Figure 7.10. Arc attachment (A/m^2) for varying kerf offsets of, from left to right: .2mm, .3mm, and .4mm.

In light of the assumption that a single attachment on the kerf front is most physically reasonable, a kerf offset of .3mm gives the best result. As such, it is probably the closest to physical reality.

7.7. Mesh Dependency

All results in sections 7.1-7.6 where calculated using a mesh consisting of ~121000 cells. These required about 36 hours to run when parallelized to 64 cores. For the chosen "best" set of parameters given in section 7.1, a much finer grid of ~ 375000 cells was also used, where the vast majority of the cells were added in the region occupied by the electrical arc. This was run on 4 cores for longer than a month. The effects of this mesh refinement are rather significant. This is shown for the arc attachment in figure 7.11, where the general behavior is the same with a dominant constricted attachment on the front of the kerf and a minor second attachment on the right hands side. The attachment for the fine mesh, however, is more constricted and slightly lower in the kerf.

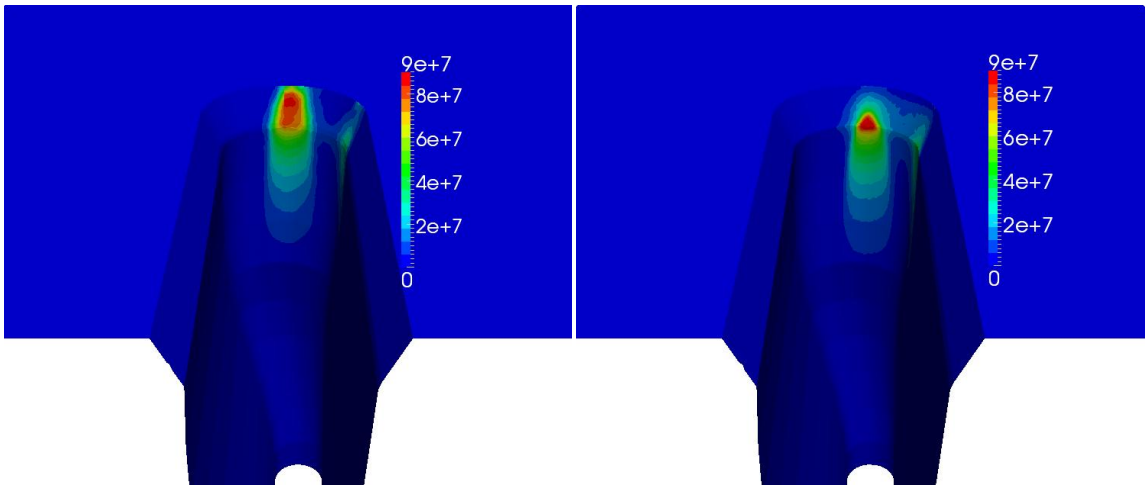

Figure 7.11. Arc attachment (A/m^2) with 121000 cell mesh on left and 375000 cell mesh on right.

The changing position of the arc attachment deeper in the kerf for the fine mesh is further elucidated by looking at the temperature distribution, shown in figure 7.12 and 7.13. The high temperature path of the electric arc is narrower when the finer mesh is used. This causes a slightly higher peak temperature in the nozzle bore where narrowing of the current carrying path results in slightly more Joule heating. At the top front edge of the kerf, the narrowing of the high temperature path allows a cold boundary to extend deeper into the kerf. The arc cannot cross this cold layer, which explains why the arc attachment is deeper in the kerf for the finer mesh.

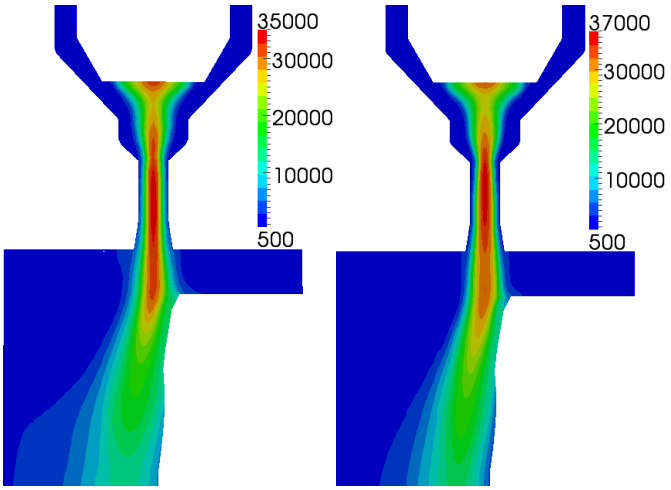

Figure 7.12. Electron temperature (K) distribution for 121000 cell mesh on left and 375000 cell mesh on right.

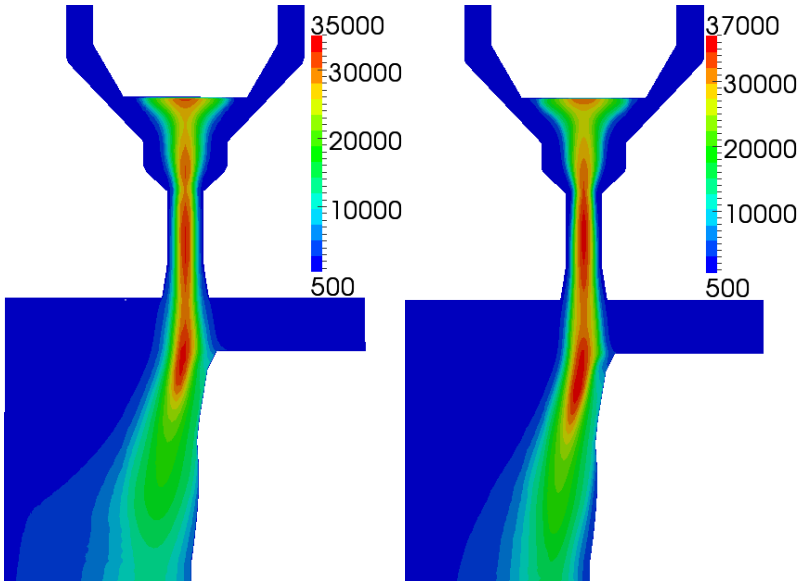

Figure 7.13. Heavy species temperature (K) for 121000 cell mesh on left and 375000 cell mesh on right.

There is also a change in the arc voltage with a value of 141V for the finer mesh compared to 153V for the courser mesh. This is likely caused by the increased peak temperature, which increases the electrical conductivity, reducing the voltage necessary to drive the current flow. This is not, however, a reason for concern as the experimental value of 145 V falls between these two values.

The most dramatic effect of the finer mesh is found in the heat flux, shown in figure 7.14. The overall distribution is similar, with the highest heat flux at the location of arc attachment and further enhanced heat flux below the attachment, where the thermal boundary layer is very thin. The magnitudes however, are quite different with a the course grid having a peak heat flux of ~1e9 W/m^2 and the fine grid having a peak heat flux of ~ 1.4e9 W/m^2. This difference is also evident in the total heat transfer with a heat transfer of 46kW for the course grid and a heat transfer of 69kW for the fine grid.

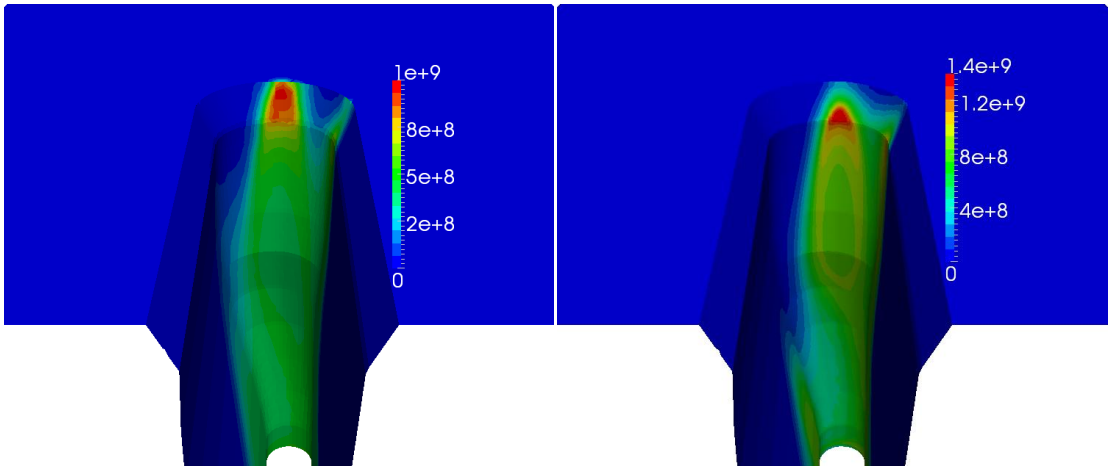

Figure 7.14. Heat flux for (W/m^2) a 121000 cell mesh on left and a 375000 cell mesh on right.

7.8. Influence of Iron Vapors

In the real cutting process, there is most likely some iron vapor present in the kerf that has been emitted from the melt. This effect is investigated for the parameters chosen in section 7.2. This was done by imposing a mass inflow of iron vapor along the kerf face that assumes 1% of the calculated heat flux was utilized in vaporizing the metal. While this is a rather general approximation, it effectively captures the phenomenon in which the most iron vapor is emitted where the highest heat flux is. As such, this method will give a good understanding of what influence the iron vapor will have.

The mole fraction of iron vapor is shown in figure 7.15. A thin layer of iron vapor appears on the front face of the kerf beginning at the point of attachment, where the heat flux vaporizes a significant amount of iron. This layer becomes thicker and more pronounced as it moves downstream, where both more iron vapor is introduced and the vapor present diffuses away from the kerf wall

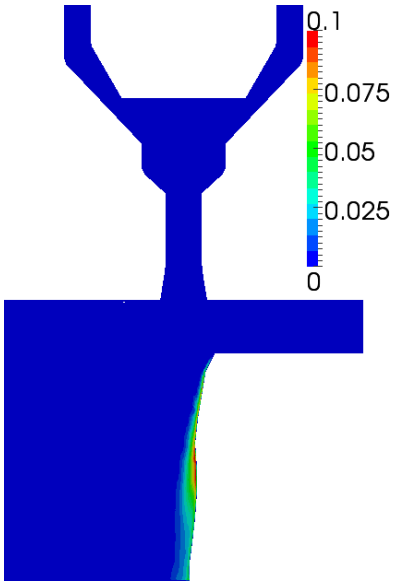

Figure 7.15. Mole fraction of iron vapor

The inclusion of iron vapor was found to have a negligible effect on the distribution of temperature, velocity, and current density, as well as having a negligible effect on the drag force and arc voltage. The effect on the heat flux, however, is dramatic. This is shown in figure 7.16, where the decrease in heat flux at the point of the attachment is not overlay large but the decrease in heat flux down steam is very significant. This is also reflected in the overall heat transfer which is 46 kW when iron vapor is neglected and 28 kW when iron vapor is included. This decrease in heat transfer is explained by the heavy species reactive thermal conductivity. Pure oxygen has dramatic, narrow peak in thermal conductivity around 3000K due to the dissociation reaction of the oxygen molecule. This is the temperature range of interest next to the kerf wall, where the heat flux is determined and thus contributes a lot to the heat transfer. Iron, however, does not have this peak in the heavy species reactive thermal conductivity and thus, when it is present, reduces the thermal conductivity resulting in a lower heat transfer rate. In other words, a large portion of the heat flux comes from the chemical reaction of oxygen molecules recombining. When iron vapor is present, the oxygen species are displaced, reducing the heat flux to the wall due to these reactions.

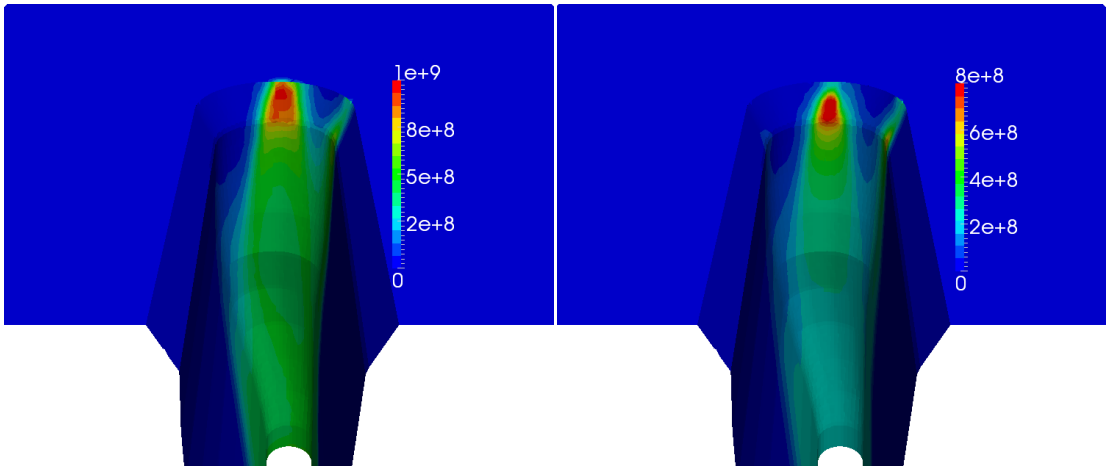

Figure 7.16. Heat flux (W/m^2) for pure oxygen case on left and iron vapor included on right.

Chapter 8

Summary, Conclusions, and Topics for Further Research

8.1. Summary

Plasma arc cutting is the best way to cut sheet metal when high output and high cut quality is a priority. There is, however, always an interest in improving the both the cut speed and the cut quality even further. Much work has been done around the design of the cutting torch itself because it is the part that can be directly controlled. Less work has been done understanding the physical phenomena around the work piece and the interaction of the plasma with that work piece. In order to further improve the plasma cutting process, it is necessary to study the anode region of the process in depth.

This thesis begins to fill the gap in knowledge of the physics of the work piece region in plasma arc cutting. Because of the narrow kerf geometry, high temperatures, and strong plasma radiation, this is very difficult to study experimentally, and the path of numerical modeling was chosen instead. The scope of the problem was narrowed to included only the flow of the plasma through the kerf and the resulting heat flux and drag force to the work piece. This model was solved as a 3D, transient problem using two separate plasma models. The first was the common local thermodynamic equilibrium (LTE) model that describes the plasma with a single temperature. The second was the more complicated two temperature model that allows for a separate electron temperature describing the energy of the electrons. Furthermore, the diffusion of iron vapors into the plasma from the work piece was considered.

A major component of the plasma model consisted of calculating the thermodynamic and transport properties. First the equilibrium chemical composition was calculated by solving a set of

mass action equations, along with Dalton's law and the quasi-neutrality assumption. This equilibrium chemical composition was then used, along with statistical mechanics, to calculate the thermodynamic properties, where it is noted that a number of different partial derivatives took the place of specific heat in the two-temperature plasma model. The transport properties were calculated using the Chapman-Enskog method, which presented particular difficulties because there is no clear consensus in the literature on the correct equations and correct collision integrals. While emphasis was given to convenience rather than correctness, reasonable agreement was found with published literature where it was available. The O_2^+ ion was included in the property calculations, which is a significant advancement not found in literature, but is necessary in order to obtain accurate two-temperature results.

The model was implemented in the general purpose, open source CFD package, OpenFOAM. This allowed the plasma model to be accurately implemented while maintaining the robustness and portability of a general purpose code. Thus, while the code was applied to plasma arc cutting in the present work, it could be easily applied to any other plasma process in the future.

The developed model was applied to a plasma arc cutting geometry that extended all the way from the inside of the nozzle to the bottom of the kerf. This model produced very reasonable looking results as well as a heat transfer rate, drag force, and arc voltage that compared well with experimental values. This gives a high level of confidence that the model does in fact capture the physics present in the plasma arc cutting process.

The model was run for a pure oxygen LTE case, a pure oxygen two-temperature case, and a oxygen iron mixture two-temperature case. For the pure oxygen two-temperature case, three parameters related to the physics of the plasma where investigated: 1) choice of net emission coefficient effective radius, 2) value of inelastic collision factor, and 3) kerf position offset in the direction of cutting. The "best" values for these parameter were then chosen by comparing the results to experiments. The influence of the computation mesh size was also investigated.

8.2. Conclusions

The results of the LTE simulation were disappointing, with an odd fluid dynamic instability developing in the nozzle, which then propagated down to the work piece to give an unreasonable arc attachment. This fluid dynamic instability also appeared in the case were an optically thin radiation model was used. This is potentially a real physical instability that is

related to the electro-magnetic "kink" instability, where a bend in an arc tends to bend further. In the true process, however, such an arc configuration would melt the nozzle, and thus, cannot be accurate.

The results of the two-temperature simulation were excellent and in reasonable agreement with physical experiments where ever experiments could be made. The heat flux was found to have a peak at the point of attachment, where both joule heating thinned the boundary layer and anode effects contributed significantly. The heat flux was also quite high immediately below the attachment, where the thermal boundary layer was still thin. Further down, the heat flux decreased as both the plasma cooled and the boundary layer became more developed. The drag on the kerf face was also greater below the attachment because the thermal boundary layer was thinner and a high temperature plasma has a high viscosity, allowing it to exert more force on the kerf face.

A net emission coefficient with an effective radius of 1mm was found to be most reasonable as the optically thin case developed the fluid dynamic instability mentioned for the LTE case above. Furthermore, the optically thin case produced an arc voltage that was unreasonably higher than the experimentally measured value. The choice of 1mm can also be justified by physical reasoning, because the arc radius is, in fact, close to 1mm through much of the domain.

An inelastic collision factor of 1000 was found to give the best results. Lower values for the factor led to a higher electron temperature in the arc fringes. This higher electron temperature led to a very diffuse anode attachment. Experimental imaging indicates that the attachment is constricted, so the diffuse attachment produced by lower values of the inelastic collision factor is clearly unreasonable.

It is necessary in the model to offset the kerf slightly from the measured shape in order to account for the molten metal that is in the kerf during cutting, but which is removed before measurement. A kerf offset of .3mm was found to be most reasonable. A smaller offset produced a more dominant attachment on the side of the kerf instead of the front of the kerf. A larger offset was found to produce an attachment wandered wildly about the kerf, which is also unphysical.

The inclusion of iron vapors was expected to have a significant effect on the arc attachment. Because of the high velocities present, however, the layer of iron vapor remained very thin and had almost no influence on any result except the heat flux, which was significantly reduced.

8.3. Topics for Further Research

8.3.1. Turbulence

Turbulent effects have been neglected in the present work. This may be reasonable in the nozzle and in the kerf where the narrow geometry and increased viscosity of the plasma reduce turbulent effects. In the space between the nozzle and the work piece, however, there is a plasma jet flowing into ambient, stationary air. This certainly has turbulent effects in which the ambient air is entrained into the plasma jet. This turbulence will serve to broaden the temperature and velocity profiles and reduce the peak values. It is uncertain what effect turbulence would have on the heat flux and drag force. On the one hand, the broadening of the temperature and velocity profile could result in momentum and enthalpy being spread across the top of the work piece instead of entering the kerf. On the other hand, turbulent boundary layers are generally thinner, which would increase heat and momentum transfer to the kerf walls.

8.3.2. Mesh dependence and sheath effects

Ideally, computational fluid dynamic results should be independent of mesh. Section 7.7 explored this somewhat and found the results in much of the domain to be mesh independent. The heat flux, however, was found to vary strongly with cell size. This variation has to do with having insufficient mesh density to fully resolving the temperature profile in the boundary layer. At first glance, it would seem obvious that this problem can be alleviated by simply refining the mesh along the kerf face. At a certain point, however, this becomes less accurate rather than more accurate. The present work neglects sheath effects, which is fine so long as the mesh next to the anode is not too fine. If, however, the mesh is too fine, then the quasi-neutrality and continuity assumptions will not no longer be valid. Thus, in order to obtain a heat flux that is truly mesh independent, it would be necessary to included some sort of sheath model.

8.3.3. Kerf shape

In the present work, there are a large number of assumptions that go into generating the kerf shape. The presences of a secondary arc attachment on the side of the kerf is probably an artifact of these assumptions. A better characterized kerf shape would lead to a more physically accurate result.

8.3.4. Melting and flow of molten metal

While the present work has only modeled the flow of plasma in the kerf, it would be extremely valuable to included the work piece itself into the computational domain. This would have to include the flow of heat into the work piece, the melting of the metal and then the flow and removal of that molten metal. This would not only side step all the problems with kerf shape, it would capture the cutting process itself instead of just the flow of plasma. It would generate its own kerf shape, which could be compared with experiments and used to study why a particular plasma flow generates a particular kerf shape.

Bibliography

1. http://www.openfoam.com/docs/user/. *OpenFOAM User Guide*. 08/26/2011].
2. Patankar, S.V., *Numerical Heat Transfer and Fluid Flow*. 1980, New York: Taylor & Francis Group.
3. Issa, R.I., *Solution of the Implicitly Discretised Fluid Flow Equations by Operator-Splitting.* Journal of Computational Physics, 1985. **62**: p. 40-65.
4. Devoto, R.S., *Transport Properties of Ionized Monatomic Gases.* The Physics of Fluids, 1966. **9**(6): p. 1230-1240.
5. Devoto, R.S., *Simplified Expressions for the Transport Properties of Ionized Monatomic Gases.* The Physics of Fluids, 1967. **10**(10): p. 2105-2112.
6. Devoto, R.S., *Transport Coefficients of Partially Ionized Argon.* The Physics of Fluids, 1967. **10**(2): p. 354-364.
7. Hsu, K.C., K. Etemadi, and E. Pfender, *Study of the free-burning high-intensity argon arc.* J. Appl. Phys., 1983. **54**(3): p. 1293-1301.
8. Murphy, A.B., et al., *Advanced Thermal Plasma Modelling.* High Temperature Material Processes, 2008. **12**: p. 255-336.
9. Trelles, J.P., et al., *Arc Plasma Torch Modeling.* Journal of Thermal Spray Technology, 2009. **18**(5-6): p. 728-752.
10. Trelles, J.P., J.V.R. Heberlein, and E. Pfender, *The Reattachment Process in Nonequilibrium Arc Simulations.* IEEE Transactions on Plasma Science, 2008. **36**(4): p. 1024-1025.
11. Trelles, J.P., J.V.R. Heberlein, and E. Pfender, *Non-equilibrium Modelling of Arc Plasma Torches.* J. Phys. D: Appl. Phys., 2007. **40**: p. 5937-5952.
12. Trelles, J.P., E. Pfender, and J.V.R. Heberlein, *Modelling of the Arc Reattachment Process in Plasma Torches.* J. Phys. D: Appl. Phys., 2007. **40**: p. 5635-5648.
13. Trelles, J.P. and J.V.R. Heberlein, *Simulation Results of Arc Behavior in Different Plasma Spray Torches.* Journal of Thermal Spray Technology, 2006. **15**(4): p. 563-569.
14. Trelles, J.P., E. Pfender, and J.V.R. Heberlein, *Multiscale Finite Element Modeling or Arc Dynamics in a DC Plasma Torch.* Plasma Chem Plasma Process, 2006. **26**: p. 557-575.
15. Hsu, K.C. and E. Pfender, *Two-temperature modeling of the free burning, high-intensity arc.* J. Appl. Phys., 1983. **54**(8): p. 4359-4366.
16. Freton, P., et al., *Energy Equation Formulations for Two-Temperature Modelling of 'Thermal' Plasmas.* J. Phys. D: Appl. Phys., 2012. **45**: p. 1-22.
17. Ramshaw, J.D. and C.H. Chang, *Computational Fluid Dynamics Modeling of Multicomponent Thermal Plasmas.* Plasma Chem Plasma Process, 1992. **12**(3): p. 299-325.
18. Ramshaw, J.D., *Self-Consistent Effective Binary Diffusion in Multicomponent Gas Mixtures.* J. Non-Equilib. Thermodyn., 1990. **15**: p. 295-300.
19. Haidar, J., *Non-Equilibrium Modelling of Transferred Arcs.* J. Phys. D: Appl. Phys., 1999. **32**: p. 263-272.
20. Murphy, A.B., *Diffusion in equilibrium mixtures of ionized gases.* Physical Review E, 1993. **48**(5): p. 3594-3603.
21. Murphy, A.B., *Thermal Plasmas in Gas Mixtures.* J. Phys. D: Appl. Phys., 2001. **34**: p. R151-R173.
22. Murphy, A.B., *The Effects of Metal Vapour in Arc Welding.* J. Phys. D: Appl. Phys., 2010. **43**: p. 1-31.

23. Gleizes, A., J.J. Gonzalez, and P. Freton, *Thermal Plasma Modelling.* J. Phys. D: Appl. Phys., 2005. **38**: p. R153-R183.
24. Lowke, J.J. and M. Tanaka, *'LTE-Diffusion Approximation' for Arc Calculations.* J. Phys. D: Appl. Phys., 2006. **39**: p. 3634-3643.
25. Gage, R.M., *Patent No. 2806124*. 1957: USA.
26. Severance, W.S. and D.G. Anderson, *How Plasma Arc Cutting Gases Affect Productivity.* Welding Journal, 1984(Febuary): p. 35-39.
27. Sasse, F.H., *Oxygen Plasma Process Increases Quality in Cutting Carbon Steel.* Welding Journal, 1991(February): p. 64-66.
28. Manohar, M. and J.P. Snyder II, *Dross formation during plasma arc cutting of steels.* Welding Journal, 1994(November): p. 45-51.
29. Nemchinsky, V.A., *Dross formation and heat transfer during plasma arc cutting.* J. Phys. D: Appl. Phys., 1997. **30**: p. 2566-2572.
30. Ramakrishnan, S., *Properties of electric arc plasma for metal cutting.* J. Phys. D: Appl. Phys., 1996. **30**: p. 636-644.
31. Ramakrishnan, S., et al., *Plasma Generation for the Plasma Cutting Process.* IEEE Transactions on Plasma Science, 1997. **25**(5): p. 937-946.
32. Nemchinsky, V.A., *Plasma flow in a nozzle during plasma arc cutting.* J. Phys. D: Appl. Phys., 1998. **31**: p. 3102-3107.
33. Gonzalez-Aguilar, J., et al., *A Theoretical Study of a Cutting Air Plasma Torch.* IEEE Transactions on Plasma Science, 1999. **21**(1): p. 264-271.
34. Freton, P., et al., *Complementary experimental and theoretical approaches to the determination of the plasma characteristics in a cutting plasma torch.* J. Phys. D: Appl. Phys., 2003. **36**: p. 1269-1283.
35. Freton, P., et al., *Numerical and experimental study of a plasma cutting torch.* J. Phys. D: Appl. Phys., 2002. **35**: p. 115-131.
36. Ghorui, S., J.V.R. Heberlein, and E. Pfender, *Non-equilibrium modelling of an oxygen-plasma cutting torch.* J. Phys. D: Appl. Phys., 2007. **40**: p. 1966-1976.
37. Colombo, V., et al., *Understanding Plasma Fluid Dynamics Inside Plasma Torches Through Advanced Modeling.* IEEE Transactions on Plasma Science, 2008. **36**(2): p. 389-402.
38. Pardo, C., et al., *Spectroscopic analysis of an air plasma cutting torch.* J. Phys. D: Appl. Phys., 1999. **32**: p. 2181-2189.
39. Peters, J., et al., *Relating Spectroscopic Measurements in a Plasma Cutting Torch to Cutting Performance.* Plasma Chem Plasma Process, 2008. **28**: p. 331-352.
40. Peters, J., J.V.R. Heberlein, and J. Lindsay, *Spectroscopic diagnostics in a highly constricted oxygen arc.* J. Phys. D: Appl. Phys., 2007. **40**: p. 3960-3971.
41. Girard, L., et al., *Experimental study of an oxygen plasma cutting torch: I. Spectroscopic analysis of the plasma jet.* J. Phys. D: Appl. Phys., 2006. **39**: p. 1543.
42. Colombo, V., et al., *High-speed imaging in plasma arc cutting: a review and new developments.* Plasma Sources Sci. Technol., 2009. **18**: p. 1-24.
43. Boselli, M., et al., *High-speed imaging investigation of transient phenomena impacting plasma arc cutting process optimization.* J. Phys. D: Appl. Phys., 2013. **46**: p. 1-10.
44. Bemis, B.L. and G.S. Settles, *Visualization of liquid metal, arc, and jet interaction in plasma cutting of steel sheet.* 8th Int. Symp. on Flow Visualization (Sorrento), 1998.
45. Bemis, B.L. and G.S. Settles, *Ultraviolet Imaging of the anode attachment in transferred-arc plasma cutting.* IEEE Transactions on Plasma Science, 1999. **27**: p. 44-45.

46. Teulet, P., et al., *Experimental study of an oxygen plasma cutting torch: II. Arc-material interaction, energy transfer and anode attachment.* J. Phys. D: Appl. Phys., 2006. **39**: p. 1557-1573.
47. Kavka, T., et al., *Experimental study of anode processes in plasma arc cutting.* J. Phys. D: Appl. Phys., 2013. **46**: p. 1-11.
48. Colombo, V., et al., *Advances in Plama Arc Cuttin Technology: The Experimental Part of an Integrated Approach.* Plasma Chem Plasma Process, 2012. **32**: p. 411-426.
49. Nemchinsky, V.A. and W.S. Severance, *What we know and what we do not know about plasma arc cutting.* J. Phys. D: Appl. Phys., 2006. **39**: p. R423-R438.
50. Osterhouse, D.J., J. Lindsay, and J.V.R. Heberlein, *Using arc voltage to locate the anode attachment in plasma arc cutting.* J. Phys. D: Appl. Phys., 2013. **46**: p. 1-7.
51. Griffiths, D.J., *Introduction to Electrodynamics*. 1999, Upper Saddle River: Prentice-Hall, Inc.
52. Modest, M.F., *Radiative Heat Transfer*. 2nd ed. 2003, San Diego: Academic Press.
53. Lowke, J.J., *Predictions of Arc Temperature Profiles Using Approximate Emission Coefficients for Radiation Losses.* J. Quant. Spectrosc. Radiat. Transfer, 1974. **14**: p. 111-122.
54. Naghizadeh-Kashani, Y., Y. Cressault, and A. Gleizes, *Net emission coefficient of air thermal plasmas.* J. Phys. D: Appl. Phys., 2002. **35**: p. 2925-2934.
55. Essoltani, A., et al., *Volumetric Emission of Argon Plasmas in the Presence of Vapors of Fe, Si, and Al.* Plasma Chem Plasma Process, 1994. **14**(4): p. 437-450.
56. Vincenti, W.G. and C.H. Kruger, *Introduction to Physical Gas Dynamics*. 1965, Malabar: Krieger Publishing Company.
57. Godin, D. and J.Y. Trepanier, *A Robust and Efficient Method for the Computation of Equilibrium Composition in Gaseous Mixtures.* Plasma Chem Plasma Process, 2004. **24**(3): p. 447-473.
58. Kramida, A., et al., *NIST Atomic Spectra Database*. 2012, National Institute of Standards and Technology.
59. Drellishak, K.S., D.P. Aeschliman, and A.B. Cambel, *Partition Functions and Thermodynamic Properties of Trogen and Oxygen Plasmas.* The Physics of Fluids, 1965. **8**(9): p. 1590-1600.
60. Lias, S.G., *Ionization Energy Evaluation*, in *NIST Chemistry WebBook, NIST Standard Reference Database Number 69*, National Institute of Standards and Technology.
61. Colombo, V., E. Ghedini, and P. Sanibondi, *Thermodynamic and transport properties in non-equilibrium argon, oxygen, and nitrogen thermal plasmas.* Progress in Nuclear Energy, 2008. **50**: p. 921-933.
62. Ghorui, S., J.V.R. Heberlein, and E. Pfender, *Thermodynamic and Transport Properties of Two-temperature Oxygen Plasmas.* Plasma Chem Plasma Process, 2007. **27**: p. 267-291.
63. Cressault, Y., et al., *Influence of metallic vapours on th properties of air thermal plasmas.* Plasma Sources Sci. Technol., 2008: p. 1-9.
64. Chapman, S. and T.G. Cowling, *The mathematical theory of non-uniform gases*. 1939, London: Cambridge University Press.
65. Hirschfelder, J.O., C.F. Curtiss, and R.B. Bird, *Molecular Theory of Gases and Liquids*. 1954, New York: John Wiley and Sons, Inc.
66. Bonnefoi, C., *State Thesis*. 1983, University of Limoges, France.
67. Aubreton, J., M.F. Elchinger, and P. Fauchais, *New Method to Calculated Thermodynamic and Transport Properties of a Multi-Temperature Plasma: Application to N2 Plasma.* Plasma Chem Plasma Process, 1998. **18**(1): p. 1-27.

68. Rat, V., et al., *Calculation of Combined Diffusion Coefficients from the Simplified Theory of Transport Properties.* Plasma Chem Plasma Process, 2001. **21**(3): p. 355-369.
69. Rat, V., et al., *Transport properties in a two-temperature plasma: Theory and application.* Physical Review E, 2001. **64**: p. 026409.
70. Rat, V., et al., *Diffusion in two-temperature thermal plasmas.* Physical Review E, 2002. **66**: p. 056407.
71. Rat, V., et al., *Transport coefficients including diffusion in a two-temperature argon plasma.* J. Phys. D: Appl. Phys., 2002. **35**: p. 981-991.
72. Rat, V., et al., *Treatment of non-equilibrium phenomena in thermal plasma flows.* J. Phys. D: Appl. Phys., 2008. **41**: p. 183001.
73. Capitelli, M., C. Gorse, and S. Longo, *Collision Integrals of High-Temperature Air Species.* Journal of Thermophysics and Heat Transfer, 2000. **14**(2): p. 259-267.
74. Andre, P., W. Bussiere, and D. Rochette, *Transport Coefficients of Ag-SiO2 Plasmas.* Plasma Chem Plasma Process, 2007. **27**: p. 381-403.
75. Murphy, A.B. and C.J. Arundell, *Transport Coefficients of Argon, Nitrogen, Oxygen, Argon-Nitrogen, and Argon-Oxygen Plasmas.* Plasma Chem Plasma Process, 1994. **14**(4): p. 451-490.
76. Versteeg, H.K. and W. Malalasekera, *An Introduction to Computational Fluid Dynamics: The Finite Volume Method*. 2nd ed. 2007, Essex: Pearson Education Limited.
77. Mahajan, M., *Numerical Modeling of Plasma Cutting Torches*, in *Mechanical Engineering*. 2010, University of Minnesota: Minneapolis.
78. Heberlein, J.V.R., J. Mentel, and E. Pfender, *The anode region of electric arcs: a survey*. J. Phys. D: Appl. Phys., 2010. **43**(2): p. 023001.
79. Nemchinsky, V.A., *Liquid Metal Movement during Plasma Arc Cutting.* Welding Journal, 1996. **75**(12): p. 388s-392s.
80. Megli, T.W., et al., *Modeling Plasma Processes in 1-Kilowatt Hydrazine Arcjet Thrusters.* Journal of Propulsion and power, 1998. **14**(1): p. 29-36.